ELASTICITY MEASUREMENT AT HIGH TEMPERATURES

by

KENNETH ROBERT CHAPLAIN

Submitted for the Degree of
Doctor of Philosophy
at
The University of Aston in Birmingham
August 1979

ELASTICITY MEASUREMENT AT HIGH TEMPERATURES

K. R. Chaplain

Doctor of Philosophy 1979

Summary

A magnetostrictive delay line technique is used to excite the resonant modes of vibration of thin discs. The temperature variations of Poisson's Ratio and Young's modulus are measured using these modes. The elastic constants of a variety of grades of graphite, including pyrolytic graphite (which was found to have a negative Poisson's Ratio parallel to the basal plane) have been measured up to a temperature of 1000°C. Tables of a normalised frequency parameter for thin discs are given covering the ranges of Poisson's Ratio -0.5 to +0.5 in steps of 0.01 to enable the calculation of Poisson's Ratio and Young's modulus from the thin disc resonant frequencies.

The delay line technique was found to be applicable to the excitation of end resonances in cylindrical solids. Experimental evidence is given of end resonant modes having 2 or more nodal diameters. Comparisons are made between the end resonant frequencies and those of the corresponding thin disc modes. It was found that in all these cases the end resonant frequency was below the cut-off frequency.

A technique of elastic constant measurement at high temperatures, complementary to the resonant thin disc method is given. This consists of a double pulse, time of flight method which does not require a high material Q and easily lends itself to automation. A design for an instrument is presented which automatically tracks the variation in time of flight resulting from the temperature change of the material. The method is demonstrated by measuring the variation of the Young's modulus of Thoriated Tungsten up to 1800°C.

ACOUSTIC VELOCITY, END RESONANCE, PYROLYTIC GRAPHITE, ULTRASONIC MATERIAL CHARACTERISATION

ACKNOWLEDGEMENTS

It is a pleasure to take this opportunity to express my gratitude to my supervisor Dr. J. F. W. Bell, for his constant advice and encouragement throughout this study. I would like to thank my colleagues in the Instrumentation group for many useful discussions and also to the workshop staff and technicians for their assistance.

I gratefully acknowledge the financial support of the Science Research Council and Professor J. E. Flood, of the Department of Electrical and Electronic Engineering for the provision of laboratory facilities.

CONTENTS

PAGE

4. THIN DISC SPECTRA

5. MEASUREMENT OF ELASTIC CONSTANTS

6. TIME OF FLIGHT MEASUREMENT OF ELASTIC CONSTANTS

LIST OF SYMBOLS

A	constant
A_m	amplitude coefficient of stress components
a	bar radius
B	constant
C	constant
	composite echo amplitude (Chapter 6)
c	velocity
C_d	dilatational wave velocity
C_g	group velocity
C_p	thin disc velocity
C_t	shear velocity
C_ϕ	phase velocity
$C_{i,j,k,\ell}$	elastic coefficient tensor
d	bar diameter
E	Young's modulus
e	error voltage
$f_{n,m}$	frequency of (n,m) disc mode
J_n	nth order Bessel function
j	$\sqrt{-1}$
k	defined as C_t/C_d
$K_{n,m}$	dimensionless frequency parameter
ℓ_o	sensor length
n	circular order
n_x	number of oscillations to crossover
r	radius
R	reflection coefficient

$S_{k,\ell}$	strain tensor
T_{ij}	stress tensor
T	transmission coefficient
T_{zz}	normal stress at end boundary
$T_{\theta z}$	} shear stress
T_{rz}	
t	time
u	displacement
V_E	echo return signal
V_1	forcing function
W	rotation
z	longitudinal co-ordinate
Z_1	characteristic impedance of line
Z_2	resonator impedance
Z	defined as Z_2/Z_1
α	defined by $\alpha^2 = \omega^2/C_d^2 - \gamma^2$
$\bar{\alpha}$	normalised longitudinal wavenumber = βa
β	defined by $\beta^2 = \omega^2/C_t^2 - \gamma^2$
$\bar{\beta}$	normalised angular wavenumber = βa
γ	wavenumber of propagation constant
$\bar{\gamma}$	normalised wavenumber = γa
Δ	dilation
η	thickness to diameter ratio
θ	angular co-ordinate
λ	Lamé constant
	wavelength
μ	Lamé constant

ρ	density
σ	Poisson's ratio
τ_o	room temperature delay
τ_θ	delay at temperature θ
τ	integrator time constant
τ_{zz}	normal stress coefficient
$\tau_{\theta z}$	shear stress coefficients
τ_{rz}	
ω	frequency
Ω	normalised frequency

LIST OF FIGURES

PAGE

Chapter 2

Chapter 3

Chapter 4

Chapter 5

Chapter 6

Chapter 7

CHAPTER 1

INTRODUCTION

CHAPTER 1

INTRODUCTION

The resonant spectrum of a solid body depends on the physical form and the elastic constants of the material. For a limited number of geometries theoretical solutions for the spectrum are known and hence an experimentally determined spectrum allows the elastic constants to be calculated. For isotropic materials the number of independent elastic constants reduces to two, in this work Young's Modulus and Poisson's Ratio are chosen. These constants are convenient for engineering calculations, the latter constant changes only slightly with temperature, variations mainly affecting Young's Modulus.

Work has been concentrated on isotropic and near isotropic solids with cylindrical geometry. The already existing theory of the in-plane vibrations of thin discs has been used. The numerical tables available have been extended to include the wide range of Poisson's Ratio of currently available engineering materials at intervals of 0.01. Errors arising from the evaluation of high order Bessel's Function in previous work(51) were detected and have been eliminated. A theoretical and experimental study has been made of the trapped resonances which occur at the end of cylindrical structures. Experimental results have been obtained for various materials having a wide range of Poisson's Ratio.

An experimental pulse echo technique using a magnetostrictive delay line enables the solid to be driven at any selected point and orientation. The line introduces sufficient delay to separate the transmission from the echo. Modes of vibration having a displacement component in the direction of the drive will be excited. In the case of a free isotropic disk a radial drive will automatically be at an antinode of the modes having nodal diameters. With disks having weak anisotropy the nodal orientation is not wholly determined by the drive position which similarly affects the degree of coupling to the mode. For torsional vibration an angled drive is necessary.

In material studies the length of the delay line enables the specimen to be in a furnace while the magnetostrictive transducer is located outside. This system has considerable flexibility. The specimen can be made integral with the line, thus avoiding a high temperature joint. While the section of the line at the transducer must be magnetostrictive the main length can be chosen for low loss or refractory properties relevant to a particular application.

It has been found that as the melting point of a polycrystalline material is approached, the internal friction becomes so high that any resonance method of obtaining the elastic constants is unworkable. In these circumstances the "Time of Flight" method is more appropriate. It has the advantage that while the signal is attenuated by high loss materials it is still strong and quite measurable. Again the method is ideally suited to magnetostrictive excitation techniques since thin wires can be used. An additional advantage is that the method is easily automated, allowing the variations in flight time to be tracked without further operator intervention.

In the end resonances of solid cylinders the energy is confined to a region within one or two radii of the end. They are readily excited by a line drive and have nodal patterns which are very similar to those of thin discs. The frequencies are a few percent lower than the disc frequencies and below the cut-off frequency of the lowest corresponding propagating mode. In all experimental investigations of end resonance no evidence was found of modes with nodal circles although modes with a full range of nodal diameters were found. Results are given for modes up to circular order 7 (corresponding to 7 nodal diameters). Theoretical attempts to solve these non axi-symmetric end resonances use a summation of a number of modes at selected points over the end face to satisfy approximately the stress free boundary condition on the end. The solution of the Pochhammer Chree equations for an infinite cylindric solid yields an infinite number of modes with real, complex and imaginary propagating modes. The modes with complex and imaginary modes exist below the cut-off frequencies of the non axi-symmetric propagating mode. The evidence points to the fact that end resonance is associated with these complex propagation constants. This is similar to the approach used successfully by Zemanek(11) dealing with symmetric mode end resonance and Bell and Karlmarczie(52) solving the case of the unique end resonance that occurs in a thin strip.

CHAPTER 2

WAVE PROPAGATION IN INFINITE CYLINDRICAL SOLIDS

CHAPTER 2

WAVE PROPAGATION IN INFINITE CYLINDRICAL SOLIDS

2.1 Introduction

An understanding of the propagating modes in an infinite cylinder is central to any discussion of vibrations in semi-infinite or finite cylindrical bodies. For example, the modes of vibration that exist in the semi-infinite bar at a given frequency are a subset of the modes that exist in an infinite bar. In the former there are two stress free surfaces and in the latter only one. It was thought at one time that only a finite number of real modes could exist at a finite frequency, that is modes with real propagation constants. It was later discovered that complex solutions to the frequency equation could exist and moreover that there were an infinity of these complex solutions at any finite frequency.

Historically the development of the theory of cylindrical propagating modes is generally attributed to Pochhammer (1) and Chree(2) in the last quarter of the nineteenth century. The equations of motion and the resulting frequency equation are discussed by Love(3). In 1941 Bancroft(4) carried out some numerical solutions of the frequency equation and gave velocity dispersion curves as a function of bar diameter to wavelength ratio for several values of Poisson's ratio. Bancroft's work was restricted to the longitudinal mode (n=0 in the following), the lowest frequency mode which is of considerable importance in elasticity measurements. Hudson(5) in 1943 extended this work to give velocity dispersion curves for the longitudinal and first flexural modes (the first flexural mode has one nodal diameter) for the range of Poisson's ratio 0.0 to 0.5. Adem(6) demonstrated the existence of complex roots for the symmetric mode frequency equation.

The barrier to the accurate numerical solution of the frequency equation was removed by the introduction of high speed digital computers in the 1960's. Mindlin and McNiven(7) in 1960, using approximate equations derived the axially symmetric mode dispersion curves at low frequency for real, imaginary and complex propagation constants. Also in 1960 Pao and Mindlin(8) gave a grid of bounds for the real propagation constants of the first flexural mode and Pao(9) extended this to include imaginary propagation constants. In 1972 Zemanek(11) gave full dispersion spectra for longitudinal modes and flexural modes up to circular order 4 at a Poisson's ratio of 0.3317 (the value for Aluminium).

In this chapter longitudinal dispersion spectra are computed for real, complex and imaginary solutions of the frequency equation for 3 values of Poisson's ratio, 0.25, 0.30 and 0.35. The dispersion spectra for higher circular orders are illustrated with the flexural mode spectra for n=1 to 3 at a Poisson's ratio of 0.3. The computer programmes used to compute these spectra were developed as a preliminary to obtaining the end resonance spectra of the longitudinal mode discussed in more detail in Chapter 3.

2.2 The Wave Equation for an Isotropic Solid

If the deformations of an elastic solid are small then stress is linearly related to strain. This is stated mathematically by the generalised Hooke's Law in tensor form.

$$T_{ij} = C_{ijk\ell}S_{k\ell} \tag{2.2.1}$$

Equation (2.2.1) represents nine equations giving a total of 81 elastic coefficients $C_{ijk\ell}$. It is shown by Love$^{(3)}$ that for an isotropic elastic solid the number of independent elastic constants reduces to 2 and the total number of equations reduces to 6. Equation (2.2.1) can then be written.

$$\begin{bmatrix} T_1 \\ T_2 \\ T_3 \\ T_4 \\ T_5 \\ T_6 \end{bmatrix} = \begin{bmatrix} \lambda+2\mu & \lambda & \lambda & 0 & 0 & 0 \\ \lambda & \lambda+2\mu & \lambda & 0 & 0 & 0 \\ \lambda & \lambda & \lambda+2\mu & 0 & 0 & 0 \\ 0 & 0 & 0 & 2\mu & 0 & 0 \\ 0 & 0 & 0 & 0 & 2\mu & 0 \\ 0 & 0 & 0 & 0 & 0 & 2\mu \end{bmatrix} \begin{bmatrix} S_1 \\ S_2 \\ S_3 \\ S_4 \\ S_5 \\ S_6 \end{bmatrix} \tag{2.2.2}$$

where λ and μ are the standard Lamé elastic constants. The two constants can be related to any of the engineering elastic constants such as Young's modulus, Bulk modulus, Torsional (Shear) modulus and Poisson's ratio and are conveniently summarised by Redwood$^{(12)}$.

Under conditions of zero body force the vector equation of motion is

$$(\lambda + \mu)\nabla\nabla.\bar{u} + \mu\nabla^2\bar{u} = \rho\ddot{\bar{u}} \qquad (2.2.3)$$

where $\ddot{\bar{u}}$ denotes the second differential of the displacement with respect to time.

If the displacement is defined in terms of potential functions (equation (2.2.4)) then two recognisable wave equations emerge[13]

$$\bar{u} = \text{grad}\ \phi + \text{curl}\ \bar{\psi}$$

and (2.2.4)

$$R(\psi_I) + R(\psi_0) = 0$$

$$(\lambda + 2\mu)\nabla^2\phi = \rho\ddot{\phi}$$

$$\mu\nabla^2\bar{\psi} = \rho\ddot{\bar{\psi}} \qquad (2.2.5)$$

where ϕ is the scalar displacement potential and $\bar{\psi}$ is the vector displacement potential.

The dilatational or volumetric wave represented by the scalar potential function ϕ propagates with a velocity C_d and the rotational (Shear) wave represented by the vector potential function $\bar{\psi}$ propagates with a velocity C_t where

$$C_d = \left[\frac{(\lambda+2\mu)}{\rho}\right]^{\frac{1}{2}} \qquad (2.2.6a)$$

and

$$c_t = \left[\frac{\mu}{\rho}\right]^{\frac{1}{2}} \qquad (2.2.6b)$$

Equation (2.2.5) represents four partial differential equations and, in cylindrical polar co-ordinates, have the following solutions.

$$\begin{aligned} \phi &= A_1\ J_n(\alpha r)\cos n\theta\ \exp\{j(\gamma z-\omega t)\} \\ \psi_r &= A_2\ J_{n+1}(\beta r)\sin n\theta\ \exp\{j(\gamma z-\omega t)\} \\ \psi_\theta &= -A_2\ J_{n+1}(\beta r)\cos n\theta\ \exp\{j(\gamma z-\omega t)\} \\ \psi_z &= A_3\ J_n(\beta r)\sin n\theta\ \exp\{j(\gamma z-\omega t)\} \end{aligned} \qquad (2.2.7)$$

where

$$\alpha^2 = \frac{\omega^2}{c_d^{\,2}} - \gamma^2 \qquad (2.2.8a)$$

and

$$\beta^2 = \frac{\omega^2}{c_t^{\,2}} - \gamma^2 \qquad (2.2.8b)$$

2.3 Displacement Equations

Combining equations (2.2.7) and (2.2.4) give the displacement components

$$
\begin{aligned}
u_r &= U_r \cos n\theta \exp\{j(\gamma z - \omega t)\} \\
u_\theta &= U_\theta \sin n\theta \exp\{j(\gamma z - \omega t)\} \qquad (2.3.1a) \\
u_z &= U_z \cos n\theta \exp\{j(\gamma z - \omega t)\}
\end{aligned}
$$

where

$$
\begin{aligned}
U_r &= AJ_n'(\alpha r) + \frac{\gamma B}{\beta} J_n'(\beta r) + \frac{n}{r} CJ_n(\beta r) \\
U_\theta &= -\frac{n}{r} AJ_n(\alpha r) - B\frac{\gamma n}{\beta r} J_n(\beta r) - CJ_n'(\beta r) \qquad (2.3.1b) \\
U_z &= j\gamma AJ_n(\alpha r) - jB\beta J_n(\beta r)
\end{aligned}
$$

A, B and C are arbitrary constants and the prime denotes differentiation with respect to r.

2.4 The Boundary Conditions

The stress strain relationship of equation (2.2.1) written in terms of the Lamé constants is

$$T_{ii} = \lambda(S_{11} + S_{22} + S_{33}) + 2\mu\, S_{ii} \tag{2.4.1a}$$

and

$$T_{ij} = 2\mu S_{ij} \qquad \text{(Summation not implied.)} \tag{2.4.1b}$$

In cylindrical co-ordinates i=r, θ or z, and j=θ, z or r respectively. The strains in terms of displacement components are given by equation (2.4.2).

$$\begin{aligned}
S_{rr} &= \frac{\partial u_r}{\partial r} \\
S_{\theta\theta} &= \frac{1}{r}\frac{\partial u_\theta}{\partial \theta} + \frac{u_r}{r} \\
S_{zz} &= \frac{\partial u_z}{\partial z} \\
S_{\theta z} &= \frac{1}{2}\left(\frac{1}{r}\frac{\partial u_z}{\partial \theta} + \frac{\partial u_\theta}{\partial z}\right) \\
S_{rz} &= \frac{1}{2}\left(\frac{\partial u_r}{\partial z} + \frac{\partial u_z}{\partial r}\right) \\
S_{r\theta} &= \frac{1}{2}\left(\frac{\partial u_\theta}{\partial r} - \frac{u_\theta}{r} + \frac{1}{r}\frac{\partial u_r}{\partial \theta}\right)
\end{aligned} \tag{2.4.2}$$

For an infinitely long bar the only stress free boundary is the curved surface at r=a where 2a is the diameter of the bar. The boundary conditions are therefore

$$T_{rr}\Big|_{r=a} = T_{rz}\Big|_{r=a} = T_{r\theta}\Big|_{r=a} = 0 \tag{2.4.3}$$

2.5 The Infinite Rod Frequency Equation

Using the displacement equation (2.3.1b) and the boundary conditions of Section 2.4 result in the matrix equation (2.5.1).

$$\begin{bmatrix} T_{rr} \\ T_{r\theta} \\ T_{rz} \end{bmatrix} = \begin{bmatrix} a_{11} & a_{12} & a_{13} \\ a_{21} & a_{22} & a_{23} \\ a_{31} & a_{32} & a_{33} \end{bmatrix} \begin{bmatrix} A \\ B \\ C \end{bmatrix} = [0] \tag{2.5.1}$$

For a non-trivial solution the determinant of the 3×3 matrix must be zero, i.e.

$$\begin{vmatrix} a_{11} & a_{12} & a_{13} \\ a_{21} & a_{22} & a_{23} \\ a_{31} & a_{32} & a_{33} \end{vmatrix}_{r=a} = 0 \tag{2.5.2}$$

Equation (2.5.2) is known as the infinite rod frequency equation. The a_{ij} terms written in normalised form convenient for computation are

$$a_{11} = [\frac{\Omega^2-2\bar{\gamma}^2}{2} - n^2 - n]\, J_n(\bar{\alpha}) + \bar{\alpha} J_{n-1}(\bar{\alpha})$$

$$a_{12} = [n^2+n-\bar{\beta}^2] J_n(\bar{\beta}) - \bar{\beta} J_{n-1}(\bar{\beta})$$

$$a_{13} = 2n[\bar{\beta} J_{n-1}(\bar{\beta}) - (n+1) J_n(\bar{\beta})]$$

$$a_{21} = n[\bar{\alpha} J_{n-1}(\bar{\alpha}) - (n+1) J_n(\bar{\alpha})]$$

$$a_{22} = n[(n+1)J_n(\bar{\beta}) - \bar{\beta}J_{n-1}(\bar{\beta})]$$

$$a_{23} = 2\bar{\beta}J_{n-1}(\bar{\beta}) - (2n^2 + 2n - \bar{\beta}^2)J_n(\bar{\beta})$$

$$a_{31} = n\ J_n(\bar{\alpha}) - \bar{\alpha}J_{n-1}(\bar{\alpha})$$

$$a_{32} = \frac{\bar{\gamma}^2 - \bar{\beta}^2}{2\bar{\gamma}^2}[\bar{\beta}J_{n-1}(\bar{\beta}) - nJ_n(\bar{\beta})]$$

$$a_{33} = n\ J_n(\bar{\beta})$$

The normalised wave numbers are

$$\bar{\gamma} = \gamma a; \qquad \bar{\alpha} = \alpha a \qquad \text{and} \quad \bar{\beta} = \beta a$$

and are related to the normalised frequency Ω (defined as $\frac{\omega a}{C_t}$) by

$$\bar{\alpha}^2 = k^2\Omega^2 - \bar{\gamma}^2$$

$$\bar{\beta}^2 = \Omega^2 - \bar{\gamma}^2$$

where $k^2 = (C_t/C_d)^2 = \frac{(1-2\sigma)}{2(1-\sigma)}$

and σ is Poisson's ratio.

The above frequency equation (2.5.2) is in a more convenient form for computer solution than that given by Meeker and Meitzler(14) and is very similar to that given by Zemanek(11). In fact equation (2.5.2) can be made identical to equation 4 of Zemanek's by the following procedure:-

i) Change sign of third row

ii) Change sign of third column and multiply by n.

iii) Take out a factor n from the second row

iv) Subtract the second row from the first row

v) Change the sign of the first row and the second column.

Equation (2.5.2) is seen to contain three variables, the normalised frequency Ω, the normalised propagation constant $\bar{\gamma}$ and Poisson's ratio σ.

2.6 The Axially Symmetric Mode Frequency Spectra

The axially symmetric mode frequency equation is readily obtained as a simplification of (2.5.2) by setting the circular order n equal to zero. Thus the determinant (2.5.2.), expanded, becomes

$$a_{23}\,(a_{11}\,a_{32} - a_{12}\,a_{31}) = 0 \qquad (2.6.1)$$

Note that either the first term, a_{23} or the bracketed term can be equal to zero independently. The first term equal to zero gives the eigenvalues of the torsional modes and is given in full by equation (2.6.2)

$$\bar{\beta}\,J_0(\bar{\beta}) - 2J_1(\bar{\beta}) = 0 \qquad (2.6.2)$$

The torsional modes will not be considered further in this thesis.

The bracketed term of (2.6.1) is the frequency equation for the axially symmetric longitudinal modes and is given in expanded form by equation (2.6.3).

$$2\Omega^2\bar{\alpha}\,J_1(\bar{\alpha})J_1(\bar{\beta}) - (\Omega^2-2\bar{\gamma}^2)^2\,J_0(\bar{\alpha})J_1(\bar{\beta}) - 4\bar{\gamma}^2\bar{\alpha}\bar{\beta}\,J_1(\bar{\alpha})\,J_0(\bar{\beta})=0 \qquad (2.6.3)$$

2.6.1 Method of Solution of the Frequency Equation

The roots $\bar{\gamma}_i$ of equation (2.6.3) are required over a range of Ω to obtain the dispersion spectra which constitute the basis for the work on end resonances that follows in Chapter 3. The equation was solved for real, complex and imaginary roots using a modification of Newton Raphson's iteration procedure given by equation (2.6.4).

$$z_n = z_o - z_i \frac{f(z)}{f(z+z_i)-f(z)} \qquad (2.6.4)$$

A mode was tracked by starting at the already calculated frequency for $\gamma=0$ (the thin disc) and then obtaining γ for various other Ω values. The results are sensitive to Poisson's ratio.

The above procedure was programmed on an ICL 1904S computer and was found to converge on a root to 4 places of accuracy after 5 to 8 iterations. A sample of the results are displayed graphically in the dispersion spectra of Figure 2.1 for the longitudinal mode (n=0). The three graphs are for differing values of Poisson's ratio. Features of the dispersion spectra for both longitudinal and flexural modes are discussed in Section 2.8.

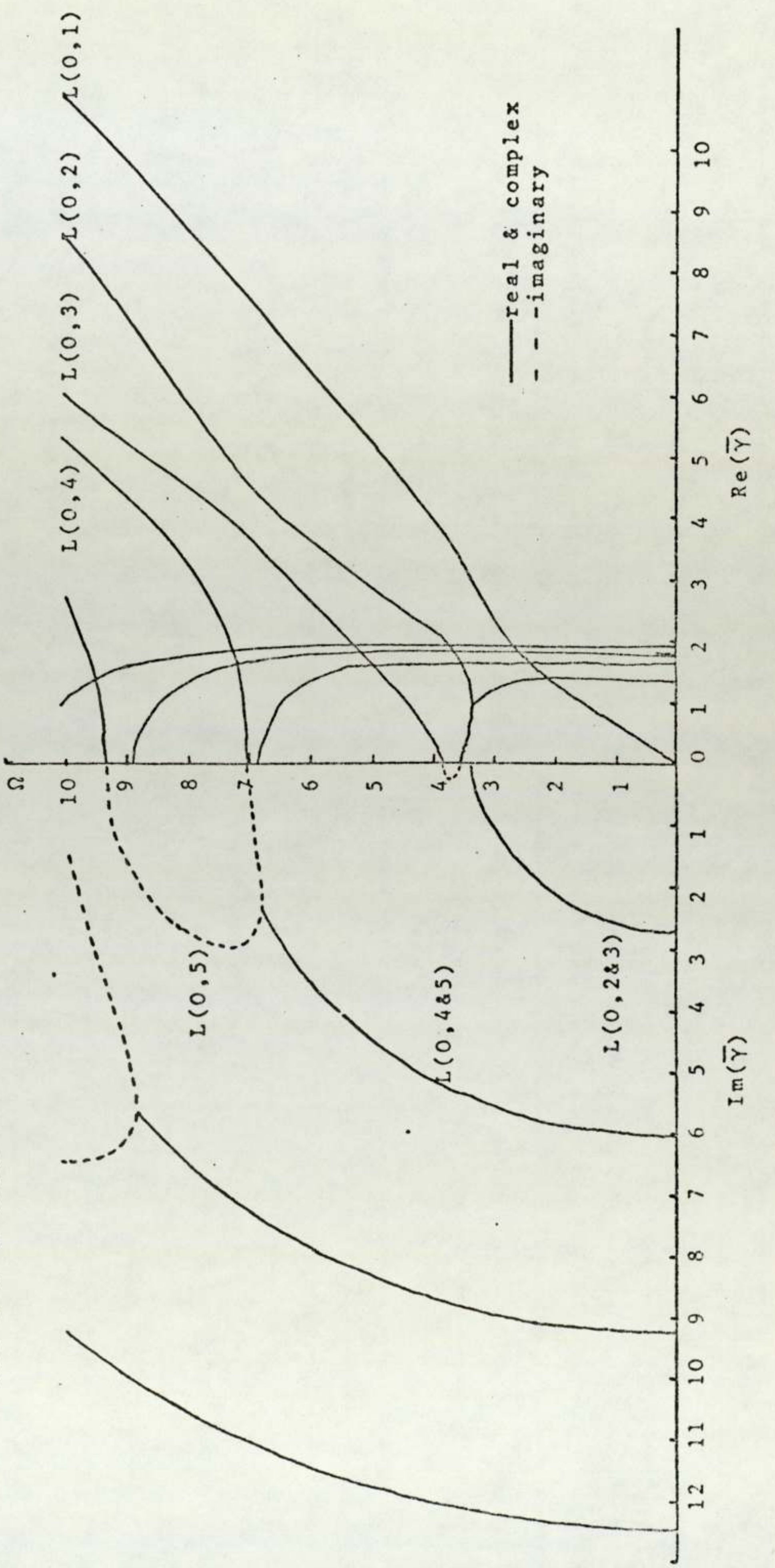

FIGURE 2.1a

Frequency dispersion curves for n=0 σ=0.25

FIGURE 2.1b

Frequency dispersion curves
for n=0 $\sigma=0.30$

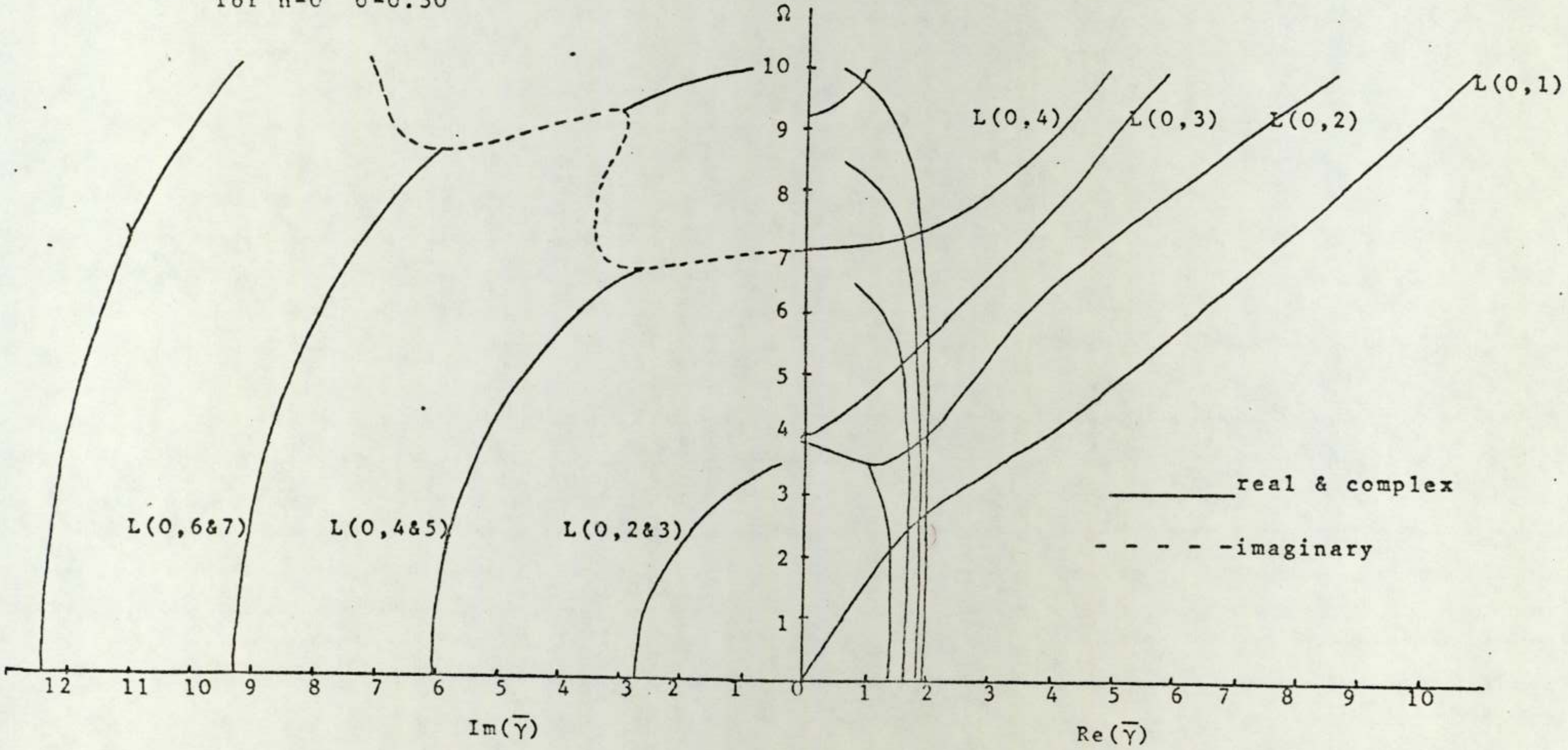

FIGURE 2.1 c
Frequency dispersion curves
for n=0 σ=0.35

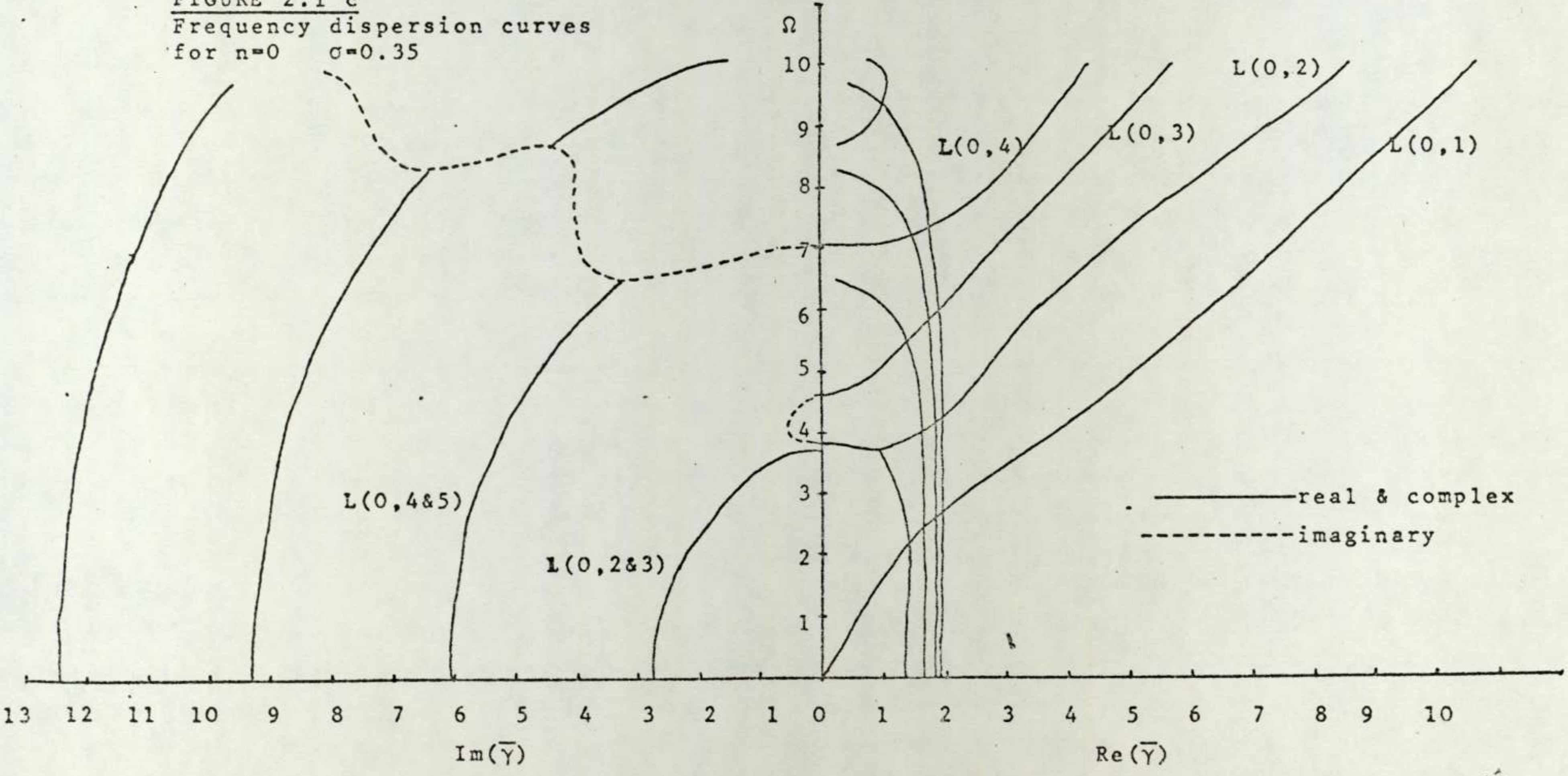

2.7 Non-Axially-Symmetric Mode Frequency Spectra

When the circular order n is greater than zero, no further simplification of the frequency equation (2.5.2) is possible. The first flexural mode of the bar occurs with n=1 and is considered by Hudson$^{(5)}$. A second computer program was written to obtain the roots of the more general equation (2.5.2) for real,complex and imaginary propagation constants for any value of n using an identical technique to that given in Section 2.6.1.

Figure 2.2 shows the results obtained for the first flexural mode (n=1) with higher flexural modes (n=2 and n=3) shown in Figures 2.3 and 2.4. Although the programs were used to obtain results up to circular order 6 the spectra are not shown since no new features appear in the spectra.

FIGURE 2.2

Frequency dispersion curves
for n=1
σ=0.30

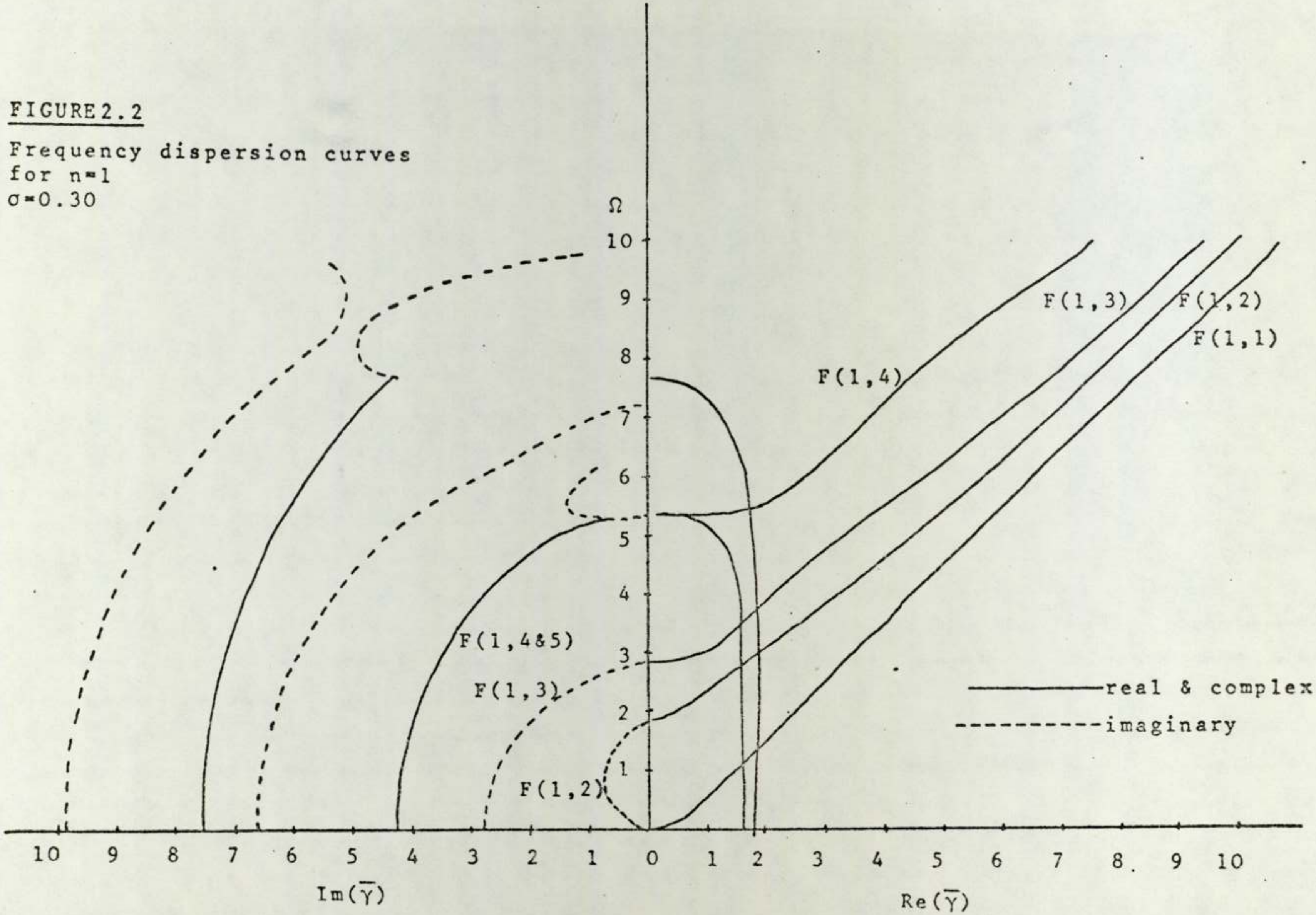

FIGURE 2.3
Frequency dispersion curves
for n=2
σ=0.30

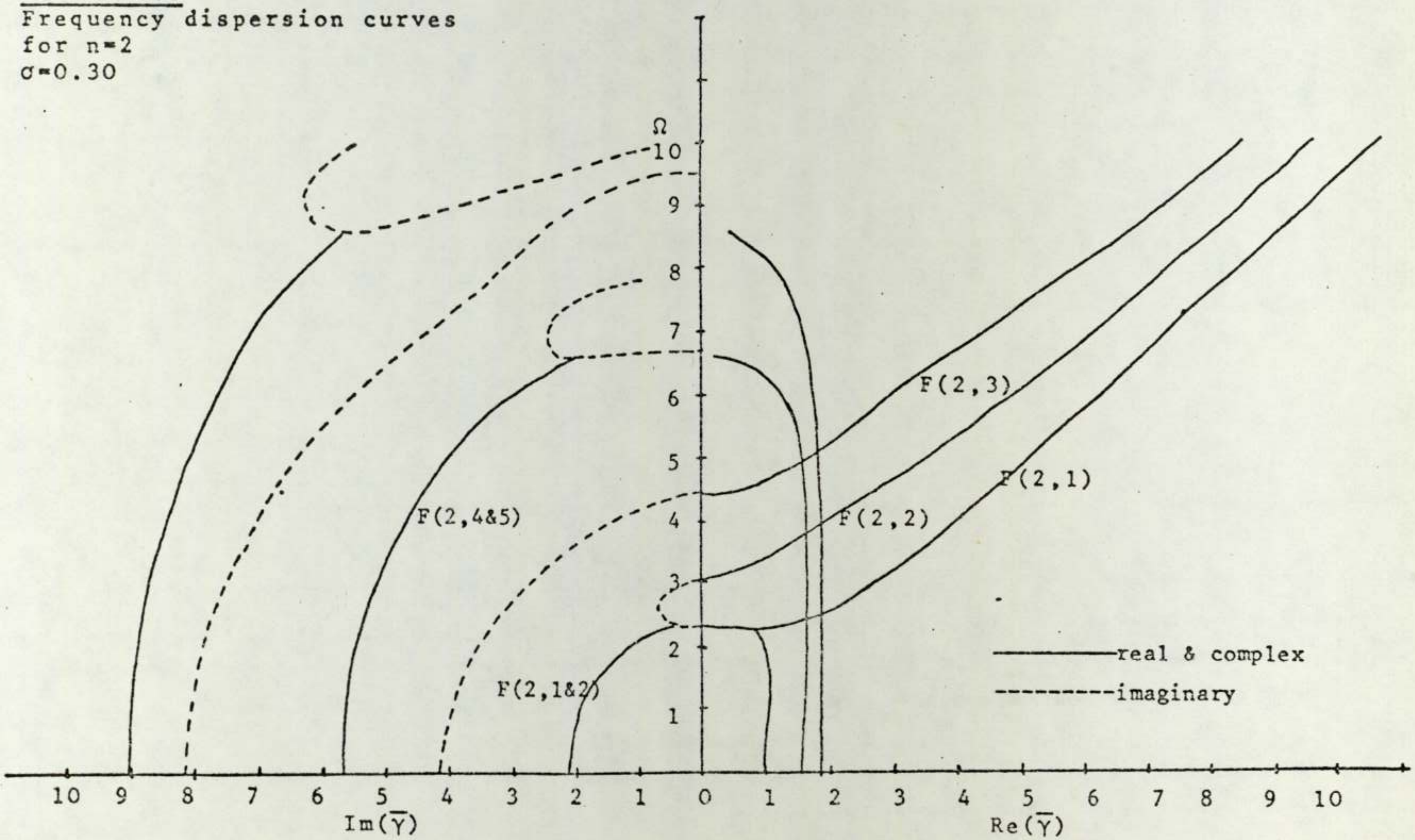

FIGURE 2.4

Frequency dispersion curve for n=3

σ=0.3

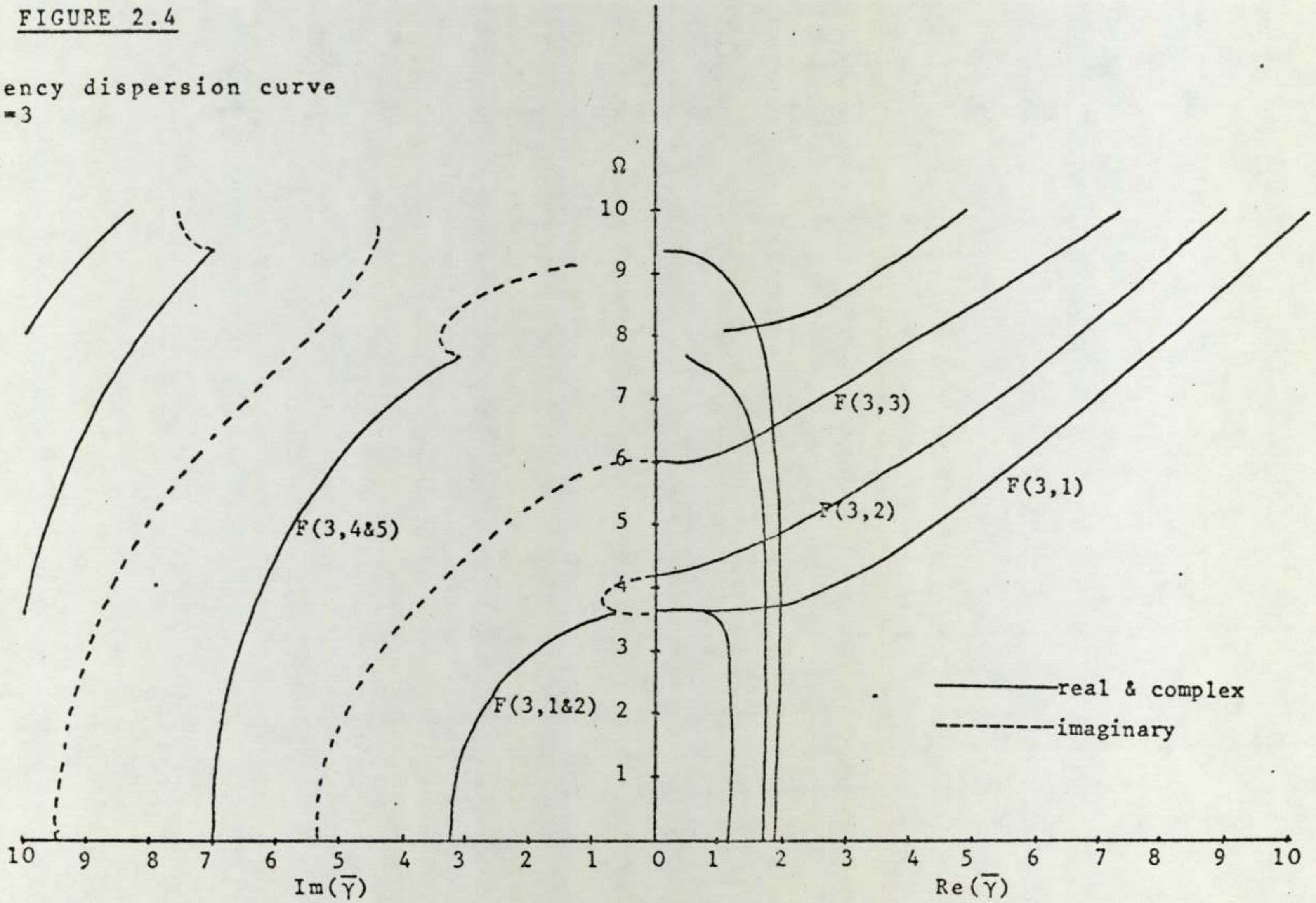

2.8 Features of the Frequency Spectra

The information relating frequency, propagation constant and velocity can normally be presented in two ways. The curves shown in Figures 2.1 to 2.4 are known as frequency spectra or dispersion spectra. An alternative to this representation are the velocity dispersion curves such as those shown in References (4) and (5). The frequency spectra method of displaying the information is probably the most useful since it also contains all the information required to plot velocity dispersion characteristics. While velocity dispersion curves could in principle be drawn for real, imaginary and complex velocity, only real velocity curves are plotted since the other velocities are not physically meaningful. The method of obtaining the velocity dispersion characteristics is illustrated using Figure 2.5.

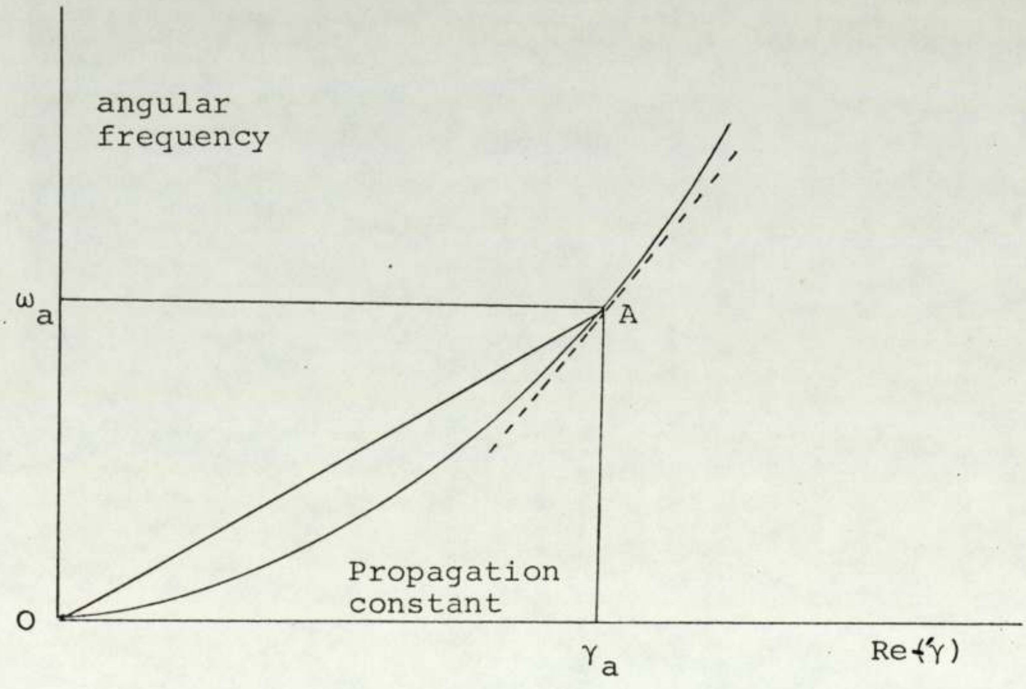

Fig. 2.5

The slope of the line OA in Figure 2.5 is the phase velocity at the propagation constant γ_a and frequency ω_a. The tangent to the curve at the point A is the group velocity at γ_a. Thus

$$\text{Phase Velocity} \quad C_{\phi a} = \left.\frac{\omega}{\gamma}\right|_{\gamma=\gamma_a} \tag{2.8.1}$$

and

$$\text{Group Velocity} \quad C_{ga} = \left.\frac{d\omega}{d\gamma}\right|_{\gamma=\gamma_a} \tag{2.8.2}$$

In addition the cut-off phenomena are readily observed from the frequency spectra when the propagation constant tends to zero and the frequency remains finite. However, the cut-off phenomenon is also implied in the velocity dispersion curves by the infinite phase velocity.

2.8.1 Imaginary and Complex Propagation

Where the propagation constant of a mode is real the energy will travel as a wave along the rod. The significance of imaginary and complex values of γ is readily seen:-

$$\underline{\gamma \text{ Imaginary}} \qquad \exp(-\gamma_i z)\ \exp(-j\omega t) \tag{2.8.3a}$$

$$\underline{\gamma \text{ Complex}} \qquad \exp(-\gamma_i z)\ \exp j(\gamma_r z-\omega t) \tag{2.8.3b}$$

Where γ_r and γ_i are the real and imaginary parts of complex γ respectively. The equation (2.8.3a) represents a spatially decaying non-propagating vibration while equation (2.8.3b) shows the same amplitude decaying form but is a propagating wave. The frequency spectra of Figures 2.1 to 2.4 are drawn in two dimensions, but to fully represent the solutions to the frequency equation a three dimensional figure would be required. The real and imaginary solutions of $\bar{\gamma}$ occur in positive and negative pairs while the complex solutions occur in positive and negative complex conjugate pairs, thus the spectra shown contain all the numerical information necessary to reconstruct all the solutions by suitable adjustment of the signs of γ.

2.8.2 Mode Designations (8,11,13,14)

The notation L(0,m) is used to identify the various longitudinal modes of the frequency spectra where m is the mth solution of the frequency equation. The flexural modes are identified by F(n,m) denoting the mth solution for circular order n (of equation (2.3.1)). Thus the designation of the real modes of Figures 2.1 to 2.4 is obvious. The designation of the imaginary and complex modes is not so clear. The method adopted here is to associate the complex and imaginary mode with a real mode. For example, consider the spectra of 2.1c. Starting at a frequency of Ω of 7 and travelling down the L(0,3) curve with Ω decreasing eventually reaches cut-off at Ω=4.7. At this point an

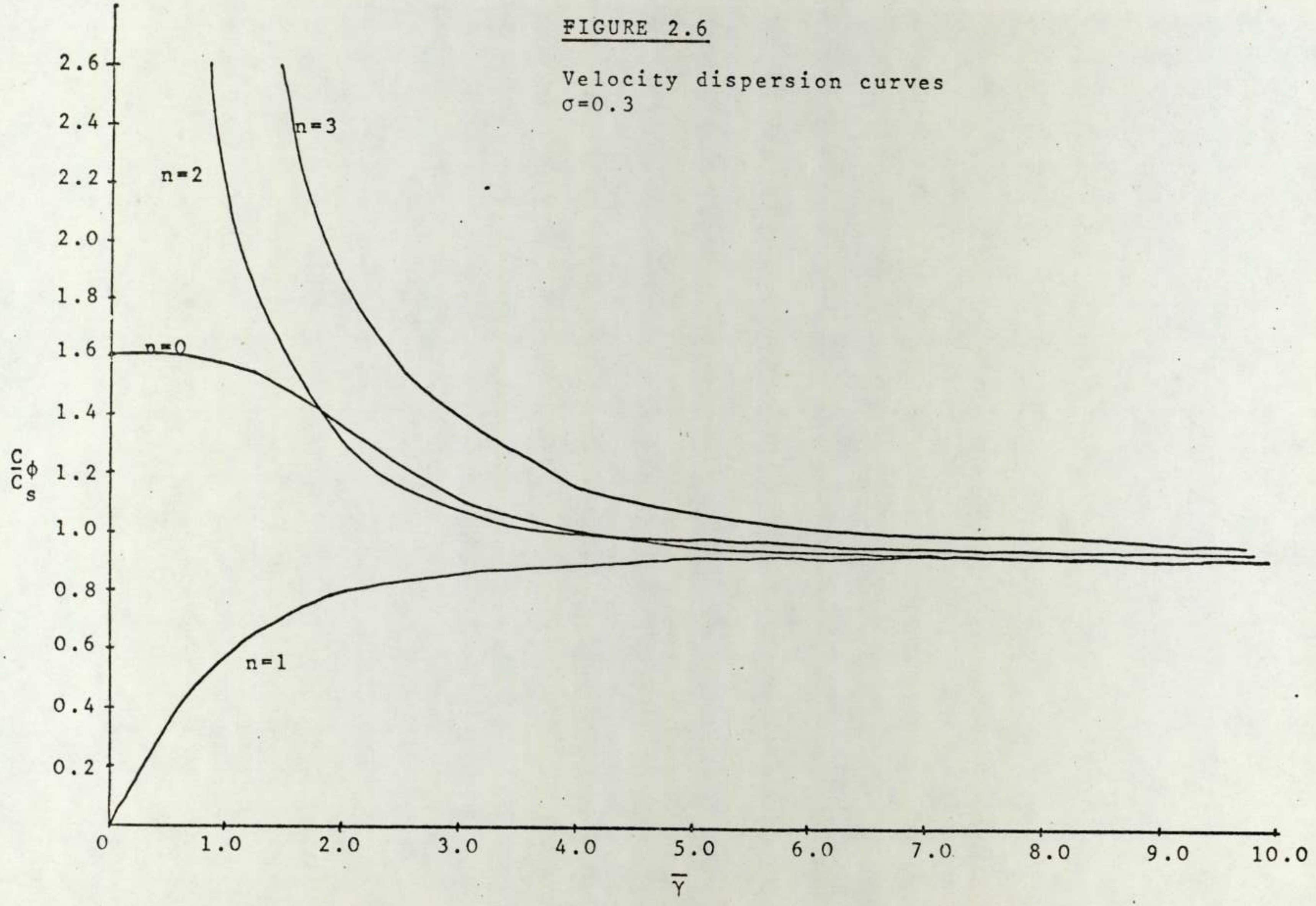

FIGURE 2.6

Velocity dispersion curves
σ=0.3

imaginary mode emerges and is still designated the L(0,3) mode until it returns to the line $\bar{\gamma}=0$. This point also corresponds to the cut-off frequency of the L(0,2) mode. Similarly this point could have been arrived at by travelling along the line of the L(0,2) mode. It is worth noting at this point that the portion of the L(0,2) wave between $\bar{\gamma}=0$ and 1.0 has a negative group velocity. This point has been discussed by Meitzler(15) who points out that the energy propagates with a positive group velocity and the phase velocity is negative relative to the group velocity. Applying strictly the arguments that the mode designation is determined from the real mode with Ω decreasing, this portion of the curve could equally well be associated with the L(0,3) mode. This is not entirely satisfactory since it would imply that the L(0,3) mode would have two cut-off frequencies and for this reason the negative slope portion is associated with the L(0,2) mode. The lowest complex mode, the L(0,2&3) can be arrived at following the path of the L(0,3) mode discussed above and also via the L(0,2) mode with Ω decreasing. The complex L(0,2&3) branches at a minimum of the L(0,2) curve.

The Figure 2.1b drawn for $\sigma=0.30$ shows that the L(0,2) and L(0,3) modes have very nearly the same cut-off frequency and that the L(0,3) imaginary mode joining the two cut-off points has almost disappeared. In fact, as will be seen in the next section this occurs at $\sigma=0.28$.

There are some interesting differences between the longitudinal and the flexural modes as shown in Figures 2.1 to

2.4. The flexural modes all show modes with $\bar{\gamma}$ imaginary extending to zero frequency, this does not occur with the longitudinal modes in Figure 2.1. Also with the exception of the first flexural modes (F(1,m)), the lowest real modes have a cut-off frequency. This point is discussed further in Chapter 3 where it is shown that difficulties are encountered in trying to account for end resonances in cylinders of $n>2$.

2.8.3 Cut-off Frequencies

The cut-off frequency equations are obtained from equation (2.5.2) by letting $\bar{\gamma}\to 0$ with Ω remaining finite. With $n=0$ to give the axially symmetric modes the cut-off frequency equation becomes:-

$$J_1(\Omega)\left[\Omega J_0(k\Omega) - 2kJ_1(k\Omega)\right] = 0 \qquad (2.8.4)$$

The first term of (2.8.4) is not a function of Poisson's ratio and is the axial shear cut-off frequency since at cut-off vibrations are entirely axial. The bracketed term at cut-off is denoted radial shear, since vibration is purely radial. Cut-off frequency versus Poisson's ratio for axially symmetric modes is plotted in Figure 2.7.
It is clear that the L(0,2) and L(0,3) modes have the same cut-off frequency at $\sigma=0.28$. This is the case where the L(0,3) imaginary mode entirely disappears.

FIGURE 2.7

Variation of cut-off frenquencies with Poisson's Ratio

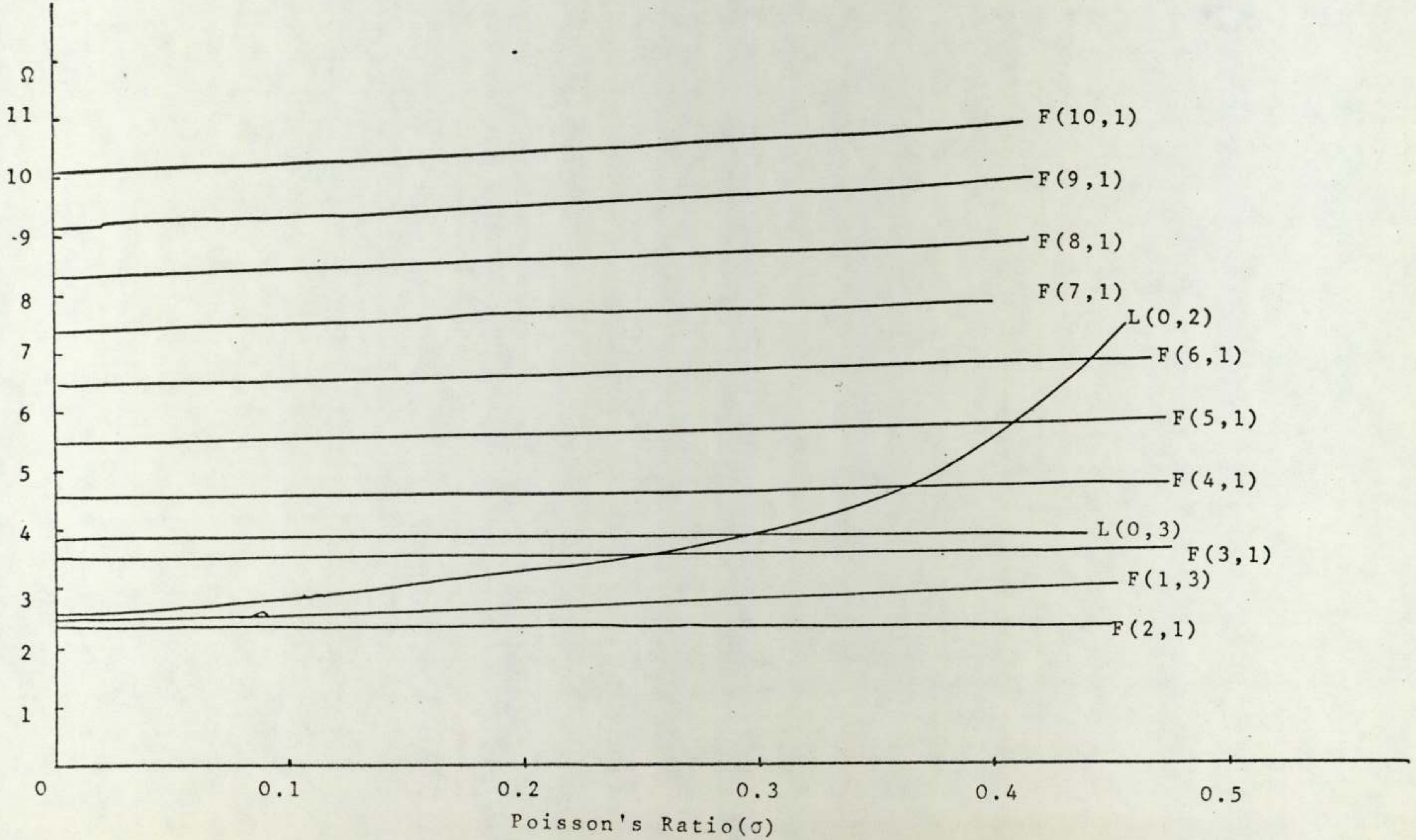

The non-axially symmetric mode cut-off frequency equation is given by equation (2.5.2) and letting $\bar{\gamma}$ tend to zero. Denoting the terms of the determinants with $\bar{\gamma}=0$ as a'_{ij}, they are:-

$$
\begin{aligned}
a'_{11} &= \left[\frac{\Omega}{2}^{2} - n^{2} - n\right] J_n(k\Omega) + k\Omega\, J_{n-1}(k\Omega) \\
a'_{12} &= \left[n^{2} + n - \Omega^{2}\right] J_n(\Omega) - \Omega J_{n-1}(\Omega) \\
a'_{13} &= 2n\left[\,\Omega J_{n-1}(\Omega) - (n+1) J_n(\Omega)\right] \\
a'_{21} &= n\left[k\Omega J_{n-1}(k\Omega) - (n+1J_n(k\Omega)\right] \\
a'_{22} &= n\left[(n+1) J_n(\Omega) - \Omega J_{n-1}(\Omega)\right] \\
a'_{23} &= 2\Omega J_{n-1}(\Omega) - (2n^{2} + 2n - \Omega^{2}) J_n(\Omega) \\
a'_{31} &= nJ_n(k\Omega) - k\Omega J_{n-1}(k\Omega) \\
a'_{32} &= \Omega J_{n-1}(\Omega) - nJ_n(\Omega) \\
a'_{33} &= nJ_n(\Omega)
\end{aligned}
\qquad (2.8.5)
$$

The variation of flexural mode cut-off frequencies with Poisson's ratio are shown in Figure 2.7.

CHAPTER 3

END RESONANCE IN SOLID CYLINDERS

CHAPTER 3

END RESONANCE IN SOLID CYLINDERS

3.1 Introduction

This chapter describes attempts to obtain theoretical solutions for the frequencies of non-axisymmetric (flexural) mode end resonances and follows techniques already used successfully for the axisymmetric (longitudinal) mode end resonance.

Using the wire drive technique the end resonance frequency for each circular order mode up to n=7 has been measured for materials having a wide range of Poisson's ratio. These frequencies are very useful for the theoretical work as they indicate quite accurately the values where a solution is to be expected.

It will be shown later in this chapter (equation (3.3.6)) that the function of $\bar{\gamma}$ representing the stress at the end face of a semi-infinite bar is odd for normal and even for shear stresses. The end face boundary conditions cannot therefore be satisfied by the reflection of any single mode. The superposition of all possible modes are necessary, (Ref. 11, 17, 50) i.e. all modes below the cut-off frequency of the associated propagating mode.

In the case of the longitudinal mode (n=0) these consist of a single real mode and the infinity of complex ones (Figure 2.1). For the second flexural mode (n=2) there is no real mode but an infinity of those with both complex and imaginary propagation constants. Zemanek(11) in a theoretical study found that, when using a summation of reflected real and complex modes to satisfy the boundary conditions, the amplitude coefficients of the complex modes rose to a high value close to experimentally observed and resonance frequency. A number of other workers have also observed end resonance in cylindrical solids with Oliver(19) usually credited with being the first to observe the phenomenon. The majority of work on end resonances has been carried out on the longitudinal (symmetrical) mode end resonance with only passing attention to higher order resonances, although McMahon(20) and Booker and Sagar(22) mention having observed end resonances at n=2 and n=3.

A possible explanation for the lack of interest in higher order end resonances in the literature is the difficulty in observing them using piezo-electric transducers, coupled with the fact that they only appear at the end face of the bar. The experimental technique given here allows end resonances to be observed of any order within the frequency limits of the transducer system, nominally to about 200 KHz. Experimental observations are presented of end resonances up to circular order n=7 in isotropic materials having a wide range of Poisson's ratios.

The method used by Zemanek(11) to obtain the longitudinal end resonance frequency at a Poisson's ratio of 0.33 (the value for Aluminium) has been extended to cover the range of Poisson's ratio 0.1 to 0.5 and experimental results have been obtained over the range 0.1 to 0.33. It is shown in Section 3.5 that this theoretical technique cannot be directly extended to include the higher order flexural mode end resonances since these modes occur below the cut-off frequency of the corresponding propagating mode. Attempts to establish the relative phase of the two lowest complex modes as an indicator of resonance, or standing waves over the relevant frequency range did not show any positive results. Nevertheless, experimentally obtained end resonance frequencies are given and compared with the corresponding mode cut-off frequencies and disc frequencies. Differences between the longitudinal mode and flexural mode end resonances are apparent from Figures 3.6 and 3.9. The longitudinal mode end resonance is very close to a linear function of Poisson's ratio while the flexural modes all have a distinct minima at a Poisson's ratio about 0.31. In addition the two types of mode have different slopes at the low values of Poisson's ratio and it is unlikely that this is due to any fault in the experimental technique.

An uncertainty concerning the isotropy of the material is always present. Rods which are drawn will have longitudinal grains and may be subject to radial cooling. Radial anisotropy, which would result in a splitting of many distortion modes in discs, has not been observed in steel, aluminium or brass discs cut from rods but is conspicuous in discs cut from rolled sheets. The glass rod, unambiguously isotropic was not perfectly circular.

3.2 Boundary Conditions on End Plane

The stresses at the z = constant plane are obtained by combining (2.3.1a), (2.4.1) and (2.4.2) to give explicit equations for the stress T_{zz}, $T_{\theta z}$ and T_{rz} which are required to be zero and take the form.

$$\begin{aligned} T_{zz} &= \tau_{zz}\cos n\theta \exp(j(\gamma z-\omega t)) = 0 \\ T_{\theta z} &= \tau_{\theta z}\sin n\theta \exp(j(\gamma z-\omega t)) = 0 \\ T_{rz} &= \tau_{rz}\cos n\theta \exp(j(\gamma z-\omega t)) = 0 \end{aligned} \qquad (3.2.1)$$

The problem of satisfying (3.2.1) with a single reflected mode lies in the fact that: if T_{zz} and $T_{\theta z}$ are satisfied exactly at the end face the T_{rz} cannot be (Refs. 3, 23). It will be seen that in equation (3.5.1) T_{zz} and $T_{\theta z}$ are odd functions of $\bar{\gamma}$ and T_{rz} is an even function of $\bar{\gamma}$. Early solutions (Ref. 2) to the finite length rod set T_{rz} to zero for the condition r/λ small. Since T_{rz} is already equal to zero on the curved boundary, its value on the end face can be taken to be approximately zero. However when r/λ is large it is found$^{(11)}$ that this approximation is no longer valid and that a series solution is necessary to cancel the residual stresses.

3.3 The Symmetric Mode End Resonance

The symmetric mode is obtained from equation (3.2.1) by setting n=0 leaving only two stress components T_{zz} and T_{rz} at the flat boundary. The zero stress condition is obtained by setting the sum of all possible modes, with real, complex and imaginary propagation constants, equal to zero (equation (3.3.1)).

$$\begin{aligned} T_{zz}(r) &= \sum_{m=0}^{\infty} A_m T_{zz_m}(r) = 0 \\ T_{rz}(r) &= \sum_{m=0}^{\infty} A_m T_{rz_m}(r) = 0 \end{aligned} \qquad (3.3.1)$$

A_m is the amplitude coefficient of the mth mode and may be complex, containing magnitude and phase information. In the experimental study a long burst of oscillations is launched via a magnetostrictive line transducer into the end face of the bar. The various modes are generated at this face (z=0) with amplitude coefficients A_m which take on values such that the sum of all modes at any position on the end face result in zero stress. Modes with real propagation constants propagate in the positive z direction, the direction into the bar.

In the case of complex propagation constants, there are four solutions to the frequency equation but physical arguments lead to only two of these solutions being valid for the case in question. Since the amplitude of the vibrations cannot increase indefinitely in the direction of propagation it is clear that the only two solutions acceptable are of the form a+jb and its negative complex conjugate. This implies that the amplitude variation with increasing z is a decreasing function.

With n=0 the displacement equations are

$$u_r = -A_\alpha J_1(\alpha r) - \gamma B J_1(\beta r)$$
$$u_z = j\gamma A J_0(\alpha r) - jB_\beta J_0(\beta r) \qquad (3.3.2)$$

One of the arbitrary constants can be eliminated by applying the boundary condition $T_{rz}=0$ at r=a. i.e.

$$T_{rz}\Big|_{r=a} = \mu\left(\frac{\partial u_r}{\partial z} + \frac{\partial u_z}{\partial r}\right) = 0 \qquad (3.3.3)$$

which gives the ratio

$$\frac{A}{B} = \frac{(\bar{\beta}^2-\bar{\gamma}^2)\ J_1(\bar{\beta})}{2\bar{\gamma}\bar{\alpha}\ J_1(\bar{\alpha})} \qquad (3.3.4)$$

The stress components (3.2.1) can then be written

$$T_{zz} = \frac{1}{\bar{\gamma}}\{(2\bar{\gamma}^2-\Omega^2)(2\bar{\gamma}^2+(1-2k^2)\Omega^2)J_1(\bar{\beta})J_0(\bar{\alpha}\bar{r})$$
$$+ 4\bar{\gamma}^2\bar{\alpha}\bar{\beta}J_1(\bar{\alpha})J_0(\bar{\beta}\bar{r})\}C \qquad (3.3.6)$$

$$T_{rz} = 2j\bar{\alpha}\{(2\bar{\gamma}^2-\Omega^2)J_1(\bar{\beta})J_1(\bar{\alpha}\bar{r})-J_1(\bar{\alpha})J_1(\bar{\beta}\bar{r})\}C$$

where C is a constant.

3.4 Reflection Coefficients of the Symmetric Mode

The method of solving the symmetric mode end resonance follows essentially that of Zemanek(11). The only difference is to take account of the transmission line driving technique and the assumption is that all modes are generated simultaneously at the driving point. However, Zemanek only dealt with one material, aluminium. The method is used here to plot the spectrum of symmetric mode end resonances, not previously obtained and is compared to a number of experimental values.

Symmetric mode end resonance occurs when the reflection coefficient A_m of the complex modes rise to large values. Although all complex mode coefficients have a larger amplitude at this frequency it is found that the reflection coefficient of the first complex mode takes on a value much larger than the two real modes, i.e. the incident and reflected real-modes.

Equation (3.3.1) is solved for A_m after normalisation to the real mode with positive propagation constant. To make such a solution achievable, equation (3.3.1) must be restricted to a finite number of modes and it was found that nine modes were a convenient number to take. Increasing the number beyond this figure only increased the computation time and did not significantly influence the computed end resonance frequencies. To solve equation (3.3.1) for these nine values of A_m the stresses (Equation (3.3.6)) were evaluated at nine discrete points along a radius. The normal stresses were calculated at five points along the radius including the centre and edge of the bar and the shear stresses were calculated at points midway between the normal stress points. Thus the approximate version of equation (3.3.1) can be written

$$-T_{zz_0}(r_i) = \sum_{m=1}^{a} A_m T_{zz_m}(r_i) \tag{3.4.1a}$$

$$-T_{rz_0}(r_i) = \sum_{m=1}^{a} A_m T_{rz_m}(r_i) \tag{3.4.1b}$$

where r_i in the case of (3.4.1a) is given by:

$$r_i = \frac{2a(i-1)}{m-1} \qquad i = 1,2,\ldots,\frac{m+1}{2} \tag{3.4.2}$$

and for (3.4.1b)

$$r_i = \frac{2ai}{m+1} \qquad i = 1,2,\ldots,\frac{m-1}{2} \tag{3.4.3}$$

and m is the total number of points taken, in this case nine.

Equation (3.4.1a) and (3.4.1b) represent a total of nine equations conveniently written in matrix form as equation (3.4.4).

$$[T_0] = [T_m][A_m] \tag{3.4.4}$$

T_0 is a column matrix of the values of the stress components due to the real mode with positive propagation constant, the first five elements being normal stresses and the remaining four shear stresses. T_m is a 9×9 square matrix whose columns represent individual stresses calculated at 9 positions along a radius and whose rows represent the 9 modes taken in the approximation. A_m is a column matrix of reflection coefficients. Computer programs were written to solve equation (3.4.4) with the propagation constants obtained from programs giving the specrta discussed in Chapter 2. The reflection coefficients were calculated as a function of frequency and the process repeated over the region of rapidly increasing A_m until the frequency of the peak was obtained to four significant figures. The phase of the reflection of the real mode coefficient is shown in Figure 3.1. This mode always has a magnitude of 1 and a phase of zero except in the region of end resonance where the phase is 180°. Also at this point the magnitude of the complex mode coefficients increase very rapidly to a peak. The behaviour of the magnitude of the first complex mode close to end resonance is shown in Figure 3.2 with the real and complex parts shown separately in Figure 3.3.

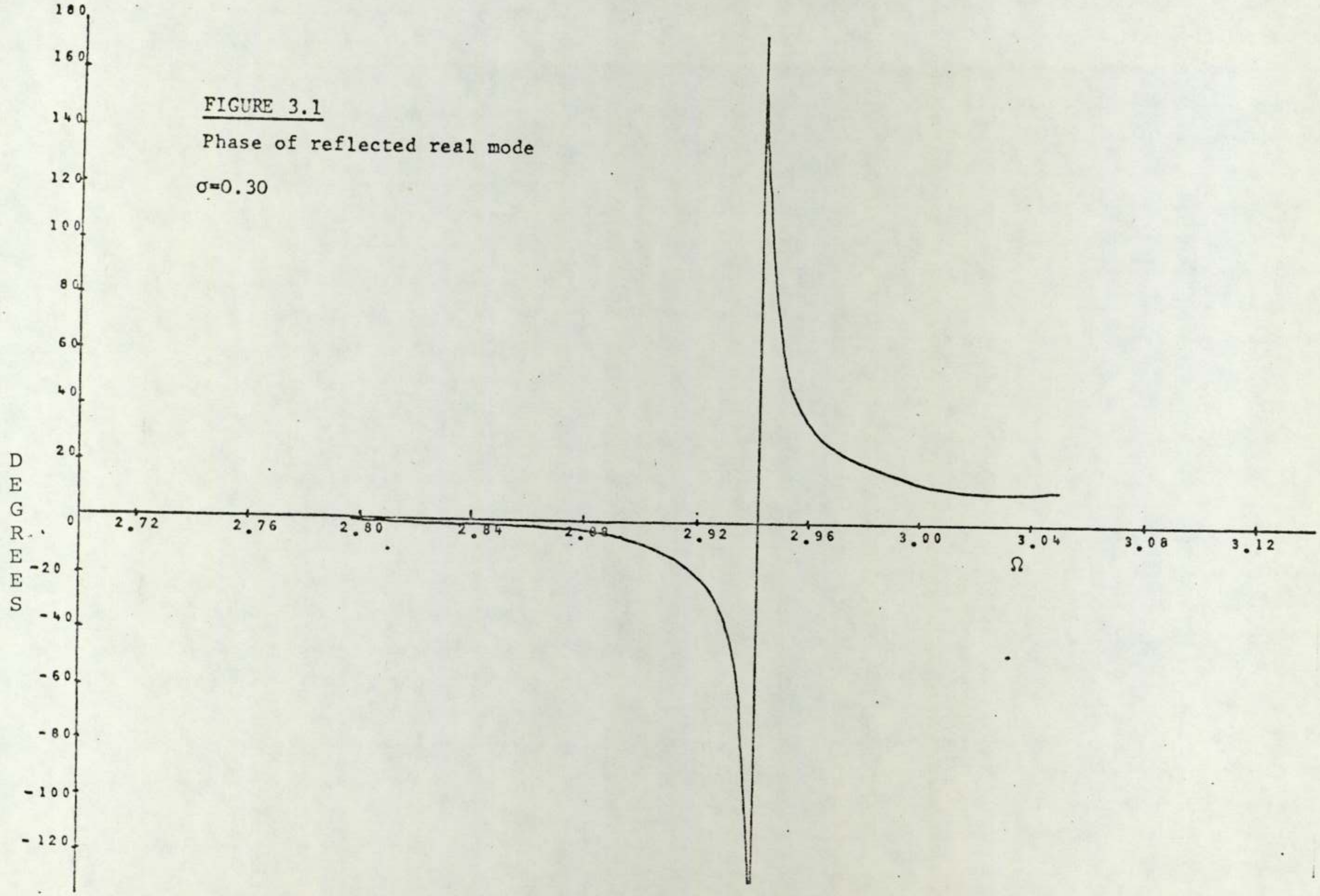

FIGURE 3.1

Phase of reflected real mode

$\sigma=0.30$

FIGURE 3.2

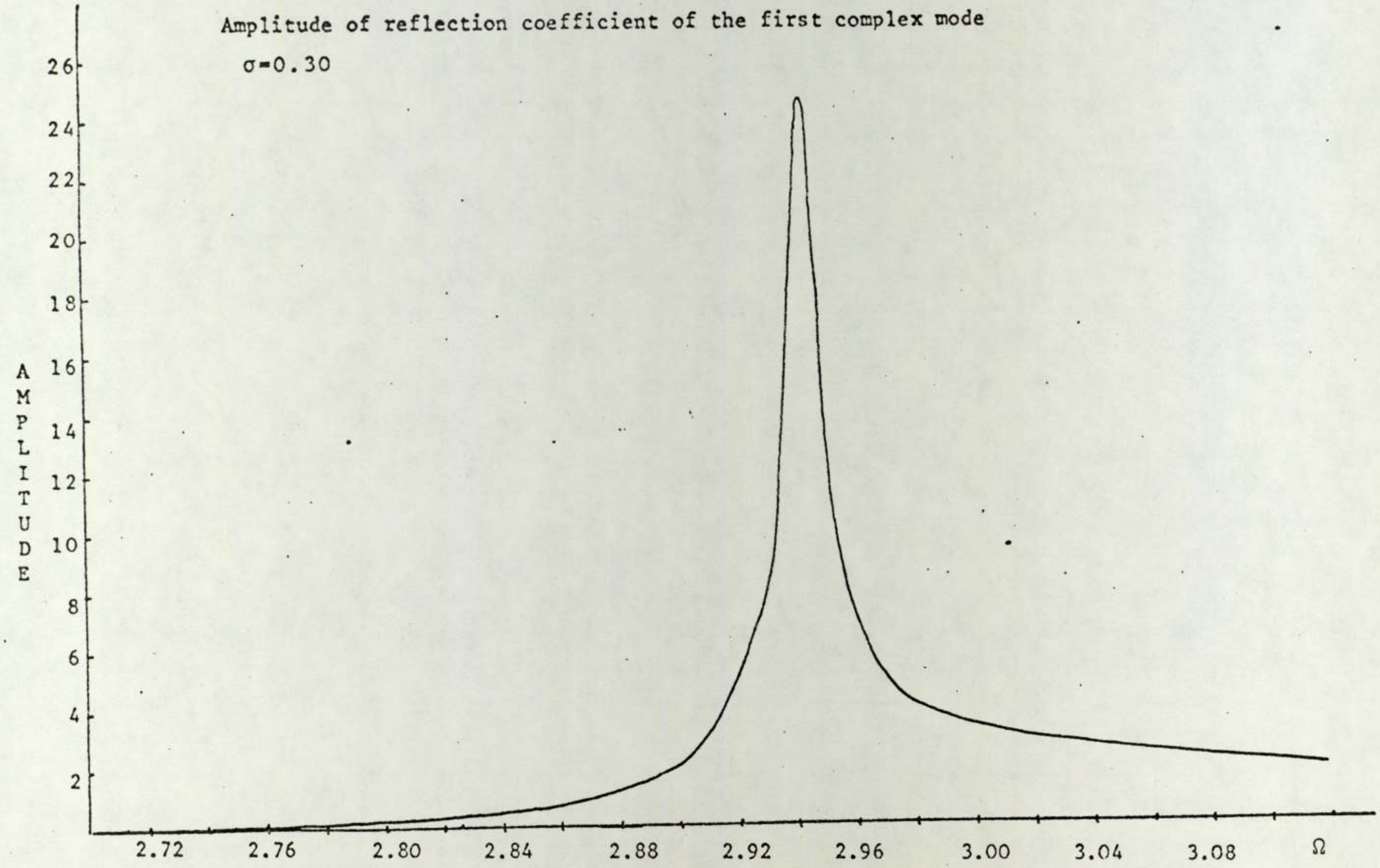

Amplitude of reflection coefficient of the first complex mode

σ=0.30

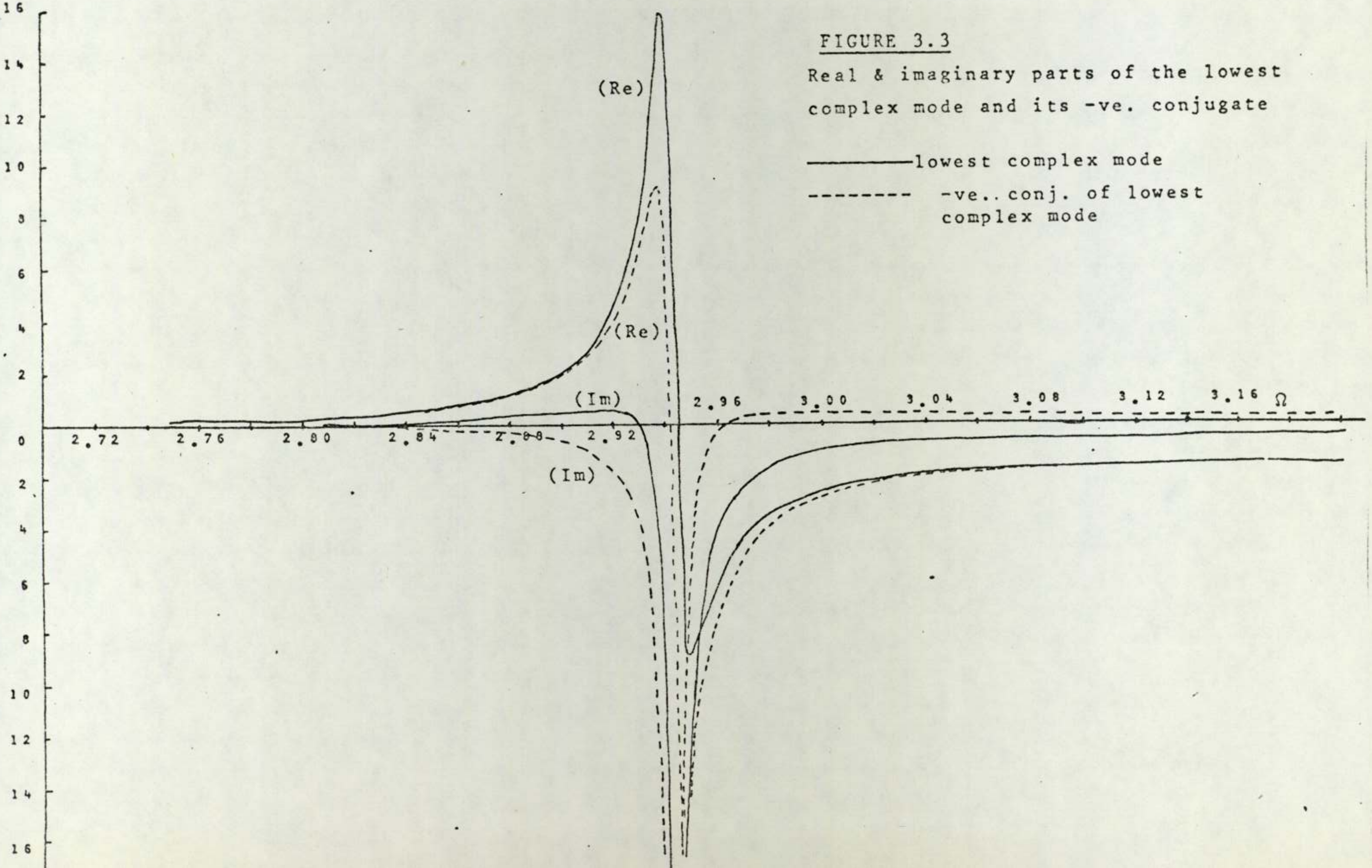

FIGURE 3.3

Real & imaginary parts of the lowest complex mode and its -ve. conjugate

3.5 Non-axisymmetric Modes

When the circular order n is greater than zero an additional stress component $T_{\theta z}$ must be included. This considerably complicates the stress equations at the end face of the bar since no simplification of equation (3.2.1) is possible. The components of stress T_{zz}, $T_{\theta z}$ and T_{rz} are obtained from equations (2.4.1) and (2.4.2). The stress coefficients of equation (3.2.1) are given by equation (3.5.1).

$$\begin{bmatrix} \tau_{zz} \\ \tau_{\theta z} \\ \tau_{rz} \end{bmatrix} = \begin{bmatrix} b_{11} & b_{12} & b_{13} \\ b_{21} & b_{22} & b_{23} \\ b_{31} & b_{32} & b_{33} \end{bmatrix} \begin{bmatrix} A \\ B \\ C \end{bmatrix} \tag{3.5.1}$$

where

$$b_{11} = - \frac{(\Omega^2 - 2\bar{\alpha}^2)}{2} \bar{r}^2 J_n(\bar{\alpha}\bar{r})$$

$$b_{12} = \bar{\beta}\bar{\alpha}\bar{r}^2 J_n(\bar{\beta}\bar{r})$$

$$b_{13} = 0$$

$$b_{21} = 2\bar{\gamma}\bar{r}_n J_m(\bar{\alpha}\bar{r})$$

$$b_{22} = \frac{n((\bar{\gamma}\bar{r})^2 - (\bar{\beta}\bar{r})^2)}{\bar{\beta}\bar{r}} J_n(\bar{\beta}\bar{r})$$

$$b_{23} = \bar{\gamma}\bar{r}(\bar{\beta}\bar{r}J_{n-1}(\bar{\beta}\bar{r}) - nJ_n(\bar{\beta}\bar{r}))$$

$$b_{31} = 2\bar{\gamma}\bar{r}(\bar{\alpha}\bar{r}J_{n-1}(\bar{\alpha}\bar{r}) - nJ_n(\bar{\alpha}\bar{r}))$$

$$b_{32} = \frac{((\bar{\gamma}\bar{r})^2 - (\bar{\beta}\bar{r})^2)}{\bar{\beta}\bar{r}}(\bar{\beta}\bar{r}J_{n-1}(\bar{\beta}\bar{r}) - nJ_n(\bar{\beta}\bar{r}))$$

$$b_{33} = n\bar{\gamma}\bar{r}J_n(\bar{\beta}\bar{r})$$

The three constants A, B and C can be written in terms of one arbitrary constant obtained from the boundary condition

$$T_{rr}\Big|_{r=a} = T_{rz}\Big|_{r=a} = 0 \qquad (3.5.2)$$

The constants are given below, denoted by a bar since strictly they differ from the above by a common constant.

$$\begin{aligned} \bar{A} &= a_2\, b_3 - a_3\, b_2 \\ \bar{B} &= a_3\, b_1 - a_1\, b_3 \qquad (3.5.3) \\ \bar{C} &= a_1\, b_2 - a_2\, b_1 \end{aligned}$$

where

$$a_1 = -2\{(\frac{(\Omega^2 - 2\bar{\gamma}^2)}{2} - n^2)J_n(\bar{\alpha}) + J_{n-1}(\bar{\alpha}) - nJ_n(\bar{\alpha})\}$$

$$a_2 = \frac{2\bar{\gamma}}{\beta}\{(n^2 - \bar{\beta}^2)J_n(\bar{\beta}) - \bar{\beta}J_{n-1}(\bar{\beta}) + nJ_n(\bar{\beta})\}$$

$$a_3 = 2n\{\bar{\beta}J_{n-1}(\bar{\beta}) - nJ_n(\bar{\beta}) - J_n(\bar{\beta})\}$$

$$b_1 = 2j\bar{\gamma}\{\bar{\alpha}J_{n-1}(\bar{\alpha}) - nJ_n(\bar{\alpha})\}$$

$$b_2 = j\frac{(\bar{\gamma}^2 - \bar{\beta}^2)}{\bar{\beta}}\{\bar{\beta}J_{n-1}(\bar{\beta}) - nJ_n(\bar{\beta})\}$$

$$b_3 = jn\bar{\gamma}\ J_n(\bar{\beta})$$

The zero stress condition for the three stress components above are obtained from an infinite sum due to the contributions from all possible modes.

$$
\begin{aligned}
T_{zz}(r)\Big|_{z=0} &= \sum_{m=0}^{\infty} A_m T_{zz}(r) = 0 \\
T_{\theta z}(r)\Big|_{z=0} &= \sum_{m=0}^{\infty} A_m T_{\theta z}(r) = 0 \qquad (3.5.4) \\
T_{rz}(r)\Big|_{z=0} &= \sum_{m=0}^{\infty} A_m T_{rz}(r) = 0
\end{aligned}
$$

3.6 Reflection Coefficients of Non-axisymmetric Modes

The boundary conditions for the non-axisymmetric mode involve an additional stress component $T_{\theta z}$ that was not present in the axisymmetric case. The stress components also depend on the angular co-ordinate θ(Equation (3.2.1)). The solution of equation (3.5.4) was carried out using a total of nine modes of complex and imaginary propagation constants. In the case of the axisymmetric mode the stress sums were set equal to zero at sufficient points along a radius to form the requisite number of equations to satisfy the boundary equations approximately. These points of zero stress represent zero stress circles in the case of the symmetric mode but this is not true forthe antisymmetric mode resulting from the independence of the stress components.

The reference mode in the case of the axisymmetric mode was the real mode that extends to zero frequency. In the case under consideration here, no real mode extends to zero frequency so the reflection coefficients were referred to the first complex mode. Now however, the criterion of end resonance used for the longitudinal mode is no longer relevant. Since the end resonance is found experimentally to occur at a clearly defined frequency, the implication is that a standing wave is present in the surface and over the region within a few wavelengths of the end. It is possible therefore that the relative phases ofthe negative conjugate modes will indicate the resonance condition. The phase relationship of the reflection coefficient that will indicate resonance is an in phase condition since the reflection coefficient is normalised to the wave travelling in the positive z direction and they appear on opposite sides of equation (3.4.4).

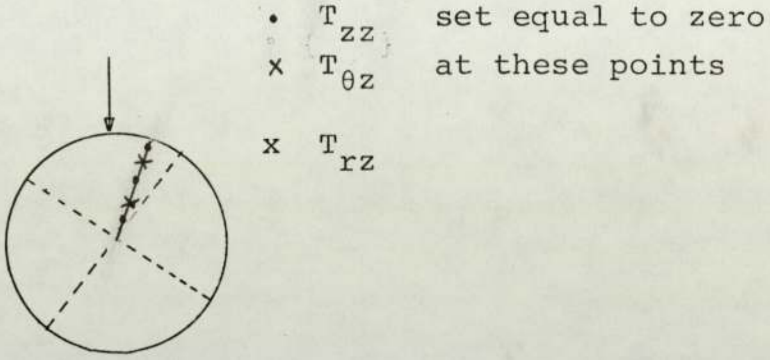

(a)

Bounday Conditions (1)

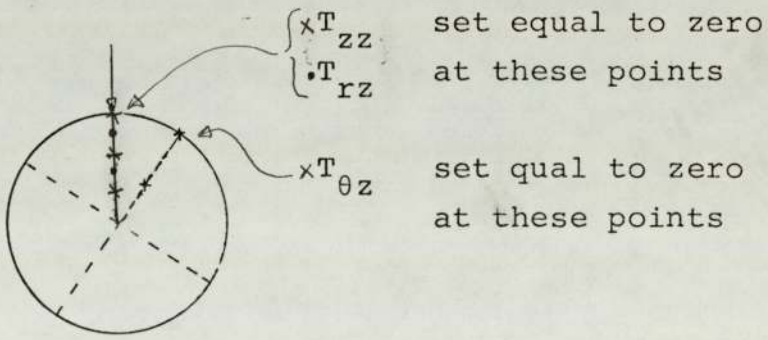

(b)

Boundary Conditions (2)

Approximate boundary conditions for antisymmetric end resonance investigation

Figure 3.4

Two sets of boundary conditions are shown in Figure 3.4 for an eight mode solution. In Figure 3.4a the stresses are set equal to zero along a radius at 45° to a reference normal stress mode. Although the figure applies to the (2,1) mode the boundary condition was used in the (3,1). Setting the radius at 45° allows the $\sin n\theta$, $\cos n\theta$ terms to be removed as a common factor. The results for the reflected complex mode for the (2,1) and (3,1) modes are shown in Figures 3.5 and 3.6 respectively. These modes indicate zero phase at Ω values of 2.05 in the case of the (2,1) mode and 2.83 for the (3,1) mode. The experimental results for nickel (σ=0.31) for the corresponding modes are 2.11 and 3.22. Applying boundary condition 2 of Figure 3.4, however, gave reflection coefficients which were not consistent with the first set of boundary conditions. In fact over the region plotted the two boundary conditions have nearly opposite phases around the experimental end resonance frequency. No obvious reason can be found to account for this sensitivity to the boundary condition approximation. The positions at which the stresses were set equal to zero were chosen to simplify the calculations. Perhaps a choice of points that minimise the average residual stresses would give more consistent results,this would however be an extremely lengthy procedure to implement.

FIGURE 3.5

Reflection coefficient of 2nd. antisymmetric mode -ve. complex conjugate

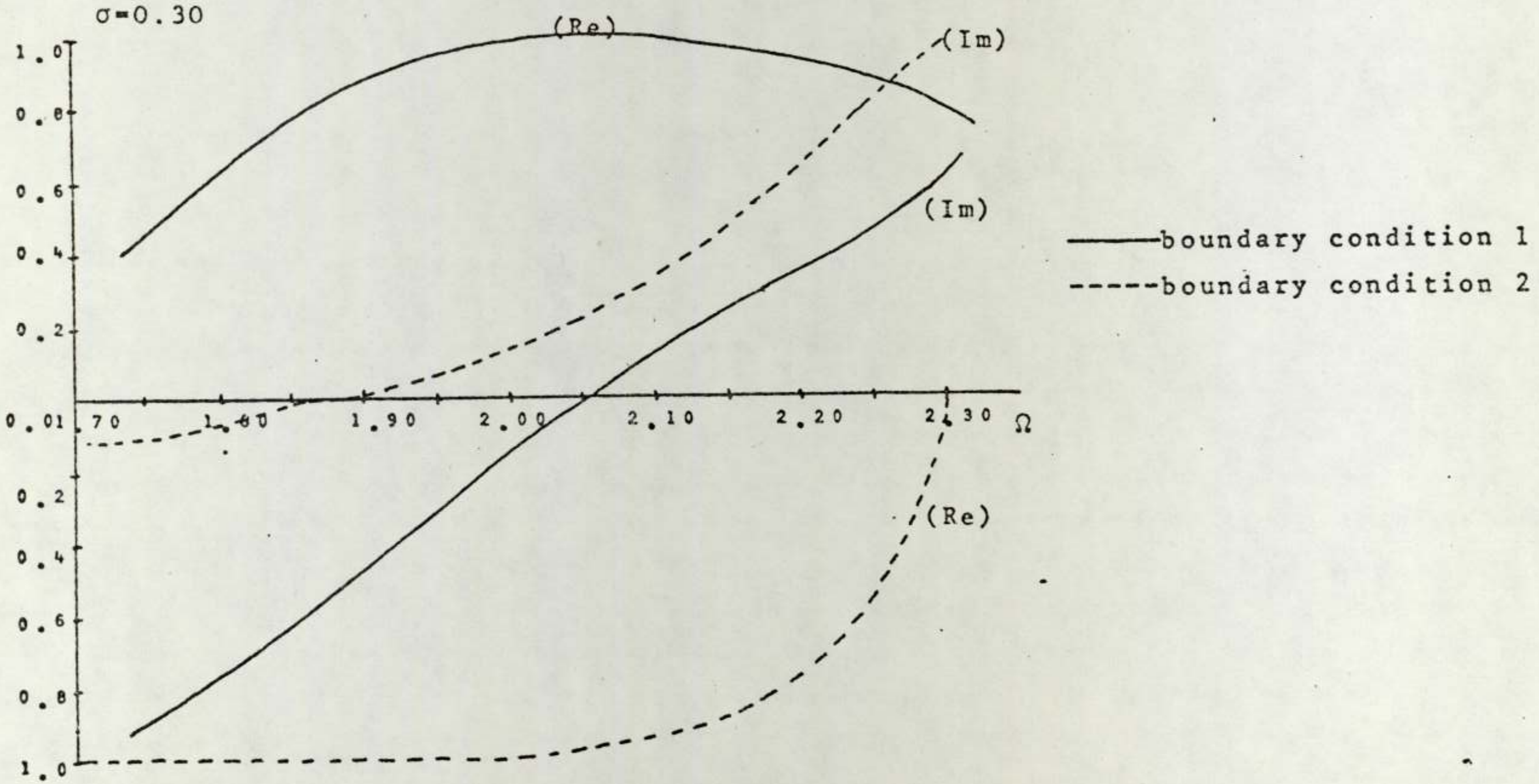

FIGURE 3.6

Reflection coefficient of 3rd. antisymmetric mode
-ve. complex conjugate
σ=0.3

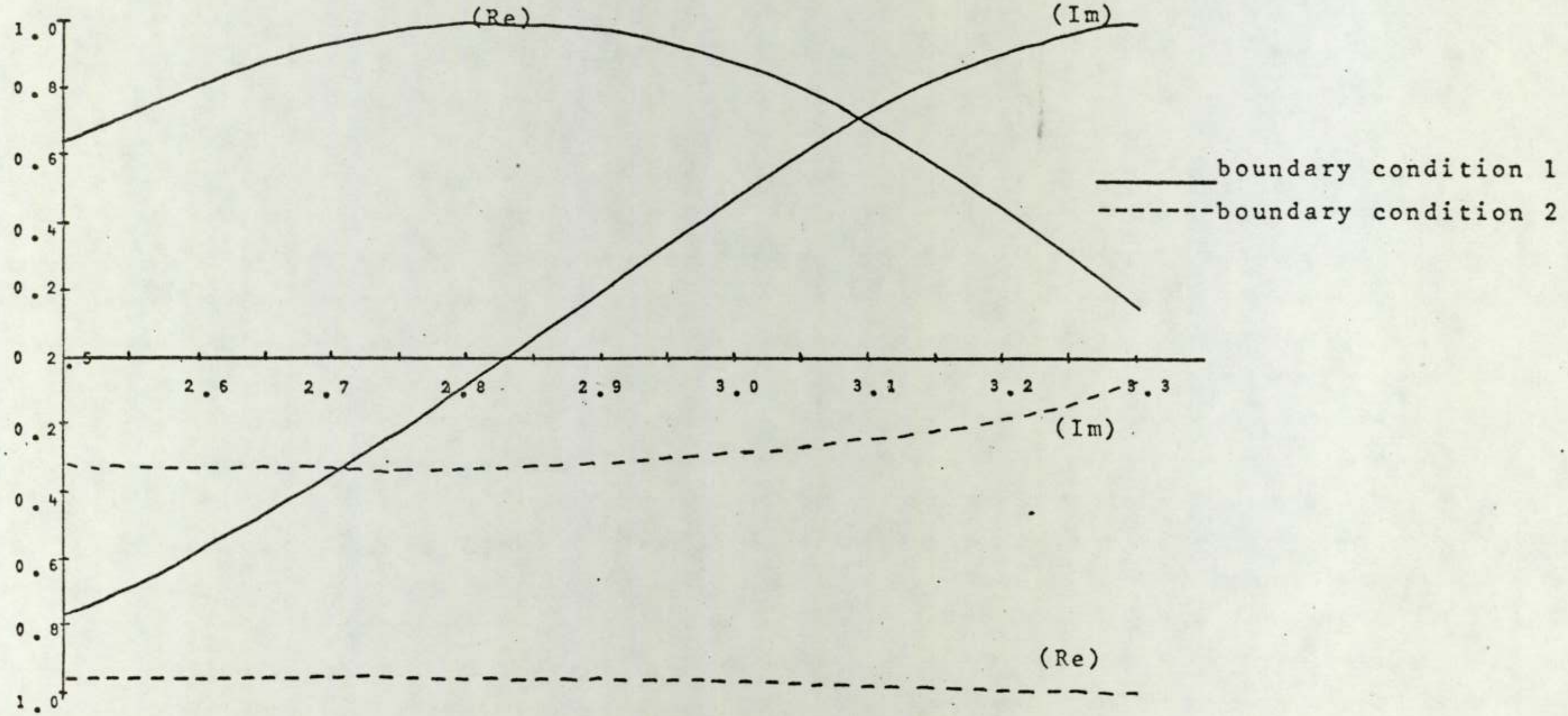

3.7 Discussion of Results

In the case of symmetric modes, the explanation of end resonance seems to be that at the end resonance frequency the amplitude of the complex mode rises very rapidly to cancel the residual stress resulting from the reflection of the propagating mode. This sharp increase in amplitude is shown in Figure 3.2 for Poisson's ratio of 0.30. The end resonance frequencies were calculated over the range of Poisson's ratio of 0.1 to 0.45. Table 3.2 shows a comparison of experimental points and the end resonance frequency obtained by calculation. Figure 3.6 is a comparison of the variation of theoretical cut-off frequency (Ω_c), thin disc frequency (Ω_d), and end resonance frequency(Ω_e), as a function of Poisson's ratio. It is apparent that the experimental point at σ=0.217 (soft glass) has a large error from the theoretical plot. It is likely that this is caused by lack of circularity and imperfections in the end of the bar. The transmission line was joined to the glass by a heat setting epoxy adhesive. The subsequent cooling of the bar caused small cracks to appear as a result of thermal stresses.

In each case shown in Table 3.2 a disc was cut from the end of the rod and its Poisson's ratio measured by the method described in Chapter 5. The shear velocity was also calculated which enabled the end resonant frequency parameter Ω_e to be calculated from equation (3.7.1).

$$\Omega_e = \frac{\omega a}{C_s} \qquad (3.7.1)$$

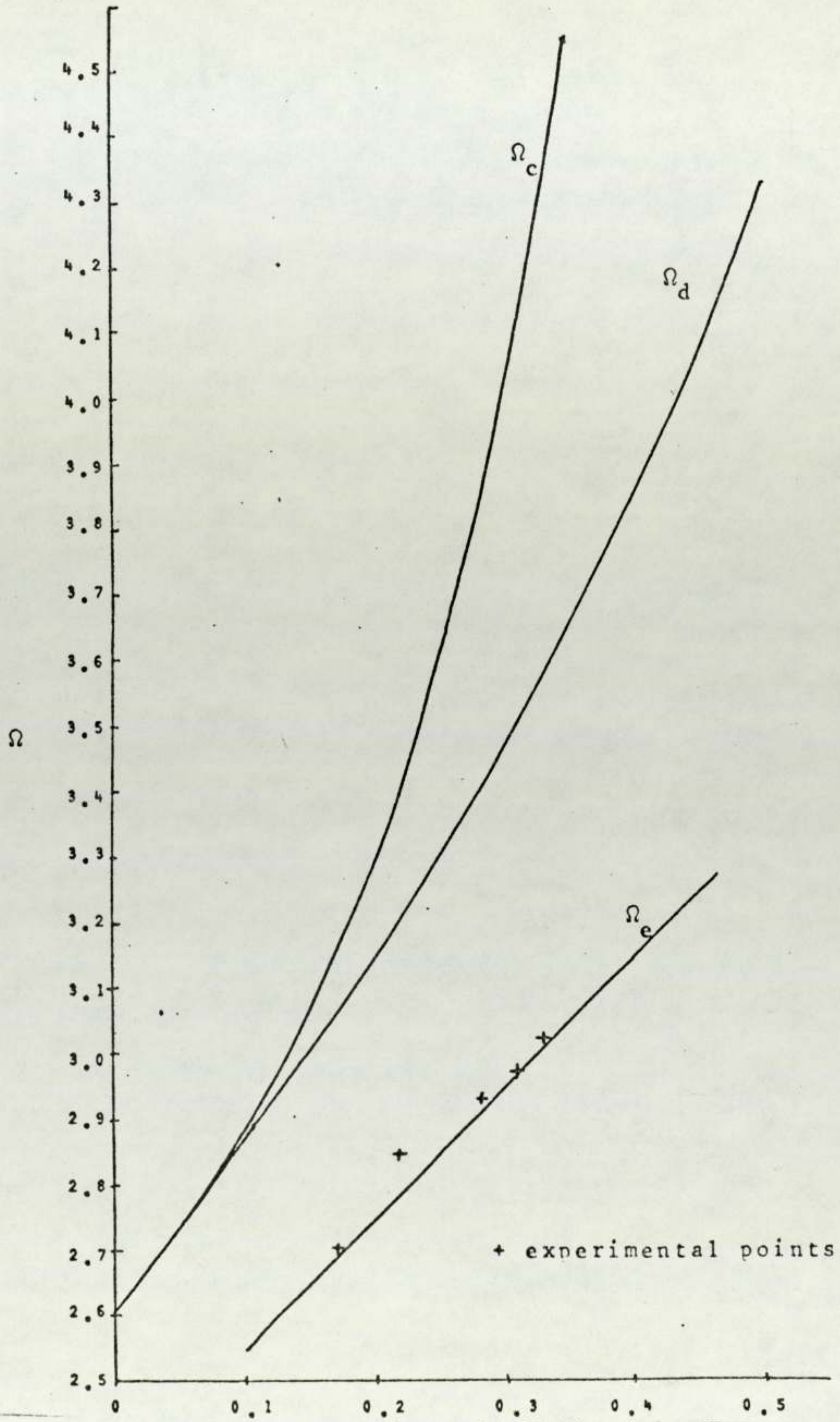

Poisson's Ratio (σ)
Comparison of end resonance disc and cut off frequencies for symmetric mode (n=0)

FIGURE 3.7

Poisson's Ratio σ	End Resonance Frequency Ω_e	Disc Frequency Ω_d	Cut-off Frequency Ω_c	$\frac{\Omega_c}{\Omega_e}$	$\frac{\Omega_d}{\Omega_e}$
0.10	2.5475	2.8553	2.8850	1.1325	1.12
0.15	2.6448	2.9920	3.0679	1.1600	
0.20	2.7434	3.1376	3.2940	1.2007	
0.25	2.8428	3.2940	3.5843	1.2608	
0.30	2.9426	3.4632	3.9769	1.3515	1.177
0.35	3.0427	3.6477	4.5521	1.4961	
0.40	3.1424	3.8509	5.5189	1.7563	
0.45	3.2406	4.0770	7.7127	2.3800	1.258

Comparison of end resonance , disc and cut-off frequencies of the symmetric mode

Table 3.1

Material	Poisson's Ratio σ	Calculated End Resonance Frequency Ω_e	Experimental End Resonance Frequency	% Difference
Pyrophylite	0.1730	2.69016	2.6999	+ 0.362
Glass	0.2172	2.7775	2.8428	+ 2.351
Mild Steel	0.2821	2.9068	2.9254	+ 0.640
Nickel	0.3099	2.9626	2.9695	+ 0.233
Aluminium	0.3300	3.0026	3.0166	+ 0.4662

Table 3.2

The experimental technique of determining resonances is discussed in Chapter 5, however, it is convenient to include the essential features of the technique here.

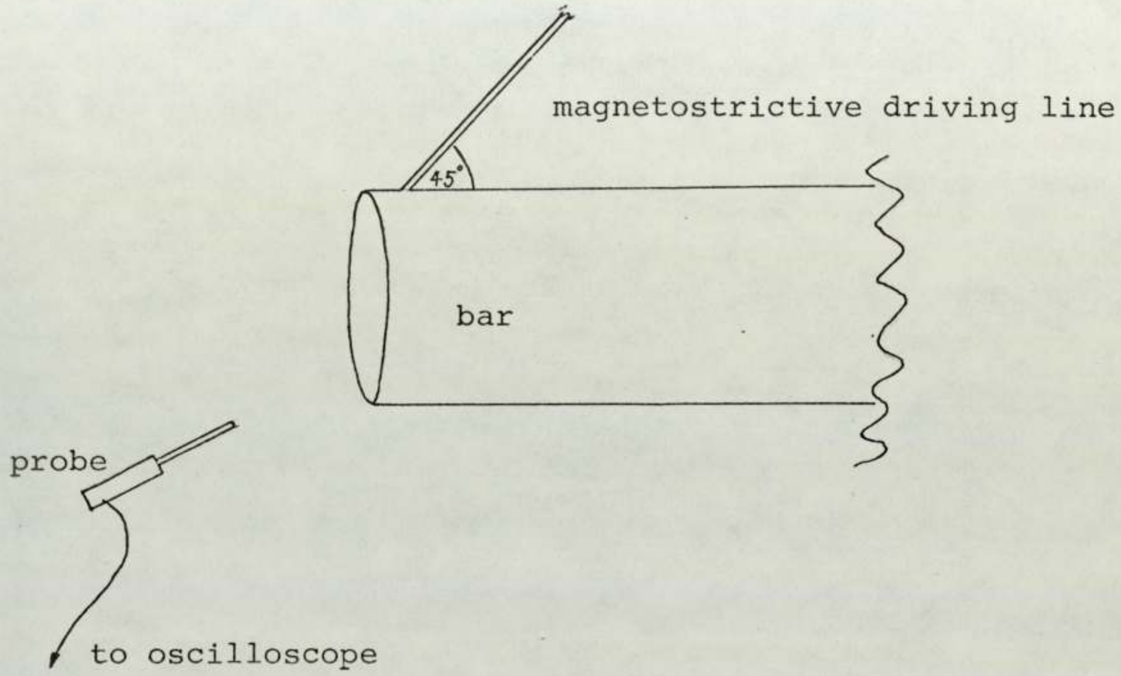

Figure 3.8

Vibrations are induced in the bar of Figure 3.8 via the magnetostrictive line which is a line of permandur or telcoseal of diameter between 0.5mm and 1.0mm. Stored energy re-radiates down the line and interferes with the launched burst. As explained in Chapter 5 the echo return displays a well defined null when the signal frequency is equal to the resonance frequency. It is this clearly defined phase effect that allows precise determination of the resonant frequency. The probe is a short length of magnetostrictive line with a coil to receive the vibrations. The probe is placed in contact with the end surface. The amplitude detected is the component of vibration in the direction of the wire. By comparing the phase of this signal with the echo, nodal areas can be mapped out. On crossing a nodal line the phase reverses. By suitable electronic gating circuits Lissajou figures,which greatly simplify this process, could be displayed.

The theoretical calculations of end resonance assume a semi-infinite bar, however, in these experiments the lengths of bars used were limited to the order of 300mm to 500mm. It is unlikely that this fact seriously influenced the experimental results since it was observed with the probe that vibrations could not be detected at a distance greater than about 50mm, from the end of the bar except for n=0. In addition heavy loading of the centre region of the bar with plasticene affected neither the frequency of end resonance, nor the amplitude of the received signal.

In the case of n=0 there is a very low amplitude propagating mode which is virtually undetectable midway down the line, but it produces high amplitudes at the remote end. An electrical analogue would be two tuned circuits of identical frequency coupled by a low impedance transmission line many wavelengths long. A more detailed study of this mode could be of value. This is as would be expected from the dispersion spectra shown in Chapter 2.

Results of the calculations of reflection coefficients for the antisymmetric modes with n=2 and n=3 for two sets of boundary conditions were not consistent. Figures 3.4 and 3.5 show the real and imaginary points of the reflection coefficients calculated at two different approximate boundary conditions. Boundary Condition 1 shown in the graphs is that the stresses are evaluated at equally spaced points along a radius that avoids any nodes. The centre and circular boundaries are not used since T_{rz} is already zero at this point. It has already been stated that there is no propagating mode associated with the antisymmetric vibration so it was anticipated that some phase characteristic may indicate end resonance. A possibility would have been that the complex reflection coefficients were exactly in phase at only one frequency as shown by the Boundary Condition 1 of Figures 3.4 and 3.5, the condition is that the reflection coefficients are both 1. That is at Ω=2.05 for n=2 and Ω=2.83 for n=3. The result given as Boundary Condition 2 established that the technique used is extremely sensitive to the choice of zero stress points. The Boundary Condition 2 is that T_{zz} and T_{rz} are calculated along a radius of their maximum amplitude and $T_{\theta z}$ is calculated along a second radius at its maximum amplitude.

The phase of the reflection coefficient for this boundary condition however, failed to establish any indication of end resonance. In view of the lack of encouragement from the results of the second and third antisymmetric modes nothing was to be gained from attempting higher order modes. A summary of the experimental observations of end resonance is given in Table 3.3.

Qualitative confirmation that the amplitude of vibration dies away with distance moved along the axis is obtained with the probe. This also confirmed that there is no resonance at the remote end of the bar. Figure 3.9 illustrates the results of probing the end surface of the 60 kHz end resonance in dural. The plus and minus signs denote the relative phase change across the nodes.

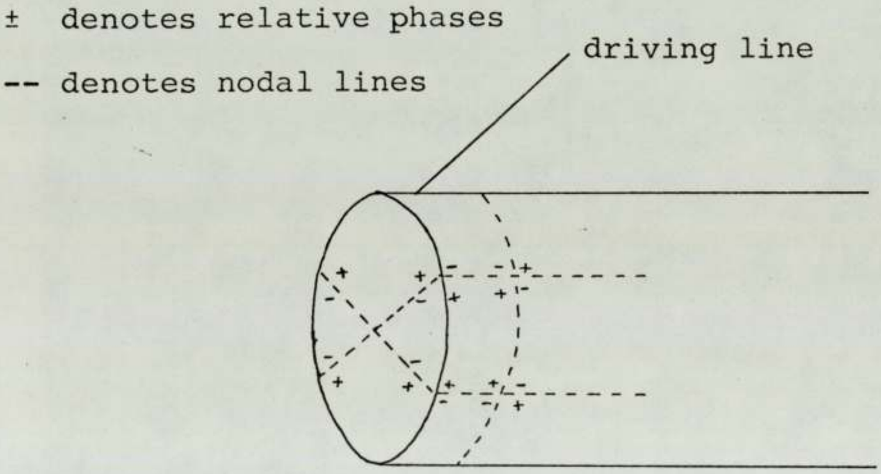

Phase relationship for non-axisymmetric mode end resonance (n=2)

Figure 3.9

A definite radial mode was observed on the circular surface of the bar, this occurred at 19.5mm from the end of the bar for the 60 kHz 2,1 mode in dural. The amplitude of vibration decayed rapidly so that a second node, if it exists, was not observed.

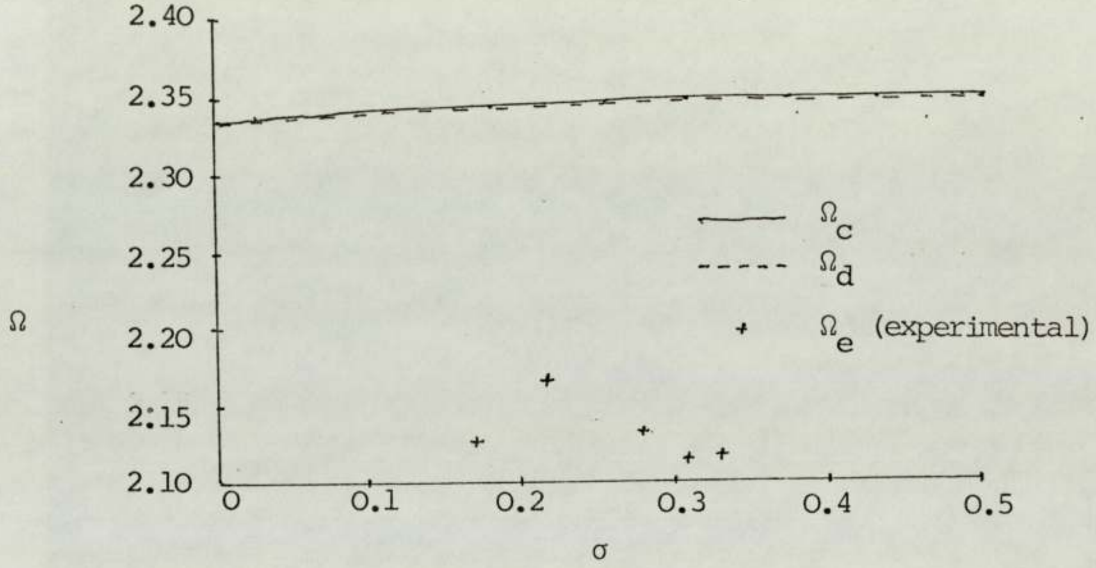

Comparison of Ω_c, Ω_d and Ω_e for n=2

FIGURE 3.10.1

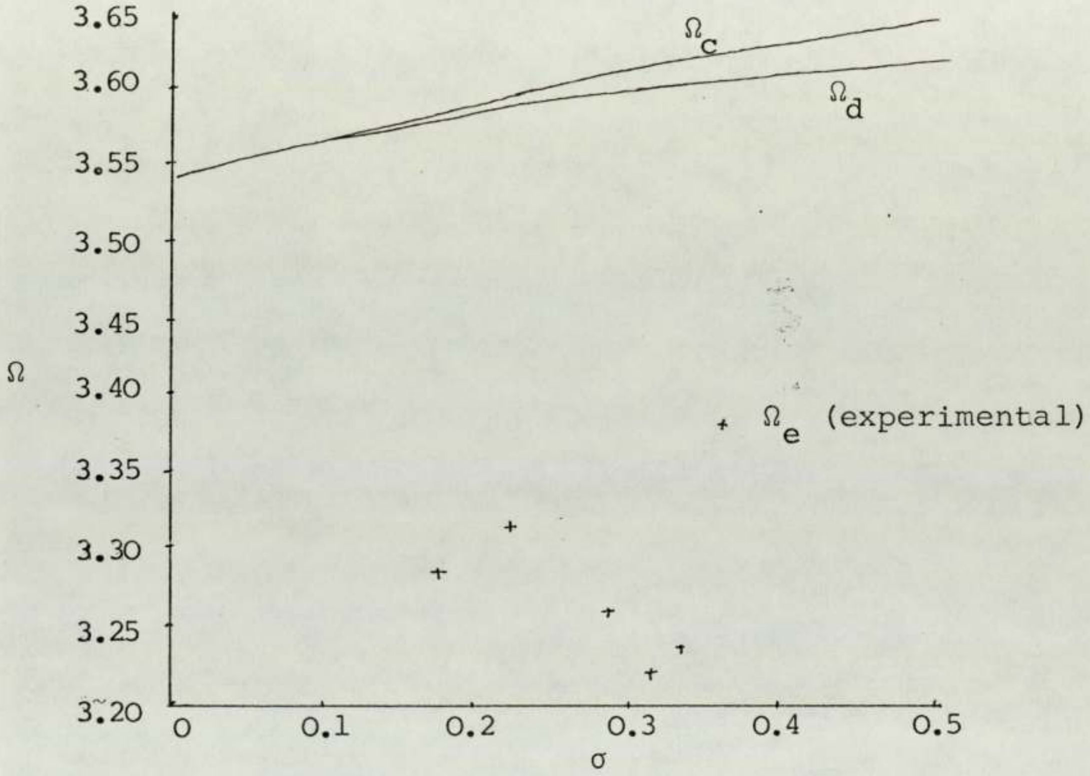

Comparison of Ω_c, Ω_d and Ω_e for n=3

FIGURE 3.10.2

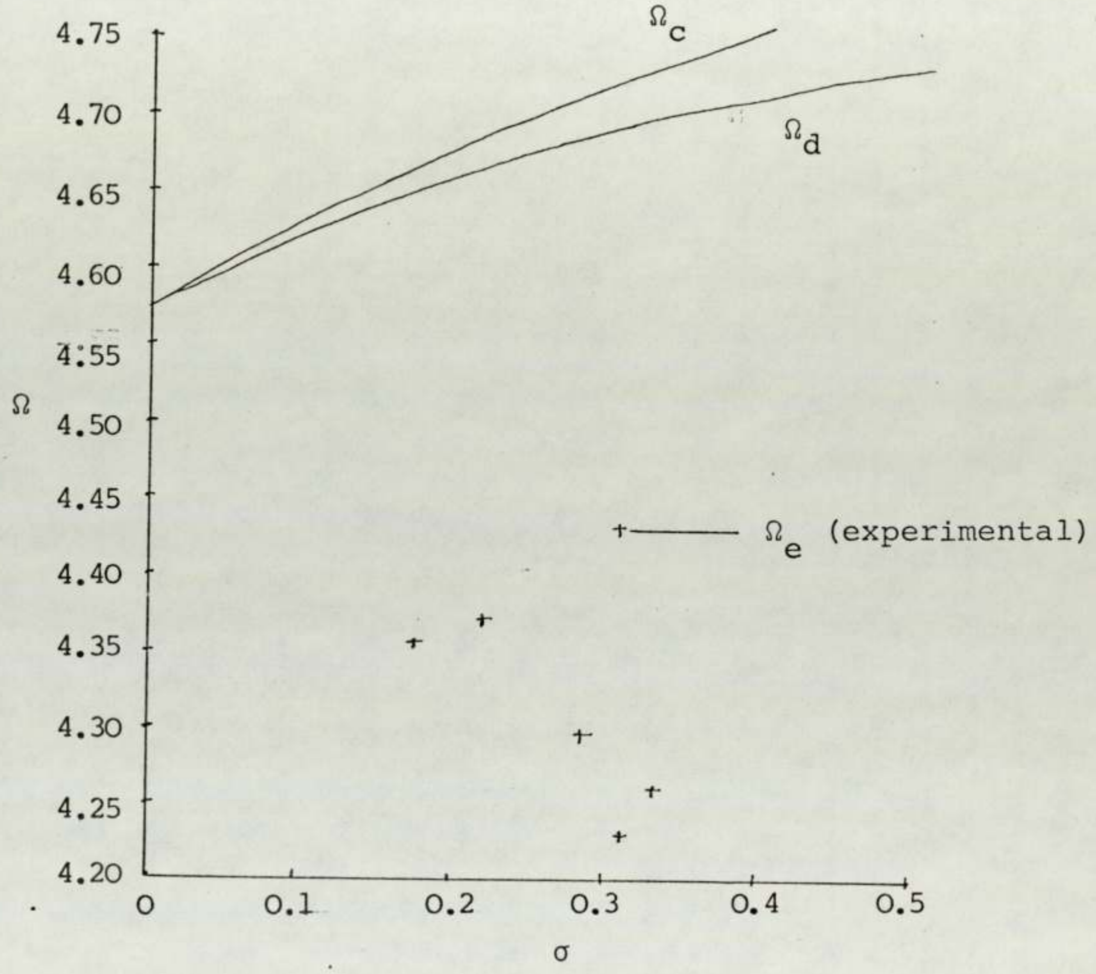

Comparison of Ω_c, Ω_d and Ω_e for n=4

FIGURE 3.10.3

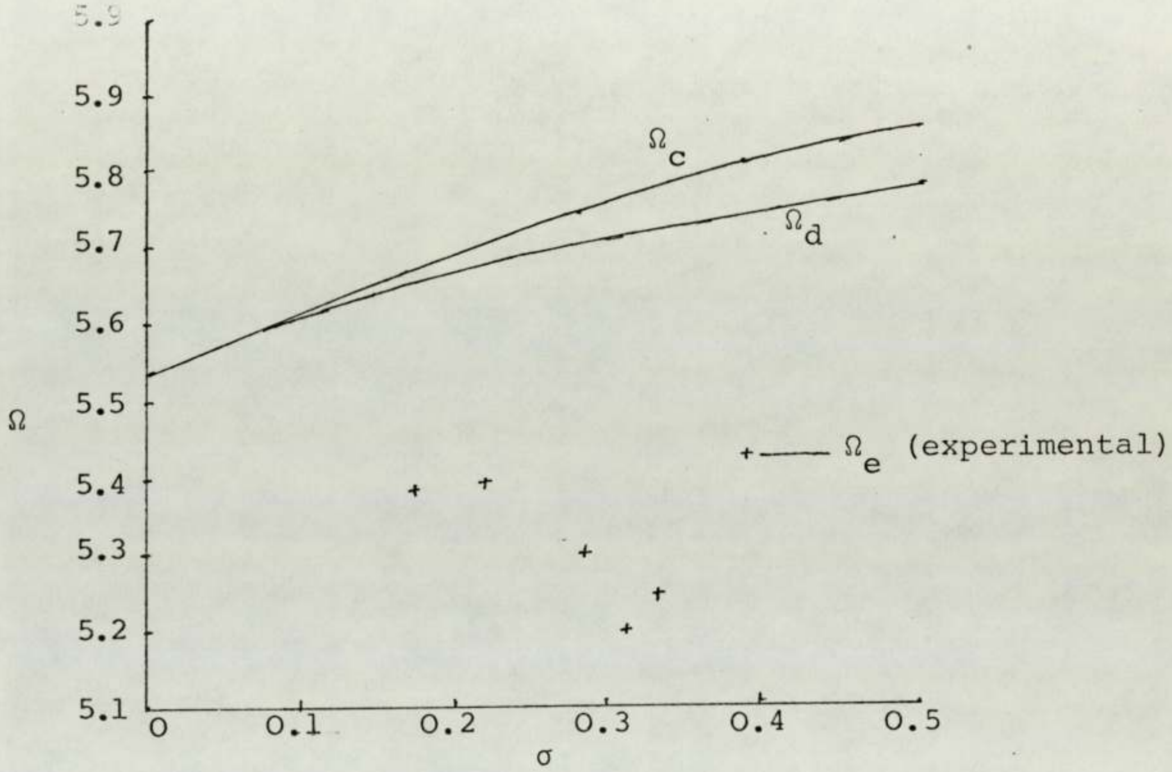

Comparison of Ω_c, Ω_d and Ω_e for n=5

<u>FIGURE 3.10.4</u>

MATERIAL BAR DIAMETER	POISSON'S RATIO σ	SHEAR VELOCITY ms^{-1}	MODE							
			2,1	0,1	3,1	4,1	5,1	6,1	7,1	
PYROPHYLITE	0.173	3473	91.71 KHz	116.50 KHz	141.77 KHz	187.77 KHz	232.14 KHz	275.52 KHz	318.01 KHz	f_e
25.62mm			2.1254	2.6999	3.2856	4.3516	5.3799	6.3853	7.3700	Ω_e
SOFT GLASS	0.217	3414	93.835 KHz	123.09 KHz	143.52 KHz	189.15 KHz	233.33 KHz	276.71 KHz	319.26 KHz	f_e
25.1mm			2.1670	2.8428	3.3145	4.3681	5.3885	6.3902	7.3729	Ω_e
MILD STEEL	0.282	3243	86.21 KHz	118.21 KHz	131.75 KHz	173.45 KHz	213.91 KHz	253.69 KHz	292.69 KHz	f_e
25.55mm			2.1335	2.9254	3.2606	4.2927	5.2957	6.2785	7.2436	Ω_e
NICKEL	0.310	3062	81.22 KHz	114.07 KHz	123.72 KHz	162.41 KHz	199.68 KHz	236.65 KHz	272.65 KHz	f_e
25.37			2.1142	2.9695	3.2206	4.2276	5.1980	6.1604	7.0974	Ω_e
DURAL	0.330	3128	60.53 KHz	86.31 KHz	92.62 KHz	121.80 KHz	150.11 KHz	177.73 KHz	-	f_e
34.8			2.1156	3.0166	3.2371	4.2569	5.2466	6.2120		Ω_e

Table 3.3

The phases indicated in Figure 3.9 are the phases of vibration normal to the surfaces of the bar since these are the only ones that the probe was capable of detecting with any certianty.

The theoretical cut-off frequencies and disc frequencies are compared to the experimental end resonance frequencies in Figures 3.9.1 to 3.9.4. The disc frequencies and cut-off frequencies have the same value at zero Poisson's ratio. In all cases the end resonance frequencies are well below cut-off of the lowest propagating mode. There is a distinct minimum in the experimental results for these values of end resonance. This does not occur in the experimental results of longitudinal mode (L(0,1)) end resonance and differs considerably from the forms of the curves for both Ω_c and Ω_d. This behaviour of the end resonance frequency seems to be a genuine phenomenon dependent on Poisson's ratio since the total error in measurement does not exceed 0.5%. Additional confidence is given by the fact that the experimental values for the L(0,1) mode shown in Figure 3.6 lie very close to the theoretical curve.

CHAPTER 4

THIN DISC SPECTRA

CHAPTER 4

THIN DISC SPECTRA

4.1 Introduction

In the previous chapter the variation of the end resonance frequency parameter with Poisson's ratio was given. The elastic constants were determined in each case by dynamic measurements from a disc cut from the end face at which the end resonance measurements were taken. Chapter 5 describes the practical technique used to measure the frequencies of the various modes required to obtain the elastic constants (Young's modulus and Poisson's ratio), of isotropic materials at high temperature. It is the purpose of this chapter to describe the theoretical basis of these measurements and to compile sufficiently comprehensive tables for accurate determination of the elastic constants from the thin disc spectra.

Love(3) established the general frequency equation for in plane vibrations of thin discs, however, no numerical calculations were carried out at that time. The frequency equation received little attention until Onoe(23,24) in 1956 published graphical data of the variation of the dimensionless frequency parameter. Holland(25) produced tables of results for the frequency parameter up to circular order 7 and up to the tenth zero of the frequency equation at the low circular orders. As in Chapters 2 and 3, the circular order corresponds to the number of nodal diameters of the disc and the mth zero corresponds to m nodal circles. Modes with n>0 are referred to as compound or contour extensional modes. Holland's numerical solutions of the frequency equation are evaluated at intervals of Poisson's ratio of 0.05 over the range of 0.25 to 0.5. It was found that in the case of graphite, discussed in Chapter 5, that the Poisson's ratios for the majority of samples tested lie below 0.2. The numerical values of the frequency parameter were calculated to extend these tables from Poisson's ratio of -0.5 to +0.5 in steps of 0.01.

The experimental technique used in Reference 25 is only applicable to piezo-electric materials since it relies on plated electrodes to excite the vibrations and involves switching the phases of the electrode components to select the various modes to be studied. The experimental technique given by Sharpe(26), involving the use of magnetostrictive transmission lines, eliminates this complication. It is also noted that with this technique the higher zeros, with the exception of the 0,2 and 1,2 modes are rarely excited. The spectra of the lowest solutions up to circular order 10 were calculated in addition to the 0,2 and 1,2 modes.

4.2 Thin Disc Wave Equation

The wave equations for a thin disc are given in terms of dilation and rotation (3).

$$\frac{\partial\Delta}{\partial x} - (1-\sigma)\,\frac{\partial\bar{w}}{\partial y} = \frac{\rho(1-\sigma^2)}{E}\,\frac{\partial^2 u}{\partial t^2} \tag{4.2.1}$$

$$\frac{\partial\Delta}{\partial y} + (1-\sigma)\,\frac{\partial\bar{w}}{\partial x} = \frac{\rho(1-\sigma^2)}{E}\,\frac{\partial^2 v}{\partial t^2} \tag{4.2.2}$$

Where Δ is areal dilation and $\bar{w}$ is rotational strain given by (4.2.3) and (4.2.4).

$$\Delta = \frac{\partial u}{\partial x} + \frac{\partial v}{\partial y} \tag{4.2.3}$$

$$2\bar{w} = \frac{\partial v}{\partial x} - \frac{\partial u}{\partial y} \tag{4.2.4}$$

To obtain a solution and hence a frequency equation, it is necessary to transform the above into cylindrical co-ordinates (26),(27). However, considerable simplification is apparent if the problem is treated in cylindrical co-ordinates from the beginning in a similar fashion to the treatment in Chapter 2.

The wave equation for thin disc is similar to equation (2.2.5) with a modification of the velocity term.

$$\nabla^2\phi = \frac{1}{C_p^2}\ddot{\phi} \qquad (4.2.5)$$

$$\nabla^2\bar{\psi} = \frac{1}{C_t^2}\ddot{\bar{\psi}} \qquad (4.2.6)$$

where

$$C_p^2 = \frac{E}{\rho(1-\sigma^2)} \qquad (4.2.7)$$

C_p is called the thin plate velocity and C_t, the torsional velocity has the same meaning as used previously.

4.3 Thin Disc Displacement Equations

For a thin disc (z is small) then u_z is approximately 0 and u_r and u_z independent of z. Hence $\bar{\psi}$ has only a ψ_z component. The radial and angular displacements are obtained from the usual definition of displacement in terms of scalar and vector potential (2.2.4).

With the omission of the exp(-jωt) term and noting that the equations no longer involve a function of z

$$u_r = \{AJ_n'(\alpha_1 r) + \frac{n}{r} CJ_n(\beta_1 r)\} \cos n\theta \qquad (4.3.1)$$

$$u_\theta = -\{\frac{n}{r} AJ_n(\alpha_1 r) + CJ_n'(\beta_1 r)\} \sin n\theta \qquad (4.3.2)$$

It will be noted that the radial and angular wave numbers (α and β) differ from those values in Chapters 2 and 3 and are now,

$$\alpha_1^2 = \frac{\omega^2}{C_p^2} \qquad (4.3.3)$$

$$\beta_1^2 = \frac{\omega^2}{C_t^2} \qquad (4.3.4)$$

4.4 Thin Disc Boundary Conditions

Using the fact that $T_{zz}=0$ to eliminate S_{zz} from equation (2.4.1), the stress equations for the thin disc become:

$$T_{rr} = \frac{2\lambda\mu}{\lambda+2\mu}(S_{rr}+S_{\theta\theta}) + 2\mu S_{rr} \qquad (4.4.1)$$

and

$$T_{r\theta} = 2\mu S_{r\theta} \qquad (4.4.2)$$

4.5 Thin Disc Frequency Equation

Applying the boundary condition of Section 4.4, at the circular boundary of the disc r=a gives the equation (4.5.1).

$$\begin{bmatrix} T_{rr} \\ \\ T_{r\theta} \end{bmatrix} = [a] \begin{bmatrix} A \\ \\ C \end{bmatrix} = 0 \qquad (4.5.1)$$

The frequency equation is given by the determinant of $|a|$ being equal to zero.

$$\begin{vmatrix} a_{11} & a_{12} \\ \\ a_{21} & a_{22} \end{vmatrix} = 0 \qquad (4.5.2)$$

The coefficient in terms of normalised variables in a form suitable for computation are;

$$a_{11} = -\{\frac{\bar{\alpha}_1^2}{1-\sigma} - n(n+1)\} J_n(\bar{\alpha}_1) + \bar{\alpha}_1 J_n(\bar{\alpha}_1)$$

$$a_{12} = 2n\{\bar{\beta}_1 J_{n-1}(\bar{\beta}_1) - (n+1) J_n(\bar{\beta}_1)\}$$

$$a_{21} = n\{(n+1) J_n(\bar{\alpha}_1) - \bar{\alpha}_1 J_{n-1}(\bar{\alpha}_1)\}$$

$$a_{22} = \{\bar{\beta}_1^2 - 2n^2-n\} J_n(\bar{\beta}_1) + 2\bar{\beta}_1 J_n(\bar{\beta}_1)$$

Putting n=0 in equation (4.5.2) leaves only the a_{11} and a_{22} terms in the determinant. The first term having only $\bar{\alpha}_1$

as its argument represents the pure radial modes and has the simple form of equation (4.5.3).

$$\frac{\bar{\alpha}_1 J_0(\bar{\alpha}_1)}{J_1(\bar{\alpha}_1)} = 1-\sigma \qquad (4.5.3)$$

The second term a_{22} has only $\bar{\beta}_1$ as its argument and is given by equation (4.5.4).

$$\frac{\bar{\beta}_1 J_0(\bar{\beta}_1)}{J_1(\bar{\beta}_1)} = 2 \qquad (4.5.4)$$

This term represents the torsional mode solution and has only a u_θ displacement component. Since all the above frequency equations are solved for $\bar{\alpha}_1$ as a function of Poisson's ratio, the equation (4.5.4) also depends on Poisson's ratio. The relationship between the shear and radial wave numbers is given by (4.5.5).

$$\frac{\bar{\beta}_1^2}{\bar{\alpha}_1^2} = \frac{2}{1-\sigma} \qquad (4.5.5)$$

4.6 The Thin Disc Spectra

The dimensionless frequency parameter above $\bar{\alpha}_1$ is renamed $K_{n,m}$ in the table given in Appendix A.4.1. The subscripts of the K parameter indicate the modes in an identical way to those of Chapters 2 and 3.

Thus

$$\bar{\alpha}_1 = K_{n,m} = \frac{\omega a}{C_p} \qquad (4.6.1)$$

The frequency could equally well be normalised to the shear velocity as used in Chapters 2 and 3. The relationship is shown in equation (4.6.2).

$$\Omega_{n,m} = K_{n,m}(2/(1-\sigma))^{\frac{1}{2}} \qquad (4.6.2)$$

The result of the solution of the frequency equation is given in the spectra of Figure 4.1 in terms of K. Values of $K_{n,m}$ as a function of Poisson's ratio are given in Appendix 4.1. The solution of the torsional modes is not given since it requires a modification to the method used to excite radial and contour extensional (compound) vibrations. For this reason it is not of interest in the measurement of Poisson's ratio via the method described here.

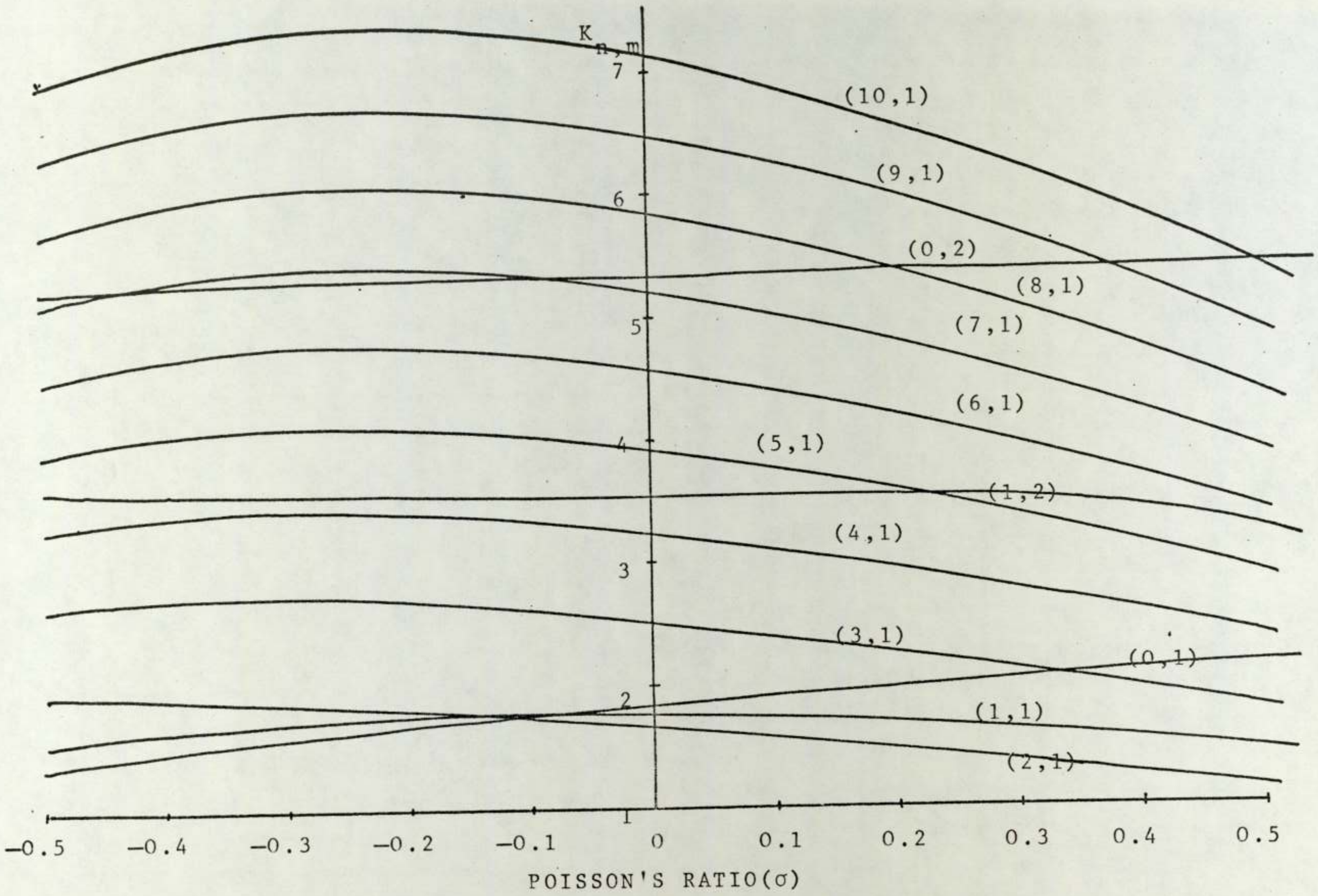

Spectrum of disc modes v. Poisson's Ratio

FIGURE 4.1

4.7 Determination of Poisson's Ratio from Thin Disc Spectra

It is clear from Figure 4.1 that the contour extensional modes, that is the (2,1); (3,1); (4,1)etc., have a decreasing frequency with increasing positive Poisson's ratio. In contrast the first and second radial modes (0,1) and (0,2) show an increasing frequency with increasing Poisson's ratio. Also the second root of the first flexural mode (1,2) has nearly zero slope below $\sigma=0.35$ and intersects the (5,1) flexural mode at approximately $\sigma=0.23$. The terms contour extensional and flexural are used interchangeably since the disc contour extensional modes show close resemblance to the flexural end resonance modes discussed in Chapter 3.

Since the spectra of the various modes shown in Figure 4.1 have varying dependence on Poisson's ratio, comparison of two modes will give a measure of Poisson's ratio. If $f_{n,m}$ is the mode frequency obtained by experiment, then,

$$\frac{f_{n,m_1} - f_{n,m_2}}{f_{n,m_2}} = \frac{K_{n,m_1} - K_{n,m_2}}{K_{n,m_2}} = g(\sigma) \qquad (4.7.1)$$

The frequencies of the modes can be measured experimentally with high accuracy, typically better than 0.1%. The ratio $g(\sigma)$ can be obtained from the theoretical dimensionless frequency parameters K in Appendix 4.1.

It would be possible to use a combination of any two modes but it is clear that certain combinations will give

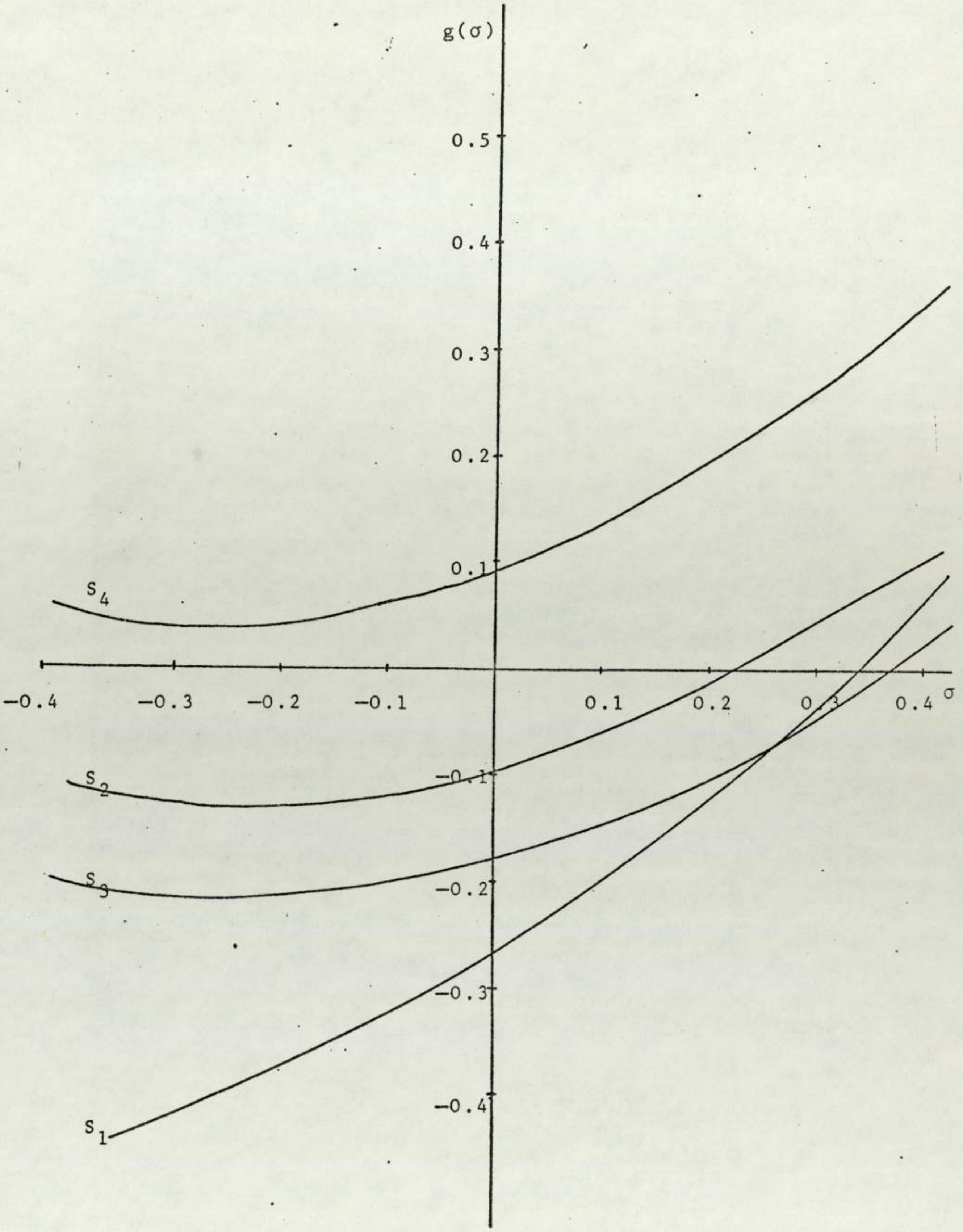

Sensitivity ratios for Poisson's ratio measurement

<u>FIGURE 4.2</u>

better sensitivity than others. Where possible it is desirable to choose modes with opposite slopes. Such a combination is given by the (0,1); (3,1) pair of modes. To allow for all possible values of Poisson's ratio it is necessary to tabulate $g(\sigma)$ for other combinations. This becomes necessary because at or close to the points of intersection it is often not possible to decide the exact resonant frequency as a result of coupling between the two modes. Four combinations of modes $g(\sigma)$ are tabulated in Appendix 4.2.

The sensitivity of the mode comparisons chosen is not constant with σ and some combinations have better sensitivity than others. The function $g(\sigma)$ is plotted in Figure 4.2 for the four mode comparisons generally used. They are:

$$S_1 = \frac{K_{0,1} - K_{3,1}}{K_{3,1}}$$

$$S_2 = \frac{K_{1,2} - K_{5,1}}{K_{5,1}}$$

$$S_3 = \frac{K_{0,2} - K_{9,1}}{K_{9,1}}$$

$$S_4 = \frac{K_{1,2} - K_{4,1}}{K_{4,1}}$$

For positive Poisson's ratio, the frequency ratio S_1, shows greatest sensitivity in Poisson's ratio since it has the largest slope in Figure 4.2. At around $\sigma=-0.1$, S_1 still

Frequency (kHz)	Mode	$K_{n,m}$	
		Experiment	Calculated
68.96	2,1	1.400	1.407
100.08	0,1	2.032	2.036
105.86	3,1	2.149	2.144
137.67	4,1	2.795	2.792
167.41	5,1	3.398	3.399
196.12	6,1	3.982	3.986
223.49	7,1	4.546	4.563

$(h/d) = 0.094$

$\sigma = 0.284$ (Steel)

Table 4.1

Thin Disc Frequencies for Steel

Frequency (kHz)	Mode	$K_{n,m}$	
		Experiment	Calculated
46.77	2,1	1.358	1.358
71.87	3,1	2.087	2.086
93.53	4,1	2.717	2.718
114.03	5,1	3.311	3.311
121.3	1,2	3.522	3.520
133.75	6,1	3.883	3.884
152.9	7,1	4.439	4.447

$(h/d) = 0.096$

$\sigma = 0.33$ (Aluminium)

Table 4.2

Thin Disc Frequencies for Aluminium

Material	Mode	2,1	3,1	4,1	5,1	6,1	7,1	0,1
Nickel σ=0.315 (h/d=0.127)	Ω_d	2.340	3.599	4.691	5.716	6.702	7.667	3.512
	Ω_e	2.114	3.221	4.228	5.198	6.160	7.097	2.969
	Ω_c	2.348	3.617	4.723	5.763	6.768	7.755	4.125
	Ω_d/Ω_e	1.107	1.117	1.110	1.100	1.088	1.080	1.183
	Ω_d/Ω_c	0.997	0.995	0.993	0.992	0.990	0.989	0.851
Steel σ=0.282 (h/d=0.125)	Ω_d	2.345	3.601	4.685	5.703	6.685	7.655	3.411
	Ω_e	2.134	3.261	4.293	5.294	6.279	7.244	3.261
	Ω_c	2.347	3.610	4.710	5.744	6.741	7.720	3.821
	Ω_d/Ω_e	1.099	1.104	1.091	1.077	1.065	1.057	1.046
	Ω_d/Ω_c	0.999	0.998	0.995	0.993	0.992	0.992	0.893
Glass σ=0.217 (h/d=0.126)	Ω_d	2.354	3.604	4.678	5.657	6.649	7.596	3.203
	Ω_e	2.159	3.303	4.352	5.369	6.367	7.346	2.833
	Ω_c	2.345	3.598	4.683	5.699	6.679	7.642	3.364
	Ω_d/Ω_e	1.090	1.091	1.075	1.054	1.044	1.034	1.131
	Ω_d/Ω_c	1.004	1.004	0.999	0.993	0.996	0.994	0.952
Pyrophylite σ=0.171 (h/d=0.128)	Ω_d	2.343	3.593	4.661	5.599	6.614	7.371	3.061
	Ω_e	2.125	3.286	4.352	5.380	6.385	7.370	2.700
	Ω_c	2.343	3.588	4.661	5.666	6.638	7.592	3.152
	Ω_d/Ω_e	1.102	1.093	1.071	1.041	1.036	1.000	1.134
	Ω_d/Ω_c	1.000	1.001	1.000	0.988	0.996	0.971	0.971

Table 4.3

has the largest slope but the sensitivity is unusable since it is seen from Figure 4.1 that the three lowest modes intersect at this value and experimentally the modes become very difficult to separate. It is shown in Chapter 5 that this is the value of σ for pyrolytic graphite. For this reason the ratio S_4 would be used in this region. While it is only necessary to find one ratio of frequencies to obtain values of σ, in practice more than one ratio is used since this gives a test of the overall measurement technique.

4.8 Effect of Finite Disc Thickness

The accuracy of determination of Poisson's ratio from thin disc depends on the accuracy with which the thin disc theory represents the practical case where the discs have a finite thickness. As stated in previous chapters, there is no exact theory for cylindrical solids of arbitrary dimensions. Moseley(28) and Lucey(29) give corrections to the frequency of vibration for the radial mode vibration. These corrections are given in terms of the radial mode eigenvalue by equations (4.8.1) and (4.8.2) corresponding to Moseley's and Lucey's correction respectively.

$$K_{0,1} = K^T_{0,1} \left[1 - \frac{1}{6}\left\{ \frac{K^T_{0,1}\sigma}{(1-\sigma)\eta} \right\}^2 \right] \qquad (4.8.1)$$

$$K_{0,1} = K^T_{0,1} \left[1 - \frac{1}{3(1-\sigma^2)} \left(\frac{2K^T_{0,1}}{\pi\eta}\right)^2 \right]^{\frac{1}{2}} \qquad (4.8.2)$$

Where $K_{0,1}$ is the corrected eigenvalue with $K^T_{0,1}$ being the thin disc eigenvalue. η is the thickness to diameter ratio. Taking $\sigma=0.3$ for a thickness to diameter ratio of 0.125 equation (4.8.1) predicts a correction to the lowest radial mode eigenvalue of 0.2% and equation (4.8.2) predicts 0.4%. Provided the thickness to diameter ratio is sufficiently small (of the order of 1/10) then the corrections are negligible. Correction factors for the contour extensional modes are not available in the literature but Ambati(51) has shown experimentally that the effect of thickness on the resonant frequency is always less than that of the radial mode vibrations. Tables 4.1 and 4.2 compare calculated and experimental values of the disc resonant frequencies for steel and aluminium.

Disc resonance and end resonance experimentally obtained frequencies are compared with theoretical cut-off frequencies in Table 4.3. The ratios Ω_d/Ω_e and Ω_d/Ω_c are given. As Poisson's ratio decreases, the disc frequencies and cut-off frequencies approach the same value, i.e. the ratio Ω_d/Ω_c approaches 1 for all modes.

CHAPTER 5

MEASUREMENT OF ELASTIC CONSTANTS

CHAPTER 5

MEASUREMENT OF ELASTIC CONSTANTS

5.1 Introduction

Methods of measuring the dynamic elastic moduli of materials generally fall into two distinct groups(30). The two major categories are resonance and time of flight techniques. The resonance method requires a high material Q and with metals can normally be used up to about 70% or 80% of their melting point. Resonance measurement of thin discs however, have a wide range of application particularly in the measurement of the elastic constants of metals and ceramics. Specimens are easily manufactured to high tolerances and sample sizes of about 1 cm diameter usually have the first 8 or 9 resonances occurring at frequencies below 200 kHz. Resonances up to this frequency can be readily excited using magnetostrictive delay line techniques.

Because the identification of resonance depends on the phase change phenomenon described later in this chapter, high precision is attainable. The reproducibility for a 'Q' factor of 100 is better than 0.05%. An approximation inherent in the derivation of the frequency parameters given in Chapter 4 is that no allowance is made for losses in the material and for acoustic coupling from the driving line into the resonator. The effect of this is discussed in Section 5.3 where simple calculations show that provided care is taken the effect of the driving line (the major effect) can be made negligible.

Although time of flight methods of measurement are discussed in later chapters a comparison with resonant techniques could be introduced here. Time of flight methods are capable of measuring materials with much lower Q, that is in materials with high losses or at temperatures beyond which the null indication of resonance cannot be obtained. That is to say time of flight methods can extend elastic constant measurement much closer to the melting point of metals. Sensitive measurements of the variation of flight time of a pulse can be obtained fairly readily. A system is described in Chapters 6 and 7 which will track these variations automatically once the instrument is initially locked onto the flight time.

Returning to resonance methods for the remainder of this chapter, the magnetostrictive transmission line method of exciting vibration is particularly suited to measuring the variation of the elastic constants of refractory materials with temperature. The transmission line itself can be chosen for its refractory properties and only the transducer portion needs to be a magnetostrictive material . For example the lead-in line into the furnace could be made from the same material under test and the low temperature portion of the transmission line could be steel with a magnetostrictive portion at the end. The overall length of the line has to be sufficiently long to accommodate the anticipated maximum number of oscillations in a burst at the lowest frequency used, about 100 oscillations is generally a suitable figure to use but may necessitate a long line at low frequencies.

The majority of measurements described in this chapter were carried out on graphite discs supplied by PERME Westcott. Because of their refractory properties graphites are widely used in the manufacture of rocket motors. However, engineering design data at high temperatures is lacking because of the absence of a simple technique for measuring the variation of elastic constants at high temperatures. The simplicity of the thin disc and delay line combination is ideal for this application since it enables large numbers of measurements to be taken to form a data base for material comparisons. Results obtained for a variety of graphite grades are given for temperatures up to 1000°C, are presented. Pyrolytic graphite is a highly anisotropic material but is almost isotropic in the plane of deposition, that is the plane of the disc sample. It was found to have a negative Poisson's ratio in the plane of the disc.

Of major importance in the use of thin disc measurements is to establish the relative positions of the resonant modes with absolute confidence. Although this is usually simple at some values of Poisson's ratio the modes merge and it can be difficult to identify them. The methods used to resolve the modes are given below. Although only two frequencies are needed to obtain both Young's modulus and Poisson's ratio it is worthwhile investigating resonances up to about circular order 7, at least at room temperature. It is apparent from Chapter 4 that the ratio $K_{n,m}/f_{n,m}$ is constant for all values of n and m and this ratio gives a useful check on the correct identification of the resonant modes. Several mode comparison ratios are given in Appendix A4.2 and consistency between independent measurements of Poisson's ratio is a further confirmation of their identity.

Anisotropy can sometimes be introduced into graphites as a result of the manufacturing process. Although this is not normally noticeable in the disc specimens occasionally the anisotropy is sufficient to cause the low frequency modes to show two closely spaced resonant frequencies. Also in contrast to the isotropic materials tested, the nodal positions are not wholly dependent on the position of the driving line. It was found that attaching the line to various positions on the periphery allowed a position to be found that excited only one resonance. Using this position gave consistent values of the $K_{n,m}/f_{n,m}$ ratio indicating correct mode identification. In the absence of solutions to the wave equations for generally anisotropic materials this was the procedure adopted at room temperature and the high temperature results were taken with this drive position.

5.2 Transmission Line Technique

A schematic representation of the transmission line and resonator layout is shown in Figure 5.1. A block diagram of the associated electronic system is given in Figure 5.2. Although a disc resonator is shown in Figure 5.1, the transmission line technique can be applied to a resonator of any arbitrary geometry. In addition the shape of the echo that is seen on the oscilloscope is independent of the exact shape of the resonator. In various applications discs, rods, plates and tuning forks have been used(27, 32, 33). This method was of course used to obtain the end resonant frequencies of cylinders described in Chapter 3.

The source of excitation of the resonator is the burst frequency oscillator. A preselected number of cycles are gated through to the buffer amplifier at a rate determined by the pulse repetition frequency (p.r.f.) oscillator. This frequency is chosen so that the signal reverberation on the line has decayed sufficiently to avoid interference with the next transmitted burst. If the p.r.f. oscillator frequency is too high the crossover (Figure 5.3) will be obscured by reverberation from the previous transmission but conveniently this can be distinguished from say a lossy resonator picture from noise preceding the sharp rising edge of the next burst.

The transmit/receive switch can be as simple as two back to back diodes in series with a resistor, the oscilloscope being connected across the diodes. This limits the peak

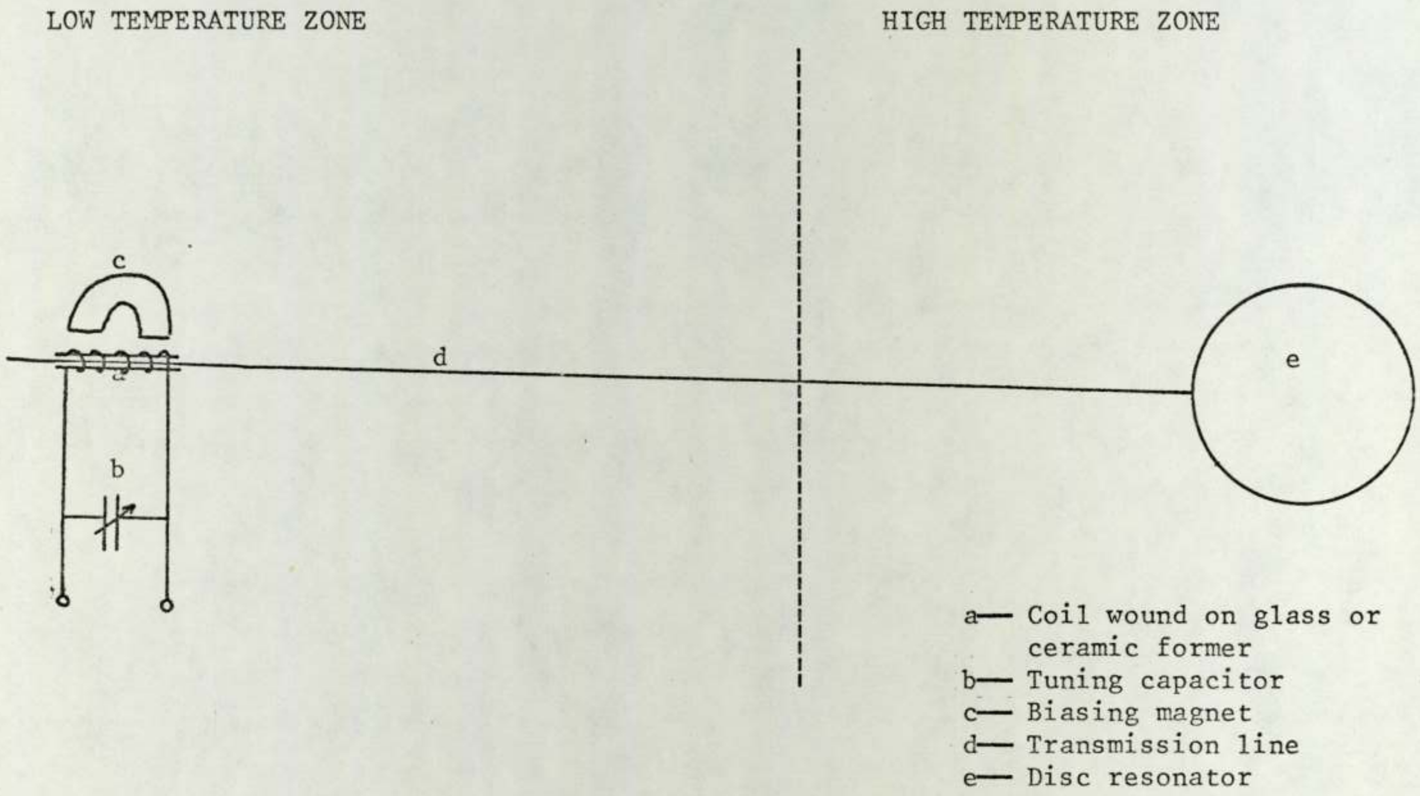

Experimental transmission line technique
FIGURE 5.1

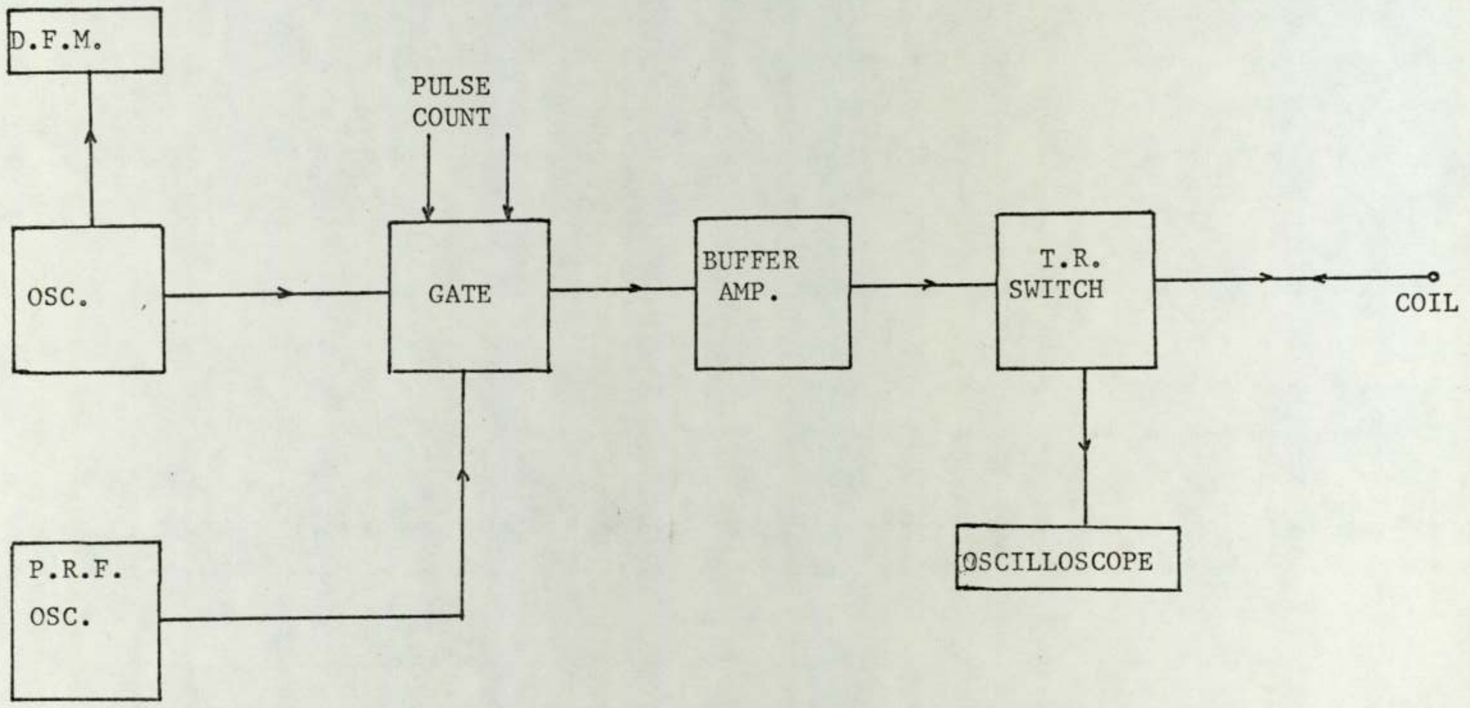

Block diagram of electronics for elastic constant measurement

FIGURE 5.2

amplitude of the signal to about 1.2V p-p. Using a transmitted signal of 30V p-p and a coil tuned to the transmitted frequency the two way insertion loss is such that the maximum echo signal is about 800 mV p-p.

The frequency of the burst oscillator is adjusted until the resonant frequency is detected by the cross-over criterion, discussed in Section 5.3. An alternative to the cross-over method is to measure the frequency of the excitation burst and compare this value with the frequency of the decrement part of the echo return. This is the part of the echo signal from the free vibration of the resonator that occurs after the excitation burst. Since the frequency of the decrement signal is at the resonant frequency, Fathimani(34) used a closed loop control system to maintain an oscillator at the resonator frequency.

5.3 The Echo

The modulation envelope of the echo is shown in Figure 5.3a, and a typical echo oscilloscope photograph in Figure 5.3b.

Sharpe$^{(35)}$ has analysed the case of a line resonator and transmission line combination in the Laplace domain. The expression for the first reflected echo is given by equation (5.3.1) where $V_1(s)$ represents the forcing function.

$$V_E(s) = \frac{Z_1(s) - Z_2(s)\tanh(\gamma\ell)}{Z_1(s) + Z_2(s)\tanh(\gamma\ell)} V_1(s) \qquad (5.3.1)$$

Equation (5.3.1) shows that the transfer function is the usual reflection coefficient from a boundary, which in this case has a terminating impedance of $Z_2(s)\tanh(\gamma\ell)$. Using a numerical inversion technique a good representation of the echo was obtained. It is interesting to compare the echo envelope obtained in Reference 35 with the reflection of a rectangular pulse on a string from an elastic boundary in Graff$^{(13,pp33)}$. The reflected pulse undergoes considerable distortion and shows very close similarities with the envelope of Figure 5.3a. The exception being that there is no increase in amplitude immediately before the decrement part of the signal.

The equation (5.3.1) is not,of course, directly applicable to the line-disc resonator combination since the load impedance

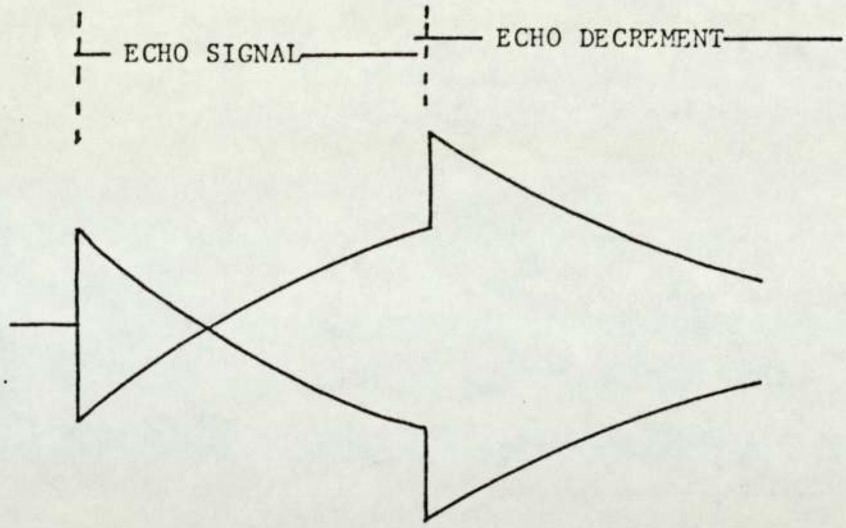

FIGURE 5.3.a

The echo

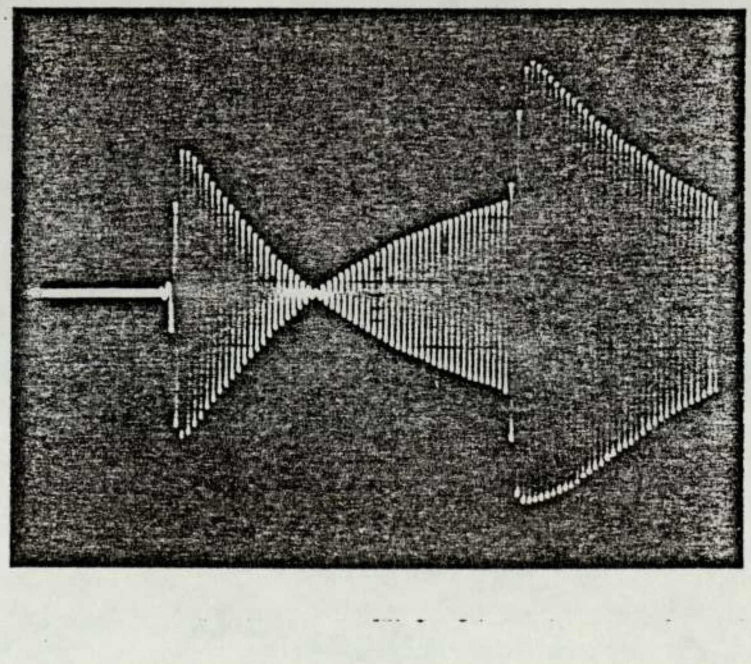

FIGURE 5.3.b

of the resonator will depend on the mode and the geometric form of the resonator. The mechanical impedance is defined by equation (5.3.2),

$$Z_m = \frac{F}{V} \tag{5.3.2}$$

and Glazanov$^{(38)}$ has shown that for the radial mode of vibration of a disc the impedance takes the form of equation (5.3.3),

$$Z_m = -j\rho C_p A \left| \frac{J_o(k_p a)}{J_1(k_p a)} - \frac{(1-\sigma)}{k_p a} \right| \tag{5.3.3}$$

where A is the effective area of coupling between the line and disc, and $k_p = s/C_p$.

A similar equation to (5.3.3) could be obtained for the contour extensional modes, noting the term in the square bracket corresponds to the frequency equations given in Chapter 4.

The transfer function of (5.3.1) yields a harmonic spectrum of poles and these poles can be obtained in explicit form. However, when the transmission line is terminated by an impedance of the type given by (5.3.3), this will not be true. The poles of (5.3.3) could be obtained experimentally or by numerical techniques to obtain s. This has not been carried out owing to the complexity involved for radial and contour extensional modes, and also, the results are unlikely to lead to any new information not already obtained experimentally. The difference is that changing the terminating impedance merely shifts the location of the poles in the s plane.

The effect of line impedance on the resonator frequency is of importance since this determines the accuracy with which material constants are calculated. The displacement equation of a lossy resonator is given by (5.3.4) where Q is the total Q of the system and

$$\frac{\partial^2 u}{\partial t^2} + \frac{\omega_o}{Q}\frac{\partial u}{\partial t} + \omega_o^2 u = f(t) \tag{5.3.4}$$

is composed of the coupling "Q" - Q_c and the material "Q" - Q_m where,

$$\frac{1}{Q} = \frac{1}{Q_c} + \frac{1}{Q_m} \tag{5.3.5}$$

For most materials the line diameter can be chosen to make the coupling Q much less than the material Q while maintaining a total Q of 100. In this case the resonant frequency of the composite system will be given by (5.3.6).

$$\omega = \omega_o\sqrt{1 - \frac{1}{4Q_c^2}} \tag{5.3.6}$$

As expected the effect of the line impedance is to reduce the resonance frequency of the system. For the resonant frequency to be within 0.1% of the undamped natural frequency, then a minimum value for the coupling Q can be obtained. Thus, for

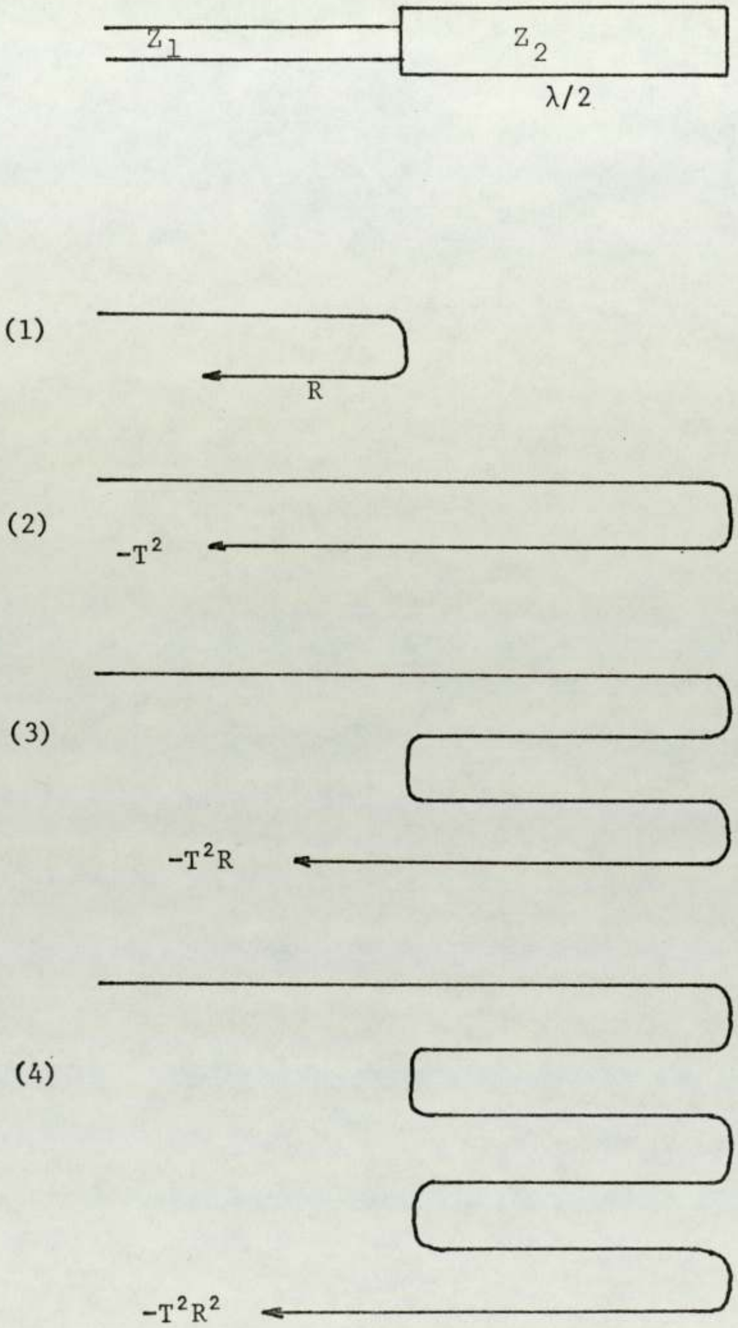

The composite echo build up

FIGURE 5.4

the above condition,

$$Q_c = 11.2$$

It is also known(36) that in the decay of free vibrations Q is the number of cycles for the amplitude to fall to $e^{-\pi}$ of its initial value. So, from these figures it is clear that if during the echo decrement (free vibration) part of the signal, the amplitude has not fallen below 4% (27.3 dB) of its value at the beginning of the decrement, within 13 cycles, then the observed frequency will be within 0.1% of the unloaded resonance. In practice, coupling Qs are normally in the range 20-200 which results in a drop from the undamped natural frequency of between 0.03% and 0.005%.

The shape of the return echo can be understood by considering the reflection of a pulse modulated signal from a distributed resonator, the echo being a composite of the reflected echo and re-radiated signal from the resonator. In Figure 5.4 a half wave length line resonator with no internal energy loss is used as a simple illustration of the build up.

1. Initially the wave reaching the interface is partly reflected and partly transmitted in proportions determined by the usual reflection and transmission coefficients. The displacement of the reflected component is 180° out of phase with the incident vibration (Figure 5.4.1).

2. The displacement wave transmitted through the interface is reflected at the free boundary with no phase change. The total delay through the resonator is always an integer number of wavelengths. Therefore, the re-transmitted wave is out of phase with the initially reflected portion. (Figure 5.4.2).

3. The steps (a) and (b) are now repeated but the wave in the resonator now contains a portion due to the first wave which is reflected from the interface back into the resonator and is in phase with the second wave. (Figure 5.4.3).

4. This process continues and clearly the displacement amplitude of the resonator builds up exponentially. The re-radiated part of the echo waveform also builds up exponentially, but is in antiphase with the reflected part of the transmitted waveform. Thus the composite echo decreases exponentially through a null amplitude to a steady state value.

5. When resonance is fully established and limited by the small but finite losses in the system, the amplitude at the boundary is twice the incident amplitude, i.e., at resonance the interface appears as a free boundary to incident vibrations, the amount of energy transmitted being equivalent to the losses of the resonator.

6. When the incident pulse stops there is an immediate increase in amplitude since there is no longer

a phase cancellation and the echo observed is twice the amplitude of the echo just before the end of the incident pulse. This part of the echo then decays exponentially due to energy lost to the line and internally.

5.4 Optimisation of Echo Signal

A number of factors influence the signal amplitude and signal to noise ratio. Signal amplitude is controlled by the transducer section and signal to noise ratio is controlled by the metallurgical state of the transmission line. Surface imperfection and impedance discontinuities increase reverberation noise and no amount of increase in signal power can improve the signal to noise ratio. For this reason it is necessary to obtain a 'clean' line by careful preparation and handling and also to have good acoustic isolation from any mechanical supports.

The transmission lines as supplied by the manufacturers come in coiled loops. Two materials were used as transmission lines in the experiments described here and they required different treatments. Telcoseal (an iron-nickel alloy) was initially strained in order to straighten the wire and remove kinks. The wire was pulled by hand until further plastic yield was not possible. The end of the wire to be inserted into the coil was then heated to a red heat along about 50 to 100 mm of its length. The effect of straining the wire reduced spurious echoes from the body of the wire and the magnetostrictive coefficient. The latter is restored by heating the end.

Permandur did not exhibit any plastic yield and could not be straightened by cold pulling. In this case the transmission line was heated to a red heat by passing a current of a few amps along its length and allowed to cool under tension. An unexpected phenomenon was observed with 0.5 mm permandur in that noise from the line increased very rapidly at 50-55 kHz. A search of the literature yielded little clarification of this aspect. It was thought that the phenomenon might be due to mode coupling in the body of the transmission line. Meitzler(37) discusses this aspect and attributes mode coupling to the fact that at certain points of the dispersion curves, the various modes have the same phase velocities. This is readily seen by superimposing the dispersion curves in Chapter 2. Modes with the same phase velocities occur at the frequencies where the mode curves cross. However, Meitzler's theory gives a lowest frequency of mode coupling for 0.5 mm permandur at about 45 MHz where the lowest longitudinal (L(0,1)) and the second flexural mode (F(2,1)) intersect. The typical operating frequencies of the transmission lines (below 200 kHz) ensure that the only propagating mode is the lowest longitudinal mode. Lange(38) also observed a phenomenon of mode coupling at long wavelengths. He postulates that surface imperfection much smaller than the wavelength of the propagating mode can act as centres of mode conversion. This seems a likely explanation for the phenomenon described above. It is thought that the process of heat annealing forms an oxide layer on the surface of the transmission line thereby giving centres for mode conversion. Permandur is unsuitable for use at high temperatures since repeated temperature cycling of the wire rapidly degraded the noise performance due to an increase in attenuation and defects created by expansion. This gives added support to the likely cause being surface effects resulting from heat treatment.

The transducer design influences the maximum amplitude of the observed signal. The nominal coil length for maximum signal should be a half wavelength at the operating frequency, although to allow for fringing effects, the coil length is wound 0.42λ with between 200 and 300 turns. In practice a single coil will be used over the full frequency range of the experiments, (between about 50 kHz to 200 kHz) and at the higher frequencies a loss of signal amplitude is tolerated. The transducer end of the transmission line is left as a free boundary for vibration reflection and use is made of this by adjusting the length protruding from the end of the coil to give an increase in signal amplitude. The mechanism of energy conversion in the magnetostrictive material is related to the strain magnitude. At a free end the strain is reflected with a 180° phase shift so the total length of transmission line protruding from the centre of the coil is $\lambda/4$ so that the total phase shift due to the delay and reflection phase shift is 360°. This length is adjusted throughout the experiment to maximise signal amplitude.

The positioning of the bias magnet also has an effect on signal amplitude. Ideally the bias should be at half the magnetic saturation value and its position relative to the coil is adjusted to obtain maximum signal amplitude.

An additional factor affecting signal amplitude is the electrical tuning of the coil. This is carried out with a capacitor connected in parallel with the coil. However, as an aid to mode identification the tuned circuit is made fairly wide band by resistive damping to lower the circuit Q. A low Q circuit can be useful as an aid to mode identification and must always be very much less than the resonator Q.

5.5 Identification of Disc Modes of Vibration

In order to obtain the material constants of a particular disc specimen the modes of vibration have to be identified with absolute certainty. If some prior knowledge of an approximate value of Poisson's ratio for the specimen is known this presents no problem. The spectrum of modes is given in Chapter 4. If an approximate value of the material constants is not known then there are a number of techniques that can be used as an aid to mode identification. It is an experimental fact that radial modes are not as strongly coupled as the contour extensional modes of vibration. This effect is apparent from the number of oscillations before the cross-over point. As an example, Table 5.1 shows the number of oscillations to cross-over (n_x) for modes of vibration of a rolled steel disc.

The parameters of the disc are -

diameter = 35.1 mm
thickness = 3.3 mm
line diameter = 1.2 mm telcoseal

Identification of contour extensional modes are readily made by use of a probe to find the number of circular modes. A quicker technique is to radially clamp the disc at the nodal points. This does not affect the resonance condition and so modes are easily identified.

Frequency kHz	Oscillations to cross-over (nx)	Mode
68.96	52	2,1
80	*	1,1
100.08	150	0,1
105.86	70	3,1
137.67	100	4,1
167.41	120	5,1
173.28	250	1,2
196.12	150	6,1

* No cross-over was obtained for this mode

Frequencies of rolled steel disc (σ=0.28)

Table 5.1

A useful technique available for mode identification is to exite the disc at opposite ends of a diameter. This makes use of the fact that for modes such as 2,1 and 4,1 the opposite ends of a diameter are in phase and for those such as 3,1, they are in anti-phase. The method is to place the driving coil at the centre of the transmission line. This is achieved by having the ends of the transmission line free and move the coil until the echoes from both ends exactly overlap. The anti-phase position is to adjust for maximum cancellation. The disc is then fixed to the transmission line. When the coil is at an even phase position only even modes are detected and odd modes when the coil position is moved by $\lambda/2$.

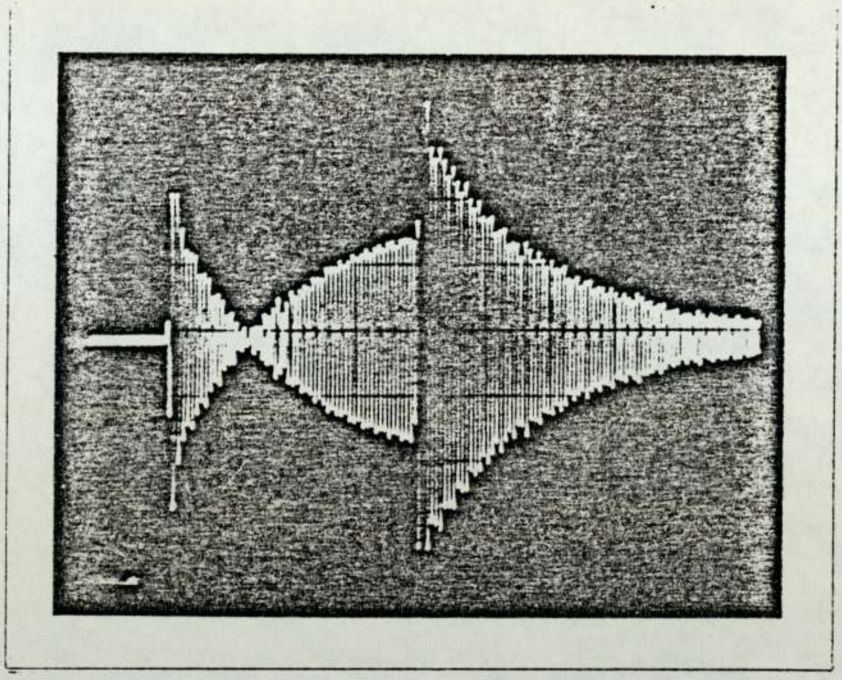

3,1 Mode of aluminium

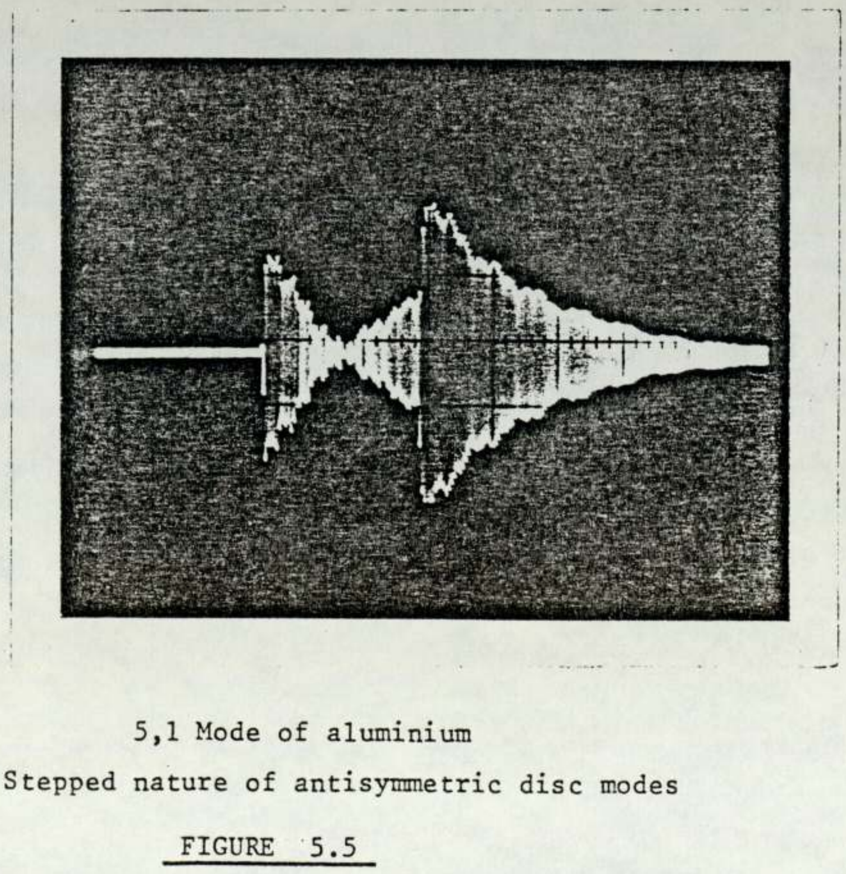

5,1 Mode of aluminium

Stepped nature of antisymmetric disc modes

FIGURE 5.5

Figure 5.5 shows a typical oscilloscope trace of the contour extensional 3,1 and 5,1 modes. The stepped nature of the echo can be made more obvious by lowering the Q of the magnetostrictive transducer to widen the bandwidth. In the case of the 3,1 mode the total phase delay of the transmitted wave is 3λ since six nodes have to be traversed before the first transmitted wave is retransmitted into the line in anti-phase with the reflected signal. Thus three peaks of the reflected part of the signal will have occurred before the transmitted part of the first peak is retransmitted. Similarly in the case of the 5,1 mode, the total phase delay is 5λ since 10 nodes have to be crossed.

Identification of the full mode spectrum of the specimen is determined at room temperature while the disc is accessible. It is normally desirable to use modes close together in frequency for the determination of material constants since retuning of the transducer is not required to optimise signals; also any frequency dependent effects are unlikely to influence the measurements.

5.6 Choice of Modes for Elastic Constant Measurement

In certain materials with Poisson's ratio around 0.33, problems arise in trying to identify the resonant frequencies by the cross-over technique of the 0,1 and 3,1 modes. It is clear from the mode spectra given in Chapter 4 that for this value of Poisson's ratio, the 0,1 and 3,1 modes intersect. The reflected signal from the resonator combines both modes which have almost the same frequency but different coupling. The resultant signal has a modulated appearance which changes rapidly with frequency.

In this case another combination of modes would be used to determine Poisson's ratio such as the 5,1 and 1,2 combination, or 0,2 and 8,1 combination. Particularly confusing was the 0,1; 1,1; 2,1 interaction at Poisson's ratio of -0.1 in the case of pyrolytic graphite. However, it was this phenomenon which occurred at the frequency of lowest detectable mode that gave a clue to a likely value of Poisson's ratio. The only useable combination of modes in this case were the 1,2; 4,1 combination.

Frequency kHz	Mode	K	f/K
24.790	2,1	1.5548	15.944
30.898	0,1	1.9267	16.037
38.099	3,1	2.3751	16.041
49.363	4,1	3.0770	16.043
59.876	5,1	3.7334	16.038
69.876	6,1	4.3686	15.995
78.832	7,1	4.9922	15.791
85.46	0,2	5.3515	15.969
89.75	8,1	5.6323	15.935
99.227	9,1	6.2209	15.951

$d = 38.2$ mm

$\sigma = 0.116$

Av.f/K = 15.974 (Std. dev. = 0.078)

$C_p = 1917\ \mathrm{ms}^{-1}$

Table 5.2

Typical thin disc frequencies of graphite

5.7 Elastic Constants of Graphites

The mode spectrum for the specimen is first established at room temperature. Having identified the modes with confidence, Poisson's ratio can be calculated from the tables in Appendix A4. Using the calculated value of Poisson's ratio the $K_{m,n}$ value is obtained, again from Appendix A4 by interpolation. A useful check on the accuracy and also that the modes are correctly identified is to divide the frequency of the mode by the K value obtained by interpolation. The ratio of f/K should be constant for all modes. The plate velocity C_p is easily obtained from equation (5.6.1).

$$C_p = \pi d(f/K) \qquad (5.6.1)$$

If d is in millimetres and f is in kHz then C_p is in metres/sec. A typical set of room temperature results for graphite are given in Table 5.2.

The graphites measured with the exception of GR5 and pyrolytic graphite were manufactured by an extrusion process. Two samples of each grade of graphite were measured denoted by the letter G or P, meaning with grain or perpendicular to grain respectively. The orientation of the discs is best seen with reference to Figure 5.6.

A summary of the room temperature results of 9 samples of graphite is given in Table 5.3. Graphite type GR5 does not have any grain orientation since it was isostatically

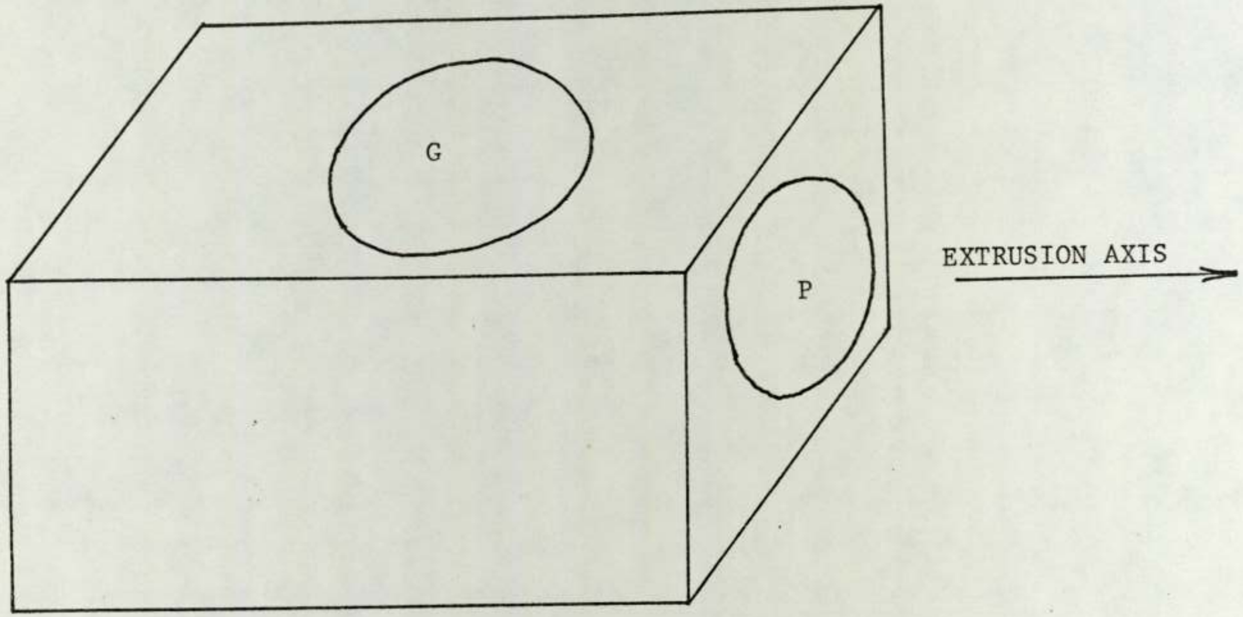

orientation of P and G discs with respect to the extrusion axis

FIGURE 5.6

Graphite Sample	Poisson's Ratio σ	Disc Frequency f (kHz)	Mode	K	f/K
GR1P (d=38.2mm)	0.123	31.402	2,1	1.550	20.26
		39.124	0,1	1.931	20.26
		47.944	3,1	2.367	20.26
		62.010	4,1	3.067	20.22
		75.201	5,1	3.722	20.21
		87.931	6,1	4.356	20.19
GR1G (d=38.2mm)	0.164	27.933	2,1	1.514	18.45
		36.373	0,1	1.960	18.55
		42.949	3,1	2.315	18.55
		55.600	4,1	3.004	18.51
		67.932	5,1	3.648	18.62
		78.944	6,1	4.272	18.48
GR2P (d=38.1mm)	0.055	29.071	2,1	1.608	18.17
		34.208	0,1	1.882	18.17
		44.470	3,1	2.447	18.17
		57.490	4,1	3.163	18.17
		69.388	5,1	3.832	18.11
		81.012	6,1	4.496	18.02
GR2G (d=38.1mm)	0.089	27.134	2,1	1.579	17.18
		33.090	0,1	1.907	17.35
		41.778	3,1	2.408	17.35
		53.850	4,1	3.116	17.35
		65.316	5,1	3.779	17.29
		76.129	6,1	4.420	17.22
GR3P (d=38.1mm)	0.144	26.294	2,1	1.532	17.16
		33.480	0,1	1.948	17.18
		40.266	3,1	2.341	17.20
		52.204	4,1	3.035	17.20
		63.305	5,1	3.677	17.22
		74.055	6,1	4.314	17.17
GR3G (d=38.3mm)	0.159	31.005	2,1	1.519	20.42
		39.950	0,1	1.957	20.42
		47.399	3,1	2.322	20.15
		61.565	4,1	3.024	20.36
		75.068	5,1	3.658	20.52
		86.616	6,1	4.283	20.22
GR4P (d=38.1mm)	0.112	24.797	2,1	1.560	15.90
		30.540	0,1	1.924	15.88
		37.795	3,1	2.381	15.88
		49.041	4,1	3.083	15.90
		59.140	5,1	3.741	15.81
		69.201	6,1	4.377	15.81
GR4G (d=38.2mm)	0.137	30.633	2,1	1.538	19.92
		38.45	0,1	1.941	19.81
		46.533	3,1	2.350	19.81
		60.475	4,1	3.046	19.85
		73.579	5,1	3.697	19.90
		85.026	6,1	4.328	19.66
GR5 (d=38.1mm)	0.188	29.793	2,1	1.493	19.96
		39.327	0,1	1.976	19.90
		45.457	3,1	2,285	19.90
		59.047	4,1	2.966	19.91
		71.820	5,1	3.605	19.70
		83.824	6,1	4.222	19.85

Table 5.3

Thin Disc frequencies for 'P' and 'G' orientated graphites pressed and not extruded. In all cases the measured Poisson's ratio of 'P' cut samples was lower than that of 'G' cut samples. The measured plate velocity did not show the same consistency.

In some samples the plate velocity was higher in 'P' cut materials and lower in others. The plate velocities are summarised in Table 5.4.

Graphite Sample	Plate Velocity ms^{-1}
GR1P	2428.2
GR1G	2223.4
GR2P	2170.7
GR2G	2068.1
GR3P	2057.4
GR3G	2442.0
GR4P	1898.8
GR4G	2379.2
GR5	2377.6

Table 5.4

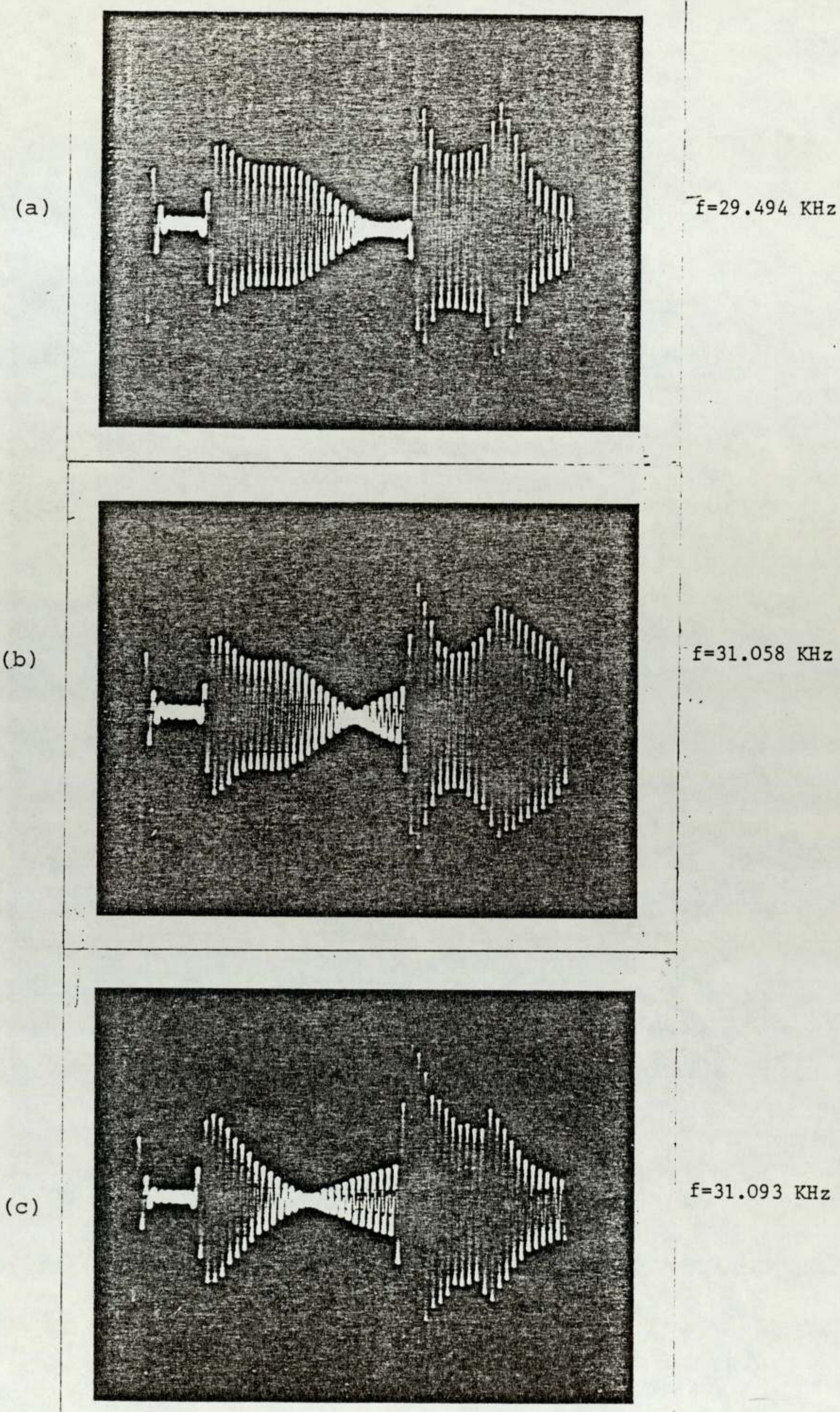

Effect of anisotropy on the echo

FIGURE 5.7

5.8 Effects of Anisotropy

Initially considerable difficulty was experienced in identifying the modes of vibration of graphite GR4G. The modes above 4,1 were readily identified from the number of oscillations in the echo steps but below the 4,1 mode there were more resonances than could be accounted for by the disc spectrum. This anomaly was not apparent in the graphite GR4P. At the lowest detectable modes , resonance occurred initially at 29.494 kHz and 31.058 kHz. These two resonances showed a modulation of the echo envelope typical of two disc resonances. The oscilloscope traces are shown in Figures 5.7a and 5.7b.

Further investigation revealed that this behaviour depended on the position of the line drive around the periphery of the disc. A position was found on the disc where the lowest mode showed no modulation, due to a second close resonance and the oscilloscope trace is shown in Figure 5.7c. The most likely reason for this effect is a small amount of macroscopic anisotropy in the manufacturing process of this particular graphite. The problem of mode identification was eventually resolved by use of the two position excitation technique described above to resolve odd and even modes using an 0.3mm permandur line at two positions at 90° apart. The results of this experiment are given in Table 5.5 for each position. Use is made of the fact that f/K is constant to identify the modes. In the 90° position the two even modes at 84.985 kHz and 86.230 kHz give f/K values of 19.6 and 19.95

0° Position σ=0.1353				90° Position σ=0.1385			
fkHz	odd o even e	Mode	f/K	fkHz	odd o even e	Mode	f/K
30.707	e	2,1	19.946	29.413	e	2,1	19.139
38.674	e	0,1	19.932	38.708	e	0,1	19.928
46.857	o	3,1	19.926	46.769	o	3,1	19.921
60.704	e	4,1	19.914	60.727	e	4,1	19.951
73.843	o	5,1	19.956	73.756	o	5,1	19.962
85.208	e	6,1	19.674	84.985 86.230	e e	6,1? 6,1?	19.650 19.938
97.957	o	7,1	19.788	97.810	o	7,1	19.785
110.026	e	8,1	19.780	109.836	e	8,1	19.772

Table 5.5

Effect of driving line position on observed frequencies of GR4 graphite.

respectively. The average value of f/K is about 19.9 implying that 86.230 kHz is the 6,1 mode resonance. The effect of the anisotropy is to increase the scatter in the f/K value and is particularly noticeable in the 2,1 mode in the 90° position. However, the effect on Poisson's Ratio is fairly small but does of course increase the uncertainty of the measurement.

Frequency kHz	K	Mode	f/K
52.778	1.7239	2,1	30.615
53.306	1.7530	1,1	30.408
54.068	1.7661	0,1	30.614
79.349	2.6030	3,1	30.483
101.408	3.3373	4,1	30.386
107.649	3.5424	1,2	30.388
122.257	4.0233	5,1	30.388
142.257	4.6890	6,1	30.300
160.741	5.3122	0,2	30.260
161.830	5.3444	7,1	30.280
179.819	5.9938	8,1	30.000

(4,1), (1,2) comparison $\sigma = -0.099$

(0,2), (7,1) comparison $\sigma = -0.102$

(0,1), (2,1) comparison $\sigma = -0.094$

$C_p = 3484 \text{ ms}^{-1}$

Table 5.6

Thin disc frequencies of pyrolytic graphite

5.9 Pyrolytic Graphite

Pyrolytic graphite is manufactured by a chemical vapour deposition (C.V.D.) process onto a former made of some refractory material at high temperatures, (about 2000°C). The pyrolytic graphite is very highly anisotropic with the basal planes parallel to the former and the planes stacked one on top of another. The disc used in the measurements performed was cut from a flat sheet of pyrolytic graphite deposited on a tungsten former. A discussion of the manufacture of pyrolytic graphite and a review of its properties is given in reference 39 .

The anisotropy of pyrolytic graphite does not have any influence on the present technique of measurement. The use of in-plane disc modes measures the in-plane value of Poisson's ratio. The disc of pyrolytic graphite of course appears isotropic in-plane. The measurement of modes of vibration do not in this case depend on the position at which the transmission line is coupled to the disc. The Poisson's ratio was measured by comparing the 1,2; 4,1 modes and as a check on accuracy, with the 2,1; 0,1 and 0,2; 7,1 modes. The room temperature frequency of vibrations are given in Table 5.6 . The ratios $(K_{2,1}-K_{0,1})/K_{0,1}$ and $(K_{0,2}-K_{7,1})/K_{1,7}$ are not included in Appendix A4.1 since they are not generally of sufficient sensitivity over the more conventional range of Poisson's ratio. However, a supplementary table over the range of Poisson's ratio -0.07 to -0.12 is given in Table 5.7 .

The average value of Poisson's ratio obtained from the frequencies of Table 5.6 is -0.098. A negative value of Poisson's ratio for the basal plane Poisson's ratio of -0.15 is also given in reference 39 . A negative value of Poisson's ratio implies an increase in lateral dimensions with tension. Smith and Leeds state that this is a consequence of the very large compression perpendicular to the basal planes. The c axis strain resulting from in-plane stress given in reference 42 corresponds to a σ value of 0.90. This of course exceeds the normal range of Poisson's ratio for isotropic materials.

Poisson's Ratio	$\frac{K_{2,1}-K_{4,1}}{K_{4,1}}$	$\frac{K_{2,1}-K_{0,1}}{K_{0,1}}$	$\frac{K_{0,2}-K_{7,1}}{K_{7,1}}$
-0.07	0.06982	-0.04463	0.00130
-0.08	0.06681	-0.03560	-0.00135
-0.09	0.06393	-0.02800	-0.00390
-0.10	0.06119	-0.01851	-0.00627
-0.11	0.05859	-0.00963	-0.00855
-0.12	0.05613	-0.00067	-0.01070

Table 5.7

It was not possible in this case to obtain a second Poisson's ratio using the disc technique. Samples of pyrolytic graphite sufficiently thick to cut discs perpendicular to the basal planes were not available. The value of plate velocity for pyrolytic graphite was considerably in excess of the values of conventional graphites given in Table 5.4. For the pyrolytic graphite sample investigated the plate velocity C_p was 3484 ms^{-1}.

5.10 Variation of Graphite Elastic Constants with Temperature

Graphites, because of their low density and refractory properties,are an important material in such applications as the throats of rocket engines. For this reason the temperature coefficients of elastic constants are of importance to designers. The transmission line technique is particularly applicable to the measurement of temperature coefficients. The transmission line can be chosen for its refractory properties and a section of magnetostrictive material can be brazed or butt-welded to the transducer end. By matching the characteristic impedances of the two materials spurious reflections can be avoided. This is often achieved from stock sizes of materials by etching with acid until the required dimensions are obtained.

The interface between the transmission line and the resonator in the hot zone is required to maintain good acoustic integrity over the temperature range being used. In the case of the graphite discs a small hole about 1-2 mm deep and slightly larger than the transmission line was made and the two joined with an alumina based cement "Autostic". This cement is suitable for use up to 1600°C.

The furnace used in the temperature experiments was a quartz tube capable of accepting discs up to about 40 mm with a temperature range of about 1000°C. The atmosphere around the disc is maintained inert by a small overpressure of nitrogen or argon.

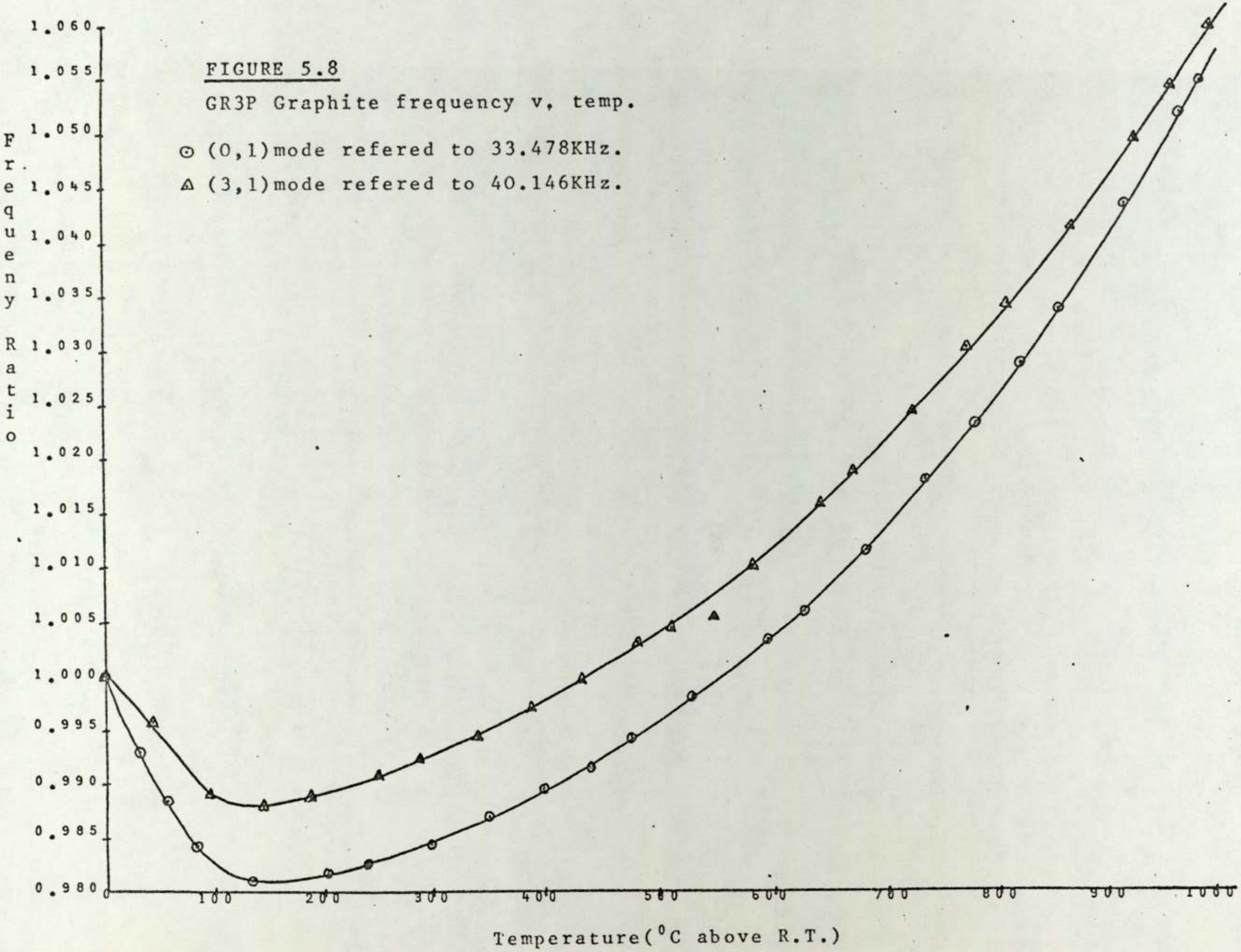

FIGURE 5.8

GR3P Graphite frequency v, temp.

⊙ (0,1)mode refered to 33.478KHz.

△ (3,1)mode refered to 40.146KHz.

In all cases except pyrolytic graphite the 0,1 and 3,1 resonances are measured over the full temperature range. In the case of pyrolytic graphite the 1,2 and 4,1 resonances are measured. Readings of the two modes were taken alternately at intervals of two minutes together with the temperature from a chromel alumel thermocouple. The thermocouple junction was placed in close proximity to the centre of the disc. The readings of temperature (mV from chromel alumel thermocouple) and frequency were recorded automatically via a Solatron data transfer unit on a teleprinter. A typical temperature run to 1000°C took about five hours to complete. The frequency variation over the temperature range is given in Figures 5.8, for a typical sample GR3P. Although the frequencies of the two modes are measured alternately, the increase in temperature can be assumed to be linear over a time of about ten minutes, and the frequencies are interpolated to give their values at the same temperature to calculate Poisson's ratio. The results of this calculation are shown in Figures 5.9. No information of the variation of density with temperature is available, so Figures 5.10 show Young's modulus/density for the temperature 0-1000°C although room temperature densities for these samples is typically $1.8.10^3$Kgm^{-3}, and it is not expected that this will change very much over the temperature range.

Figures 5.9 show the variation of Poisson's ratio for all graphites including pyrolytic graphtie to be very small up to a temperature of 1000°C. The Young's modulus curves (Figures 5.10) of conventional graphites show an initial decrease in

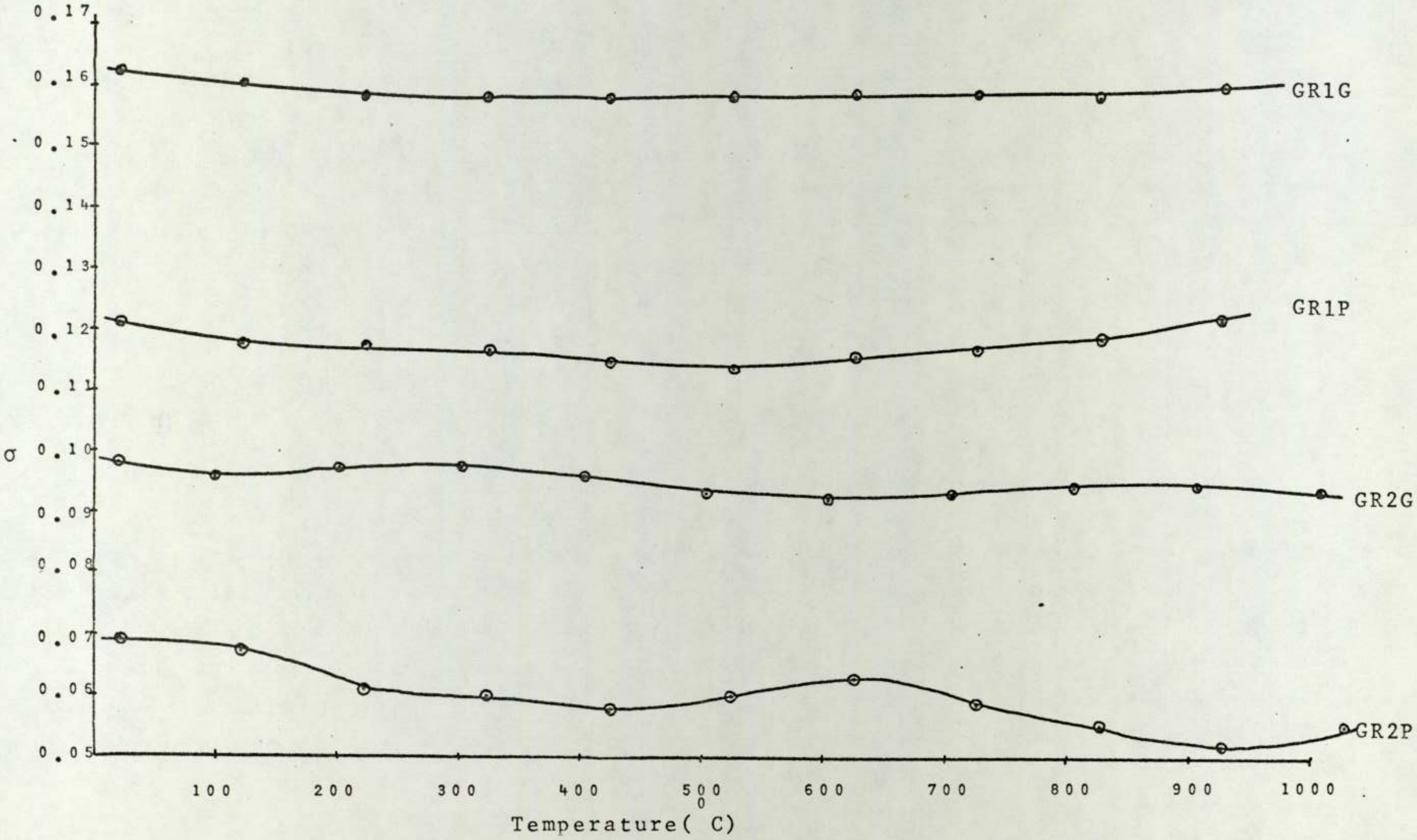

Poisson's Ratio of graphite v. temperature

<u>FIGURE 5.9.1</u>

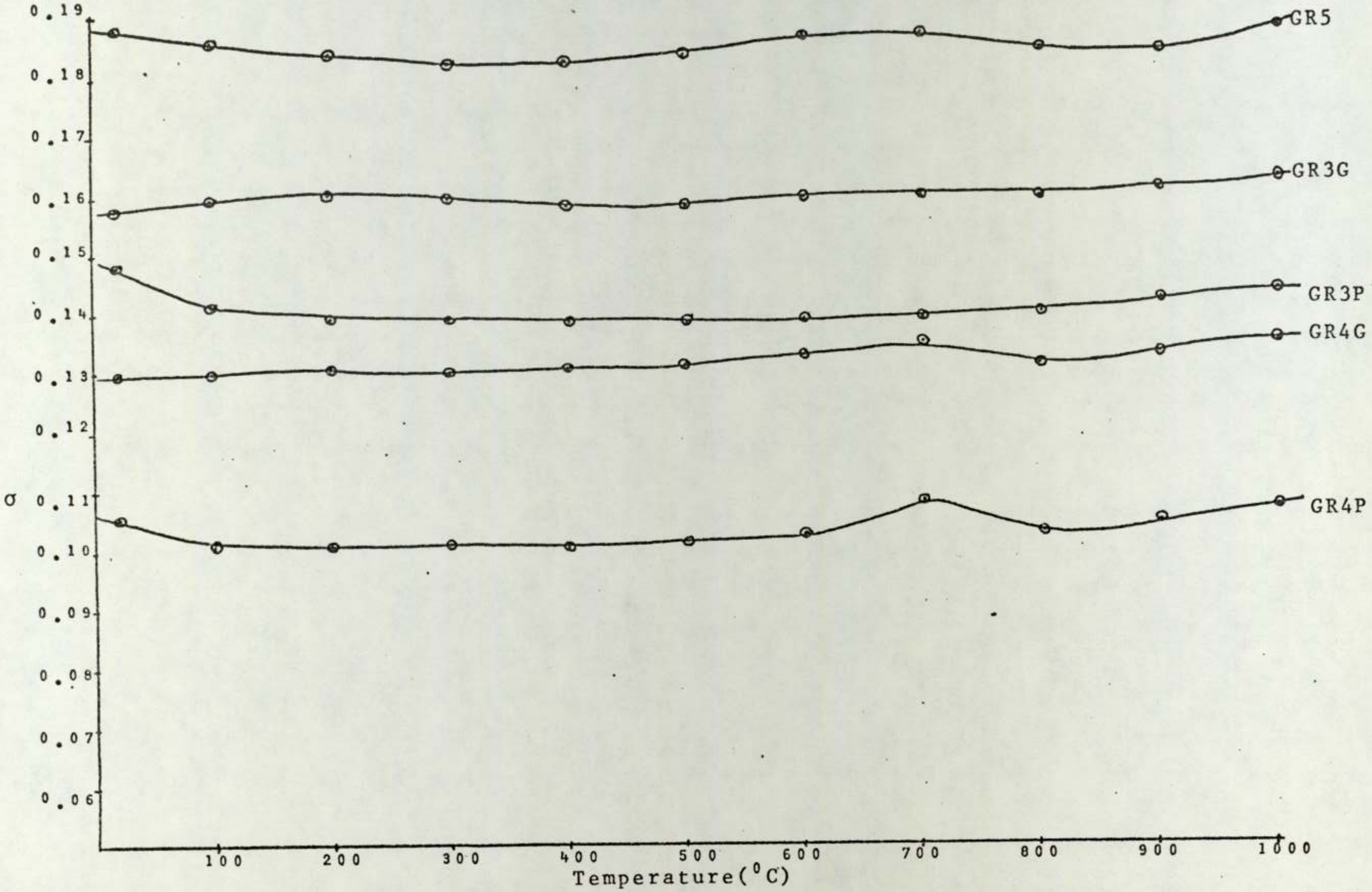

Poisson's Ratio of graphite v. temperature

<u>FIGURE 5.9.2</u>

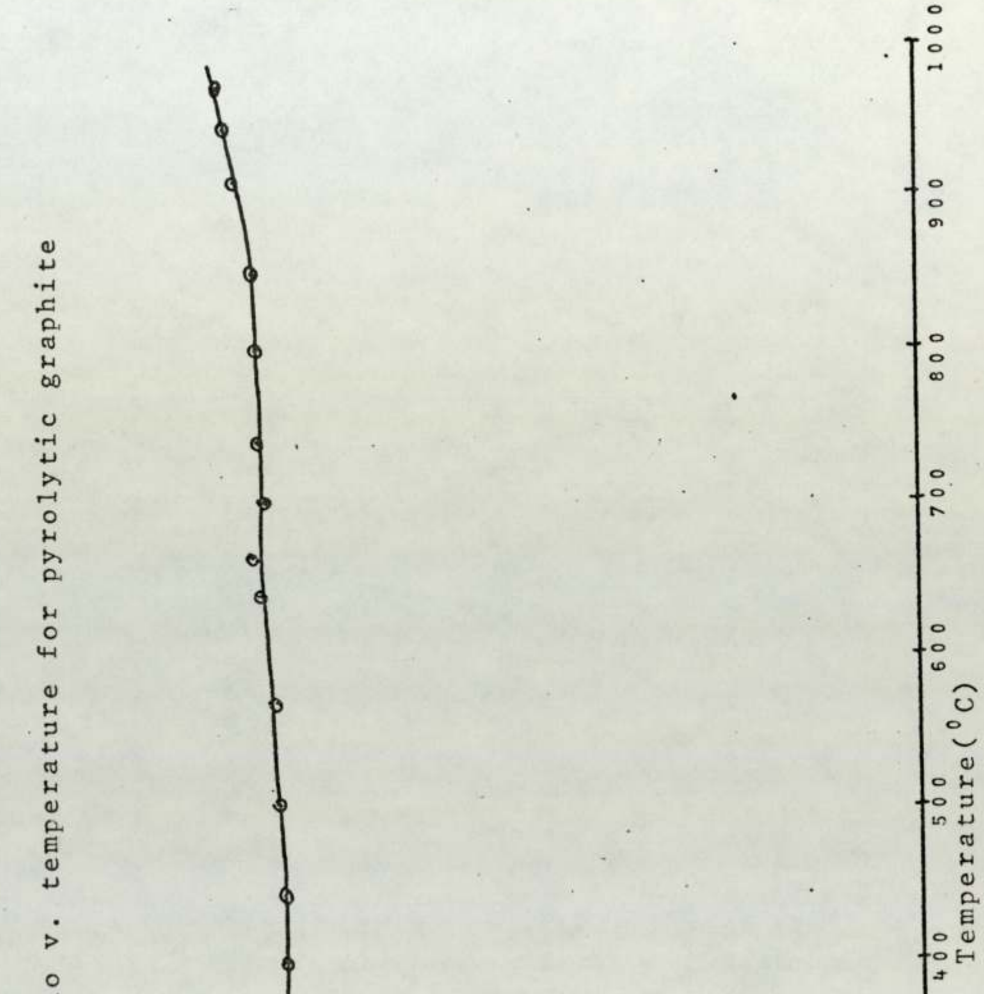

Poisson's Ratio v. temperature for pyrolytic graphite

FIGURE 5.9.3

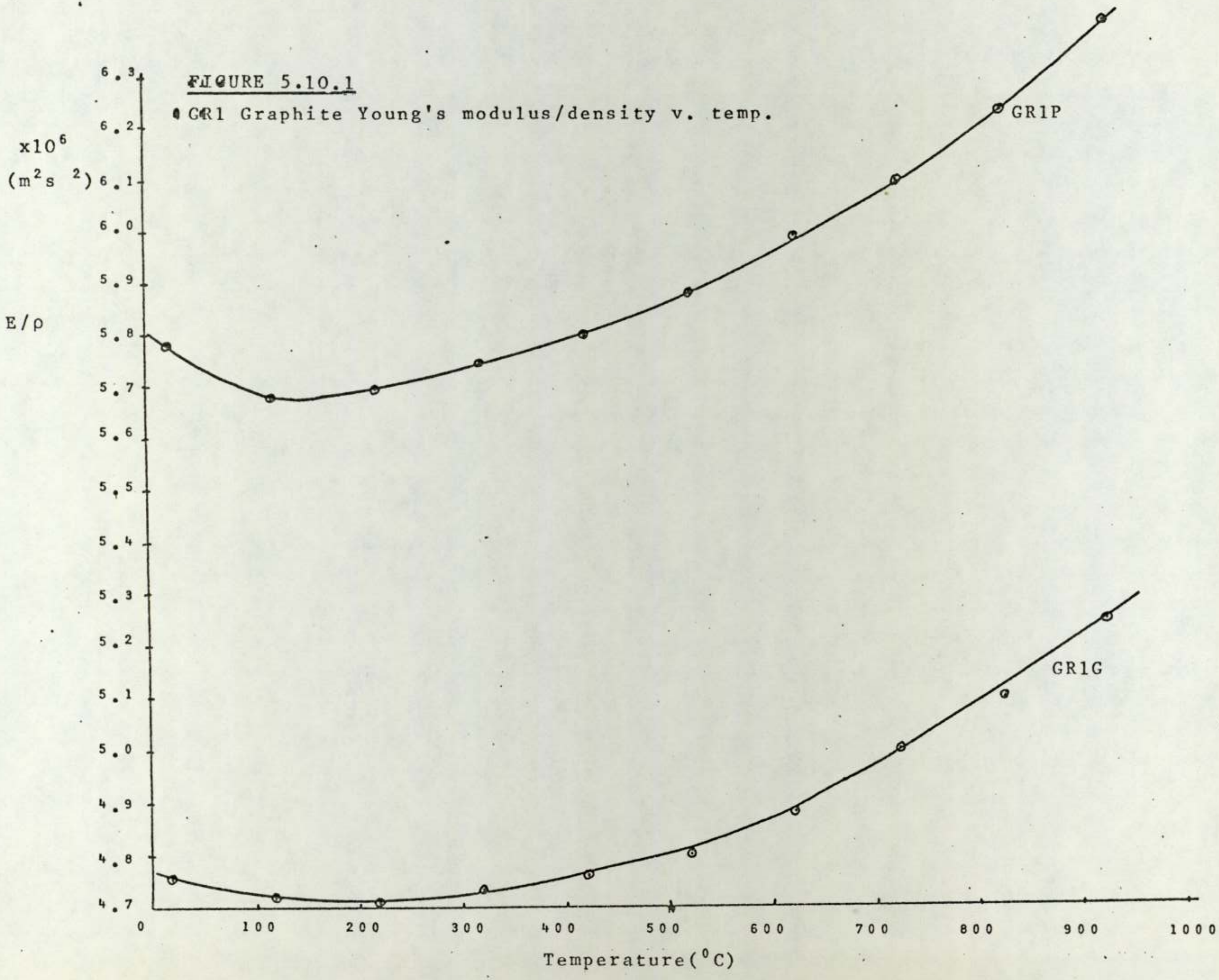

FIGURE 5.10.1

GR1 Graphite Young's modulus/density v. temp.

FIGURE 5.10.2

GR2 Graphite Young's modulus/density v. temp.

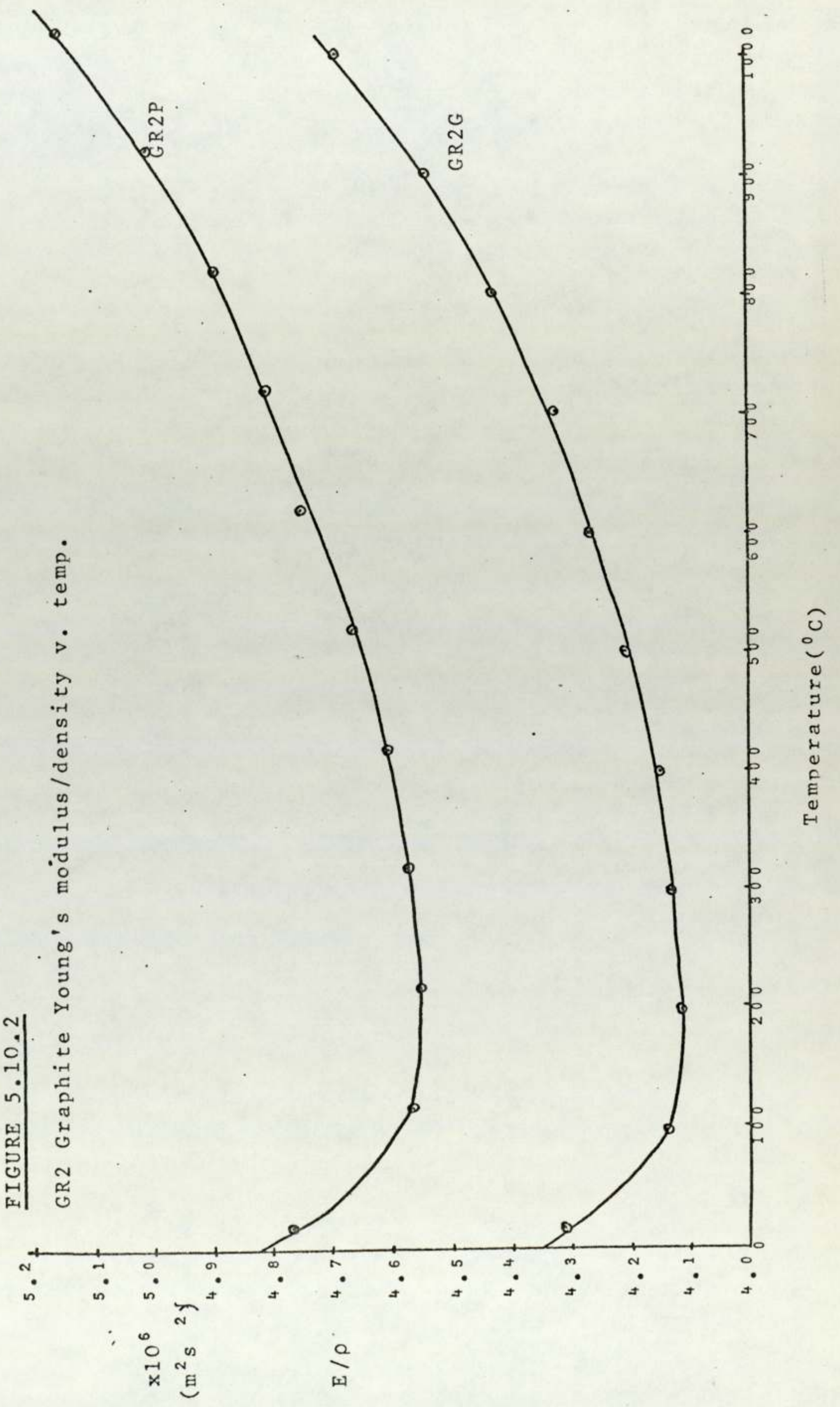

FIGURE 5.10.3

GR3 Graphite Young's modulus v. temp.

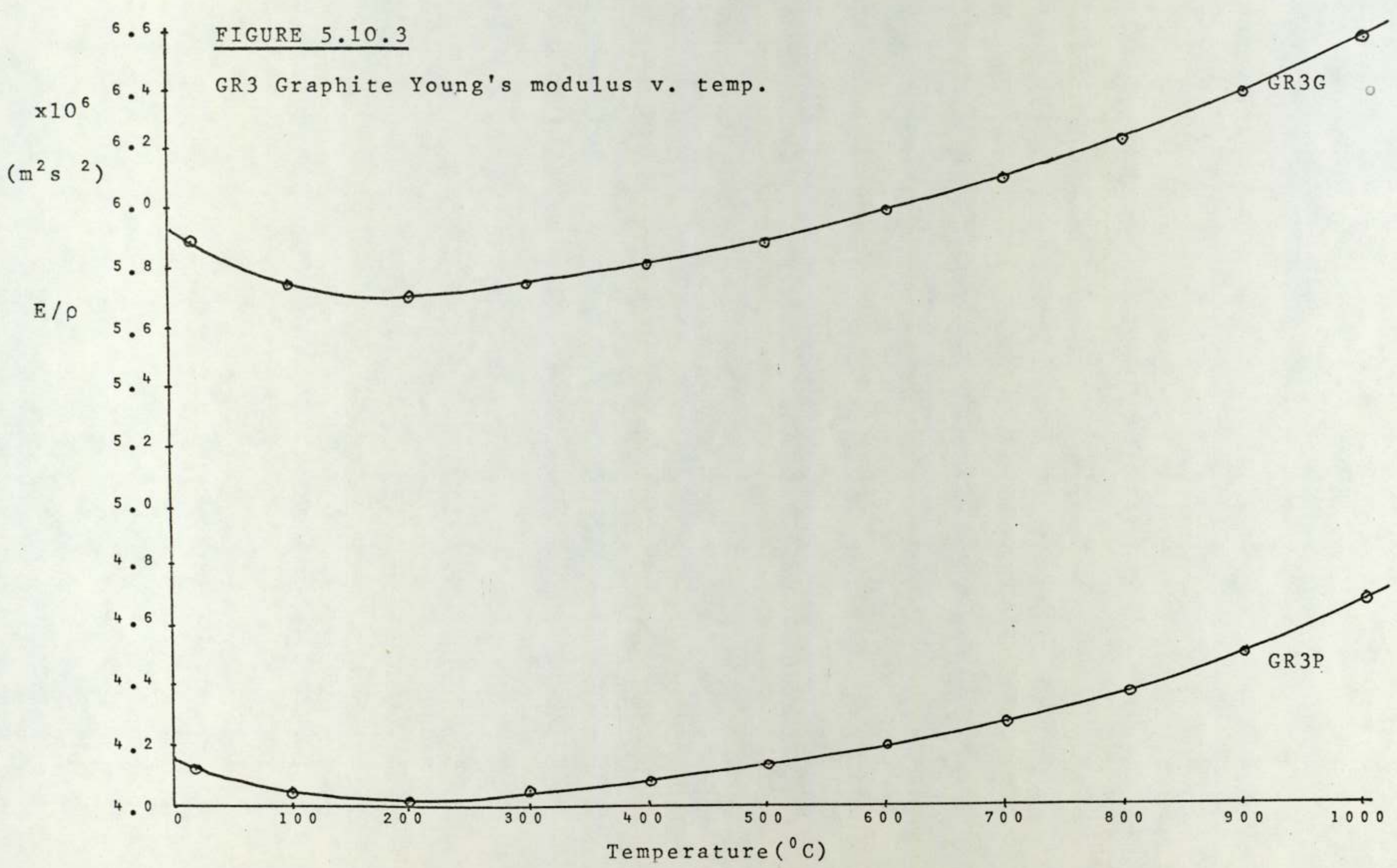

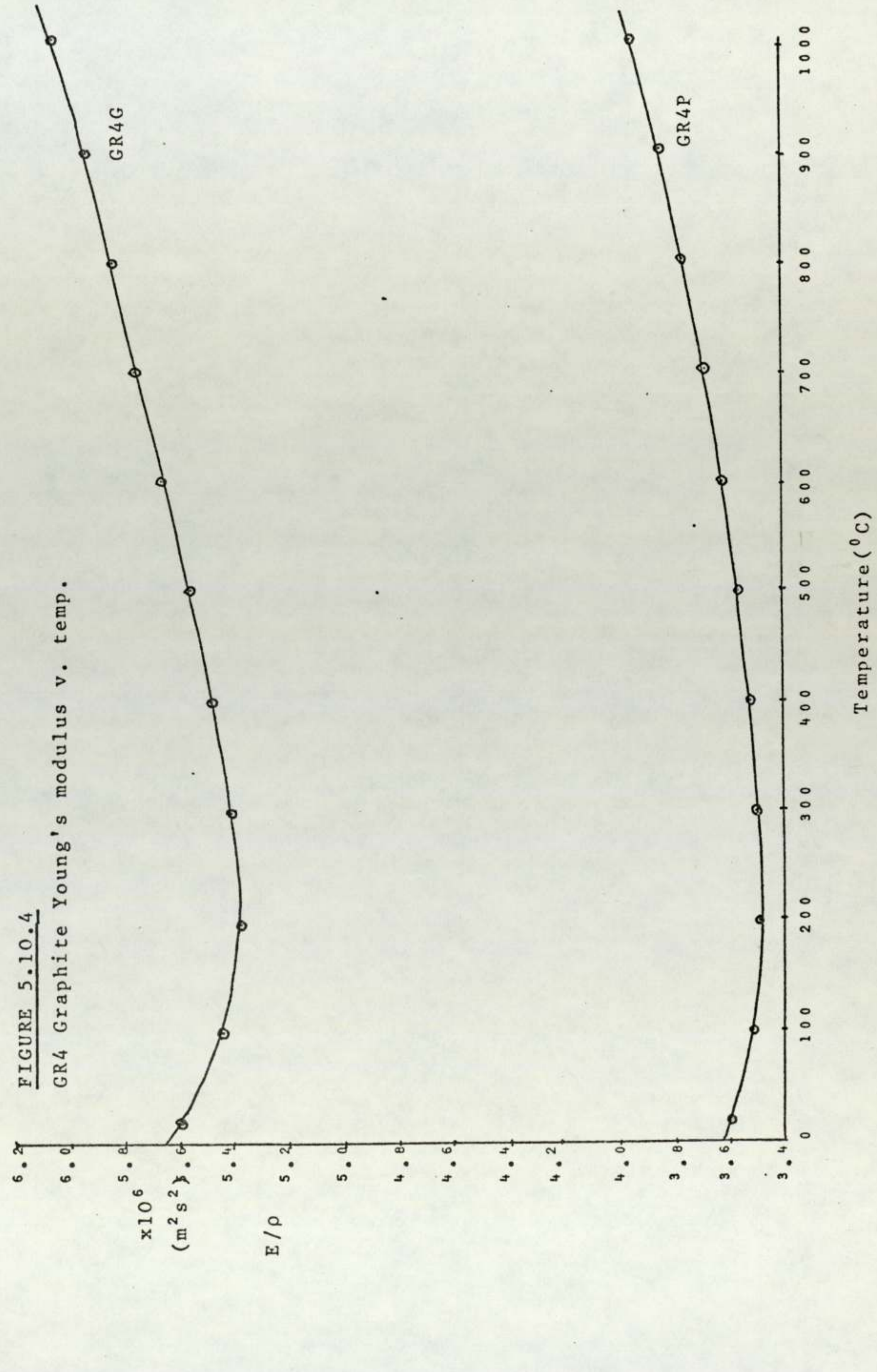

FIGURE 5.10.4

GR4 Graphite Young's modulus v. temp.

FIGURE 5.10.5

GR5 Graphite Young's modulus v. temp.

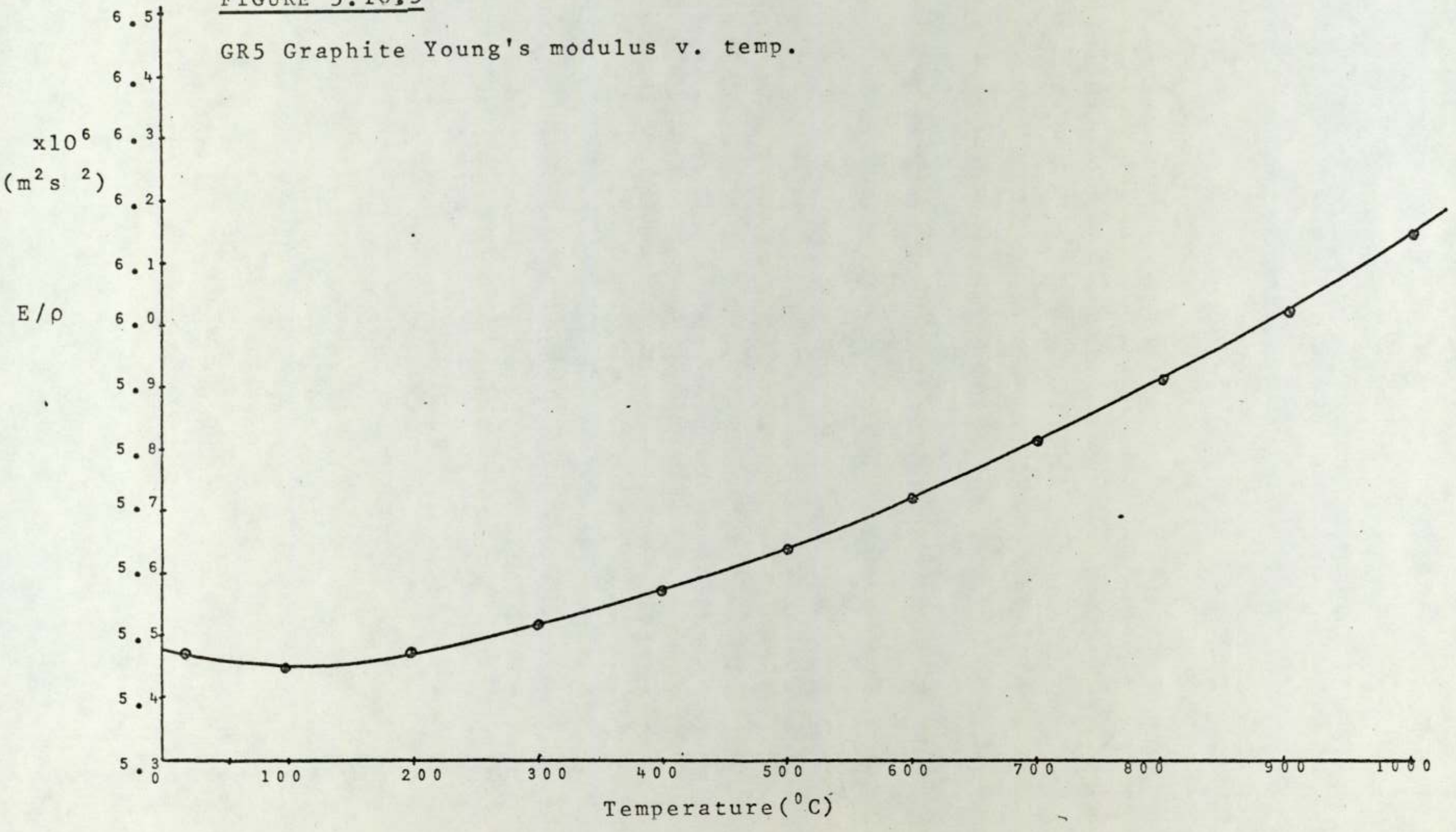

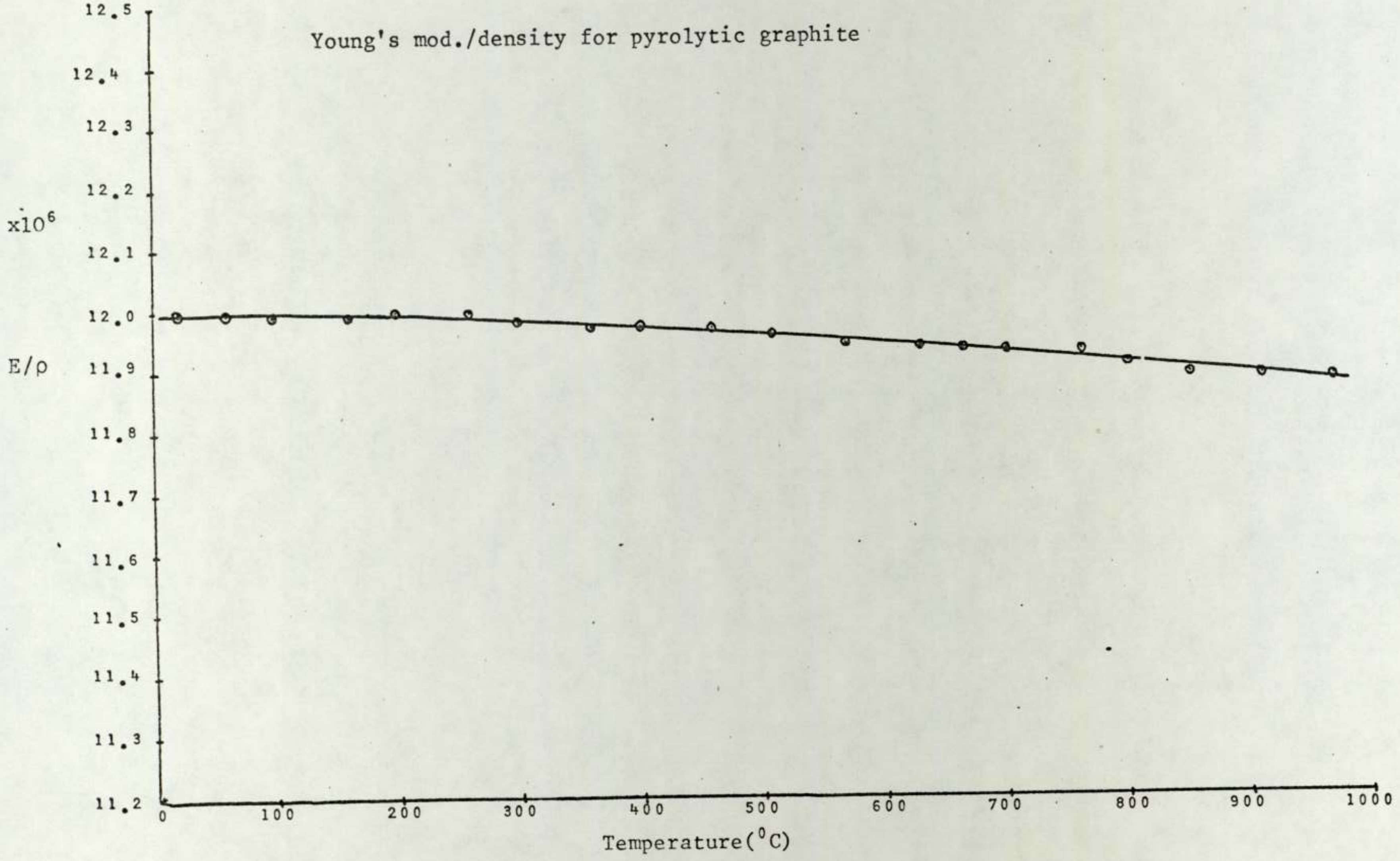

Young's mod./density for pyrolytic graphite

FIGURE 5.10.6

Poisson's ratio to definite minima. Depending on the graphite type this minima occurs at about 100°C - 200°C. This behaviour has been noted by Mason and Knibbs(40). They account for this behaviour by postulating that the crystallites expand initially to fill the voids in the polycrystalline graphite. During this time the Young's modulus decreases. Once the voids are filled, the stiffness of the material tends to increase. It would be expected that at some higher temperature (higher than 1000°C) Young's modulus must then fall again. Figure 5.10.6 shows Young's modulus variation with temperature for pyrolitic graphite. The modulus for pyrolitic graphite is between two and four times the room temperature values for the other conventional graphites. The density of pyrolytic graphite is slightly higher than conventional graphites, 2.1×10^3 Kgm^{-3} compared to about 1.5×10^3 Kgm^{-3}. The temperature coefficient for the pyrolytic graphite is again small, up to a temperature of 1000°C. It should also be noted that in this case there is no minimum in the Young's modulus for pyrolytic graphite and shows a steady fall with temperature.

The conspicuous elasticity differences between commercial and pyrolytic graphites can now be considered. Commercial graphite consists of grains of pyrolytic graphite of various sizes and are random in their orientation. The grains in turn usually consist of single crystals possibly, but not necessarily, randomly oriented. It must be emphasised that the measurements on the pyrolytic graphite are in the plane of the hexagonally structured atoms, strongly held together by covalent bonds. In the orthogonal direction the sheets of atoms are well separated and weakly bound together by a metallic like linkage of free electrons. The elasticity in this direction will be very low and the anomalous increase in elasticity with temperature of all commercial graphites must arise in some way from this anisotropy.

The results on pyrolytic graphite are typical of a single covalent crystal. The elasticity is high and falls only slightly with temperature for the comparatively limited range measured. In the transverse direction the metallic bond would be expected to produce a large negative elasticity coefficient and a high Poisson's ratio for this orientation.

Recent results on mica, which has a structure similar to graphite in which hexagonal atomic planes are widely separated, the inter-plane binding in this case however being covalent, show similar small changes in in-plane properties.

The room temperature properties of commercial graphite are consistent with these features, at least qualitatively. The randomness of orientation means that there is an averaging between the high and low elasticities of the crystals and of the Poisson's ratios. The wide scatter of results can be attributed to the variations in orientation due to the initial forms of carbon or carbon compounds used in their manufacture and variations in heat treatment. The production of graphite requires holding the material at a temperature of the order of 2500°C for a number of days. The very large furnaces used take a long time to cool down but no process analogous to annealing of metals can be expected. The large anisotropy of graphite will result in the crystals within the grains,and to some extent the grains themselves,being under stress. The contraction during cooling could result in the presence of voids in the grains and their intensities.

The paradox that the elasticity of commercial graphite having fallen to a minimum at one or two hundred degrees and increases over the full range of temperatures measured must be attributed to the effect of changes in voids and stress. The features are common to graphites formed from a variety of source materials including graphite fabric, graphite composites, and 'densitised' graphite which is multiple graphitised material where a hydrocarbon liquid has been soaked into the material between each stage. Recent measurements on a very fine grained "Poco" graphite,produced as a reference material by the National Bureaux of Standards, reveal the same phenomenon. At the present state of knowledge this paradox must remain unresolved. If the crystals are under stress at low temperatures the elasticity is expected to be high and this will fall as the stress is relieved. The reverse appears to occur. Knowledge of the effect of temperature and stress on pyrolytic graphite in the transverse direction would be a major contribution to the resolution of this paradox. As far as is known only silica, the elasticity of which increases to 1400°C, shows the same effect. The structural differences, silica being devoid of even microcrystalline structure, makes it unlikely that they have common sources.

CHAPTER 6

TIME OF FLIGHT MEASUREMENT OF ELASTIC CONSTANTS

CHAPTER 6

TIME OF FLIGHT MEASUREMENT OF ELASTIC CONSTANTS

6.1 Introduction

Time of flight methods of measuring elastic constants offer an alternative to resonance techniques and find applications in areas of measurement where resonance methods have limitations. For example, in the resonance method a material Q factor of 20 requires a coupling of the same order giving a net Q of 10. The transducer is selective to an extent amounting to a 'Q' of about 3. An observation will thus be biased significantly by the transducer tuning. In the time of flight method the corresponding signal attenuation for a distance of 10λ will be of the order of 14 dB. This gives a good signal to noise ratio and there is no deterioration in measurement accuracy. As has already been covered in previous chapters the loss in polycrystalline metals makes resonance methods ineffective at about 2/3 of the melting point. Single crystals and certain non-metals such a silicon nitride and graphite have low loss to their temperature limits. A variety of methods of measurements using piezo-electric and magnetostrictive sources have been described in the literature(41,42,31). This present work deals only with pulses derived from magnetostrictive transducers and is specifically designed to operate with thin transmission lines.

Bell (ICA 1959) proposed a notched line technique for monitoring temperature in the centre of nuclear fuel rods. Single pulse methods of measuring temperature are fairly well established although the difficulties imposed by working in a nuclear environment still present considerable problems(43).

Instruments have been designed to measure time of flight(44) with a tuning accuracy of about ±100 ms relying on estimating the 3 dB points of the return echo pulses. In ultrasonic thermometry applications, Fathimani(34) described a probe design and associated instrumentation for tracking temperature changes of frequency of resonant tuning forks.

This present chapter gives a technique based on the transmission of two pulses that enable small changes in the elastic modulus of a material to be detected. Although the method has general applications it is particularly suited, after probe calibration, to ultrasonic temperature measuring applications. The material chosen to demonstrate the method was a sample of 2% thoriated tungsten, a material often used as probes in nuclear fuel rods.

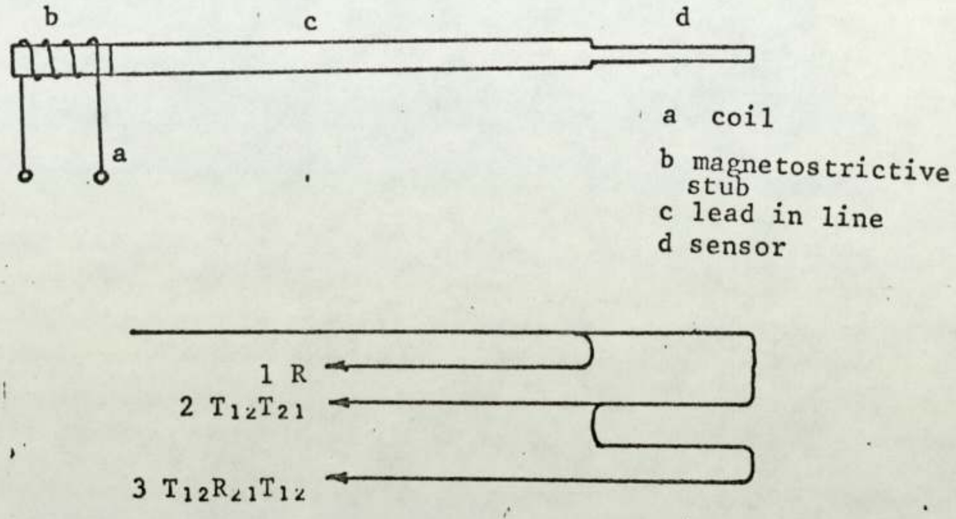

Probe arrangement
FIGURE 6.1.a

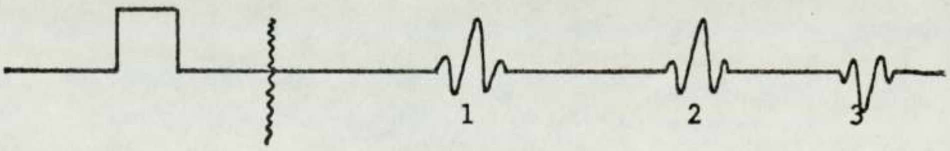

Return echoes
FIGURE 6.1.b

6.2 Pulse Overlap Velocity Measurement

The reflection and transmission coefficients for displacement at an impedance discontinuity are given by equations (6.2.1) and (6.2.2) respectively.

$$R = \frac{Z_1-Z_2}{Z_1+Z_2} \qquad (6.2.1)$$

$$T = \frac{2Z_1}{Z_2+Z_1} \qquad (6.2.2)$$

The impedance mismatch is arranged in this case for Z_2 to be less than Z_1. The physical arrangement is shown in Figure 6.1(a),and Figure 6.1(b) shows the polarity of the reflected echoes. The time between the echoes 1 and 2 is the flight time in the sensor length d. If the velocity in the sensor material is c then the flight time t is given by equation (6.2.3).

$$t = \frac{2d}{c} \qquad (6.2.3)$$

The peak of the pulse is not necessarily the centroid of the energy and Papadakis(44) uses the 3 dB points to find the centroid. All methods will be subject to some error if the spectral content and hence the shape of the pulse changes, say, due to a reactive impedance at a junction.

The pulse overlap method consists of transmitting pairs of pulses. The time between launching these two pulses is adjusted so that the reflection from the impedance mismatch

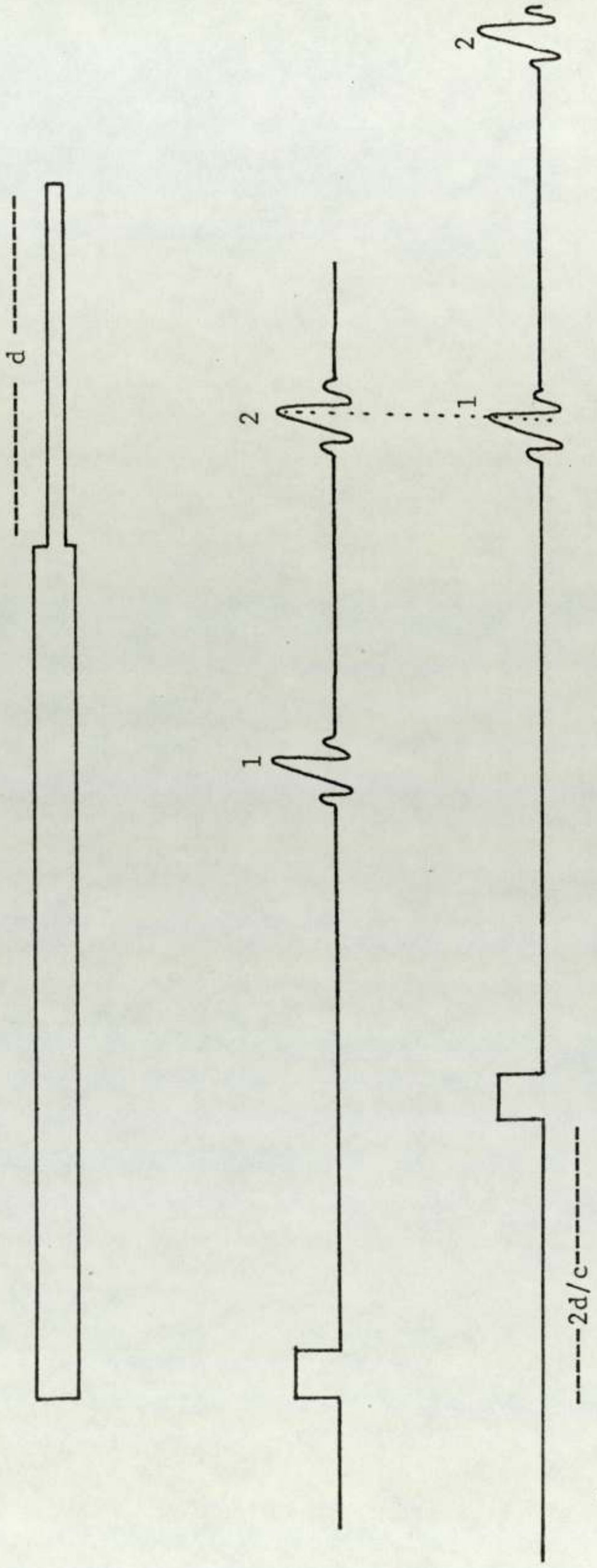

1--- Echo from junction

2--- Echo from free end

FIGURE 6.2

Schematic representation of double pulse overlap.

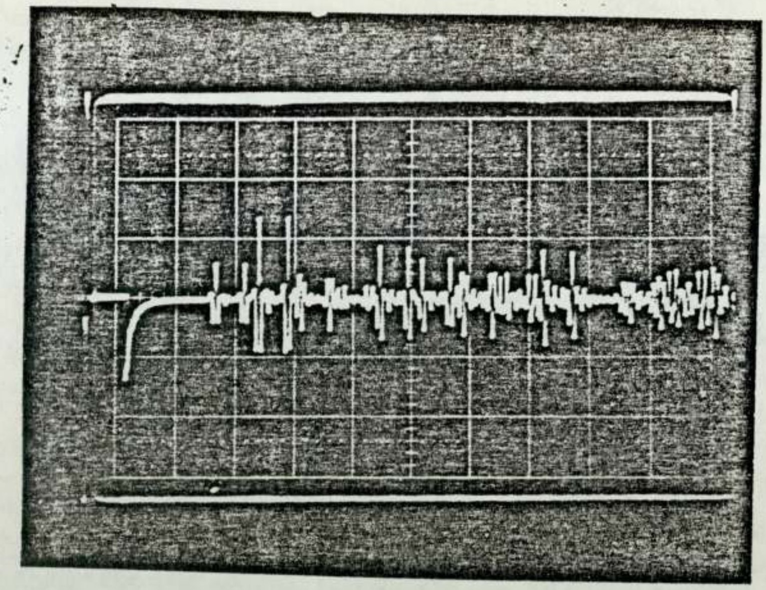

The first pair of echoes are from the junction and the second pair are the end echoes.

Period= 48.55μs (less than the 2 way flight time).

FIGURE 6.3.a.

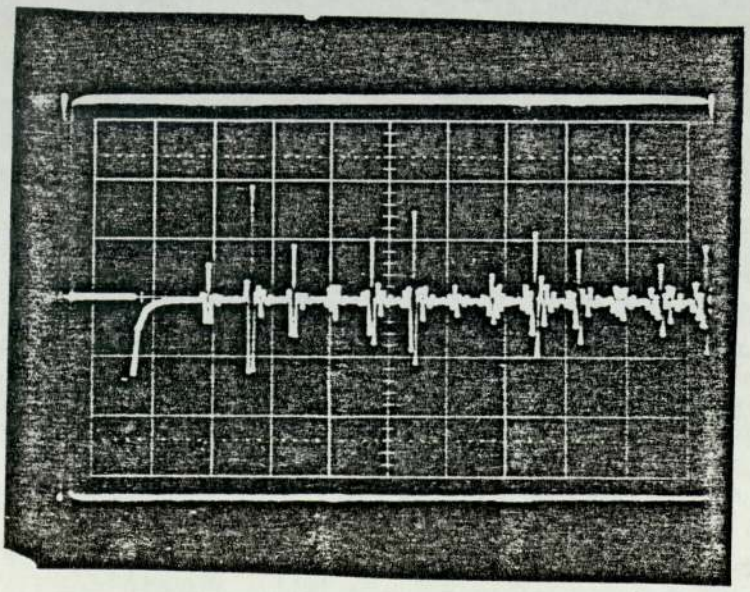

The first echo is the junction echo, the second junction echo and first end echo are overlapped.

Period = 79.892μs (equal to 2 way flight time).

FIGURE 6.3.b.

of the second transmitted pulse is made to coincide exactly with the pulse reflected from the free end of the sensor due to the first transmitted pulse. This is illustrated in Figure 6.2 where the echo timing relationships are shown schematically. If the two transmitted pulses are gated from an oscillator, then at overlap the period of the oscillator is the flight time in the sensor d. Figure 6.3(a) shows the typical echoes produced from a transmission of two pulses whose separation is less than the flight time in the sensor. Figure 6.3(b) shows the overlap condition where the period of the oscillator is adjusted until the amplitude of the combined pulse is at a maximum.

6.3 The Composite Echo

Equations (6.2.1) and (6.2.2) give the reflection and transmission coefficients. Putting $z = Z_2/Z_1$ the reflected signal from the junction is:

$$R = \frac{1 - z}{1 + z} \qquad (6.3.1)$$

and the transmitted signal is:

$$T_{12} = \frac{2}{(1+z)} \qquad (6.3.2)$$

The signal transmitted back from the sensor section d into the transmission line c of Figure 6.1 is:

$$T_{21} = \frac{2z}{(1+z)} \qquad (6.3.3)$$

The composite echo is then the sum of the signal reflected from the junction and the signal that has travelled the additional path in the sensor. The composite echo of the overlapped pulses is then:

$$C = R + T_{12}T_{21}. \qquad (6.3.4)$$

The ratio of reflected to transmitted pulses is more easily measured in practice and is given by

$$R/T_{12}T_{21} = \frac{1-z^2}{4z} \qquad (6.3.5)$$

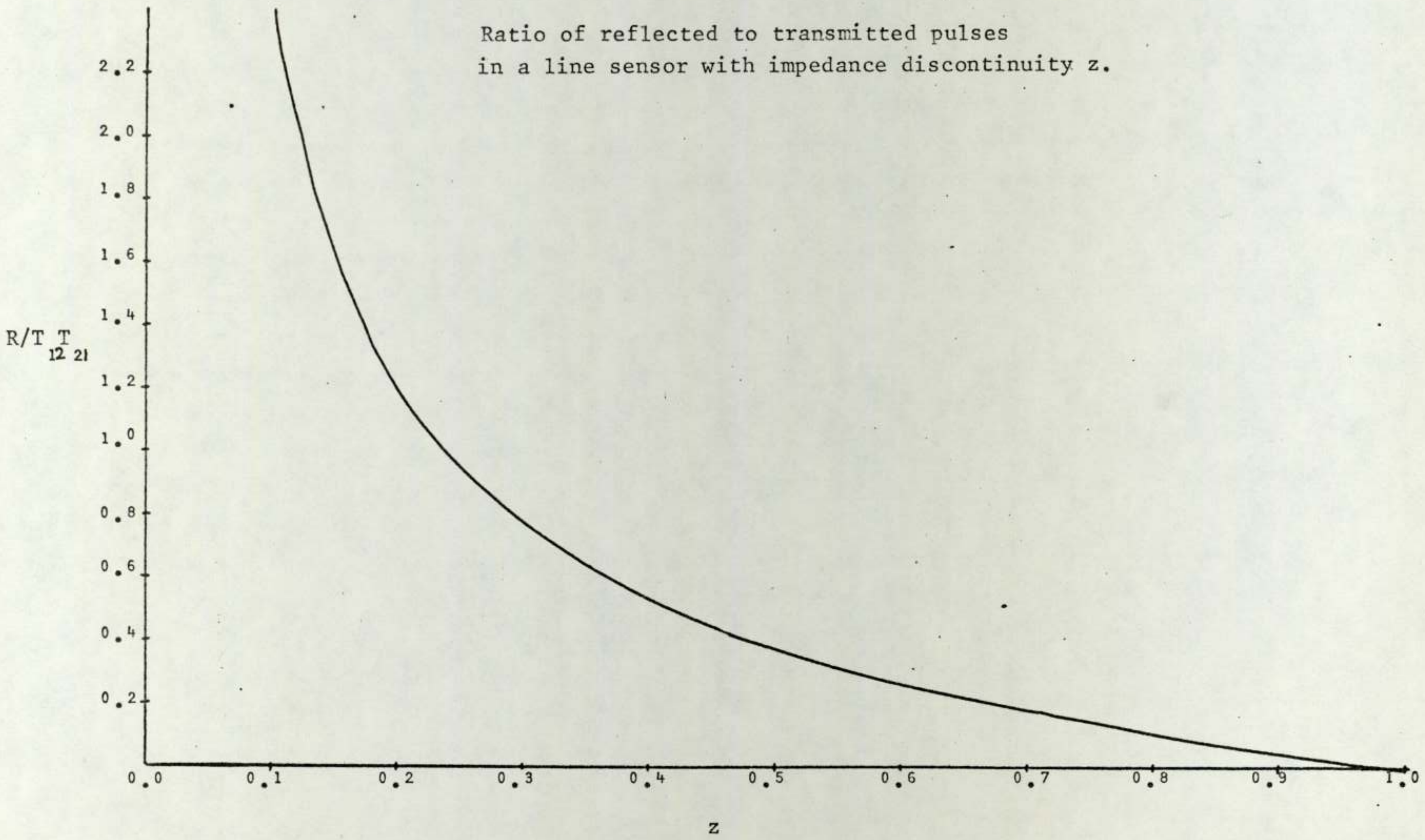

Ratio of reflected to transmitted pulses
in a line sensor with impedance discontinuity z.

FIGURE 6.4

Figure 6.4 shows this ratio as a function of z. Figure 6.3(a) was obtained using a sensor of 1 mm 2% thoriated tungsten butt welded to a 1.5 mm line of the same material. These figures correspond to an impedance ratio of about 0.44. The measured ratio of pulse heights is 0.43 compared to a calculated ratio of 0.46. The variation of the ratio R/T_1T_2 is shown in Figure 6.4 as a function of z over the range 0.1 to 1.0. Clearly the case of $z = 1.0$ represents the absence of an impedance mismatch and there is no reflection.

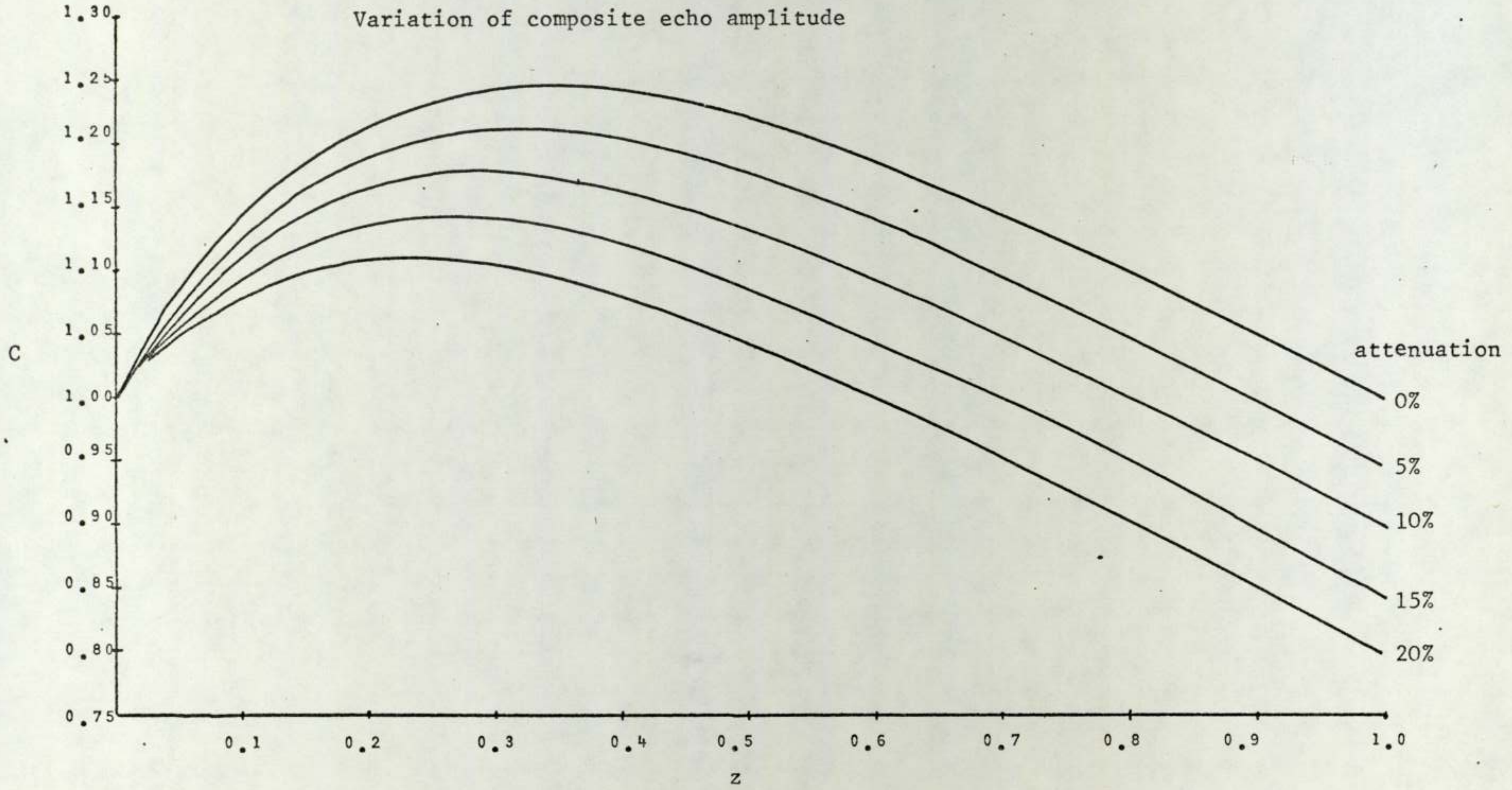
Variation of composite echo amplitude
C
1.30
1.25
1.20
1.15
1.10
1.05
1.00
0.95
0.90
0.85
0.80
0.75
0.1
0.2
0.3
0.4
0.5
0.6
0.7
0.8
0.9
1.0
z
attenuation
0%
5%
10%
15%
20%

FIGURE 6.5

6.4 Factors Affecting Choice of Z_2/Z_1 Ratio

The impedance ratio Z_2/Z_1 can be controlled by selecting the ratio of diameters of the lead-in line to sensor line. To optimise the signal to noise ratio the composite echo signal should be made as large as possible. While the ratio of reflected to transmitted signal is infinitely variable, this is not true of the amplitude of the composite echo signal. Figure 6.5 shows the variation of composite signal amplitude relative to the incident signal over the range of z of 0 to 1. A family of curves is given where the attenuation figure shown is the percentage of additional attenuation in the sensor line. It is preferable to maximise the combined signal at its high temperature and hence high attenuation than maximise it at room temperature. For example, the maximum composite echo amplitude with no attenuation is 1.25 and occurs for an impedance ratio of 0.35. At 20% attenuation at this z, the signal falls by about 12½%. However, if the signal is maximised at the 20% attenuation, an amplitude of 1.11 corresponding to a z of 0.20 it will have fallen by only about 8%.

Arave and Buchenauer(45) give attenuation for tungsten - 2% thoria, up to 2800°C. If β is the attenuation in Neper/unit length, then the attenuation in dB is given by

$$\text{Attenuation (dB/unit length)} = 8.686\beta \qquad (6.4.1)$$

For a sensor length of 150 mm the expected attenuations are shown in Table 6.1.

TEMPERATURE	ATTENTUATION	
	dB	%
1600	-	-
2000	1.6	17
2400	5.9	50
2800	10.3	70

Calculated on the basis of data given in Reference 45 for a 150 mm W-2% Thoria sensor

Table 6.1

The available furnace for testing the probe was only capable of achieving a temperature of 1800°C. For this reason the sensor was optimised for an expected attentuation of about 10%. From the curves in Figure 6.5 the maximum for 10% attenuation occurs at about $z = 0.3$. Since the lead in line and the sensor are made from the same material the ratio of the diameters is

$$\frac{d_2}{d_1} = \sqrt{0.3} = 0.55$$

The sensor was machined from a solid length of tungsten 1.5m long and 1.5 mm diameter, this gives a sensor diameter of 0.82 mm.

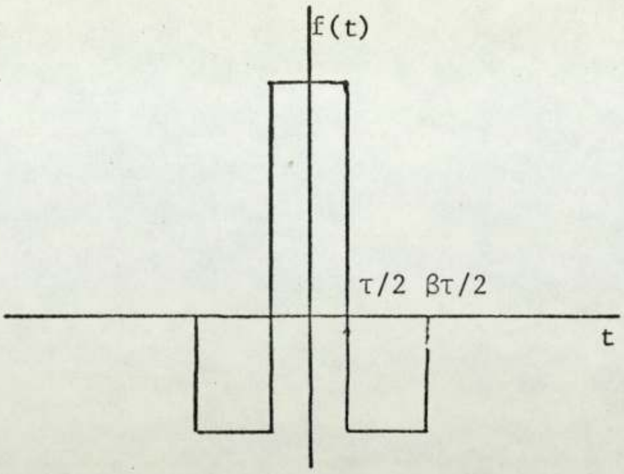

Idealised echo waveform

FIGURE 6.6.a

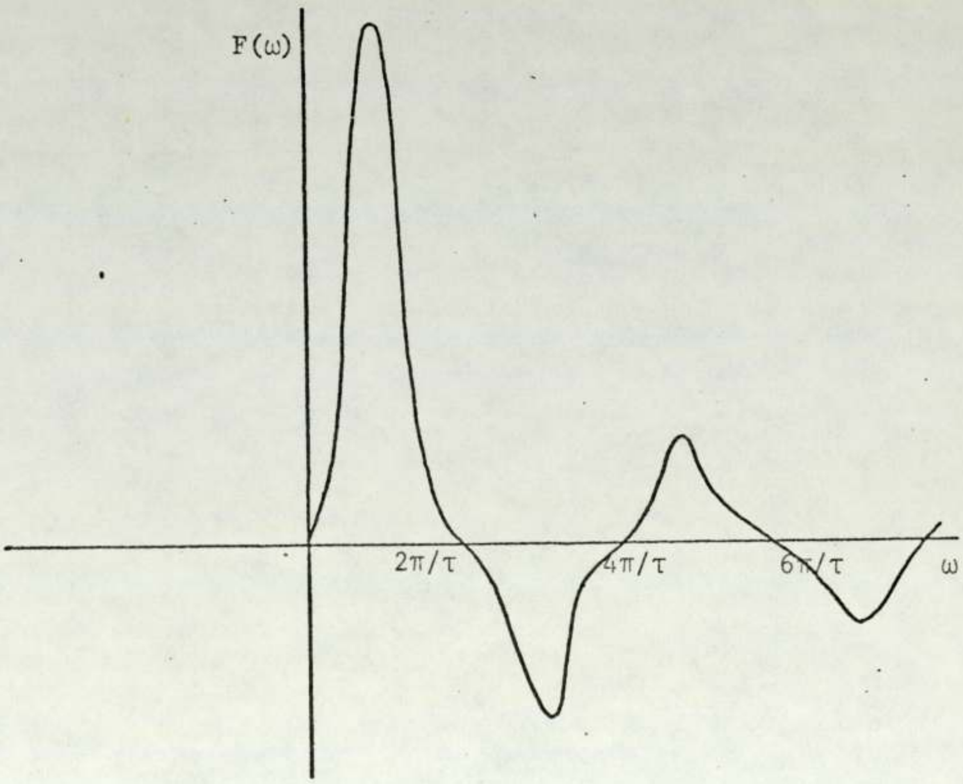

Spectrum of echo waveform

FIGURE 6.6.b

6.5 Young's Modulus Measurement by Pulse Transmission

The theory of pulses in transmission lines has been discussed by several authors(46-48). For an idealised rectangular pulse input the received echo waveform as shown in Figure 6.6(a) is produced. Figure 6.6(b) shows the Fourier spectrum of a pulse of this shape. In practice the pulse shape differs from this rectangular shape as a result of finite speeds of rising and falling edges and also as a result of fringing effects in the transducer coil(47). Most of the energy in the pulse can then be considered to occur at frequencies less than $2\pi/T$. Since the pulse width is approximately 4μs this corresponds to a frequency of 250 kHz.

The value of sensor diameter given above and this frequency gives a value of normalised frequency parameter for tungsten (as defined in Chapter 2) of approximately 0.2. Inspection of Figure 2.1(a) shows that the first longitudinal mode (L(0,1)) is essentially linear in this region and hence the group and phase velocity take the same value. This means that the frequency components of the pulse spectrum travel with the same velocity and there is no dispersion thus preserving the pulse shape independent of delay time. Under these conditions the pulse propagates with velocity (Appendix 6.1).

$$C_g = C_\phi = C_o = (E/\rho)^{\frac{1}{2}} \qquad (6.5.1)$$

Accurate absolute measurement of Young's modulus for a material depends on accurate knowledge of the dimensions of the sensor. Changes in Young's modulus can be inferred from flight time information without this knowledge. The method of estimating Young's modulus change is from equation (6.5.2).

$$E_o = \left(\frac{2\ell_o}{\tau_o}\right)^2 \rho \qquad (6.5.2)$$

where ℓ is the room temperature sensor length and τ_o is the delay at room temperature.

The ratio of Young's modulus at temperature θ, E_θ to the room temperature value E_o is given by

$$\frac{E_\theta}{E_o} = \left(\frac{\tau_o}{\tau_\theta}\right)^2 (1+\alpha\theta) \qquad (6.5.3)$$

The factor α in (6.5.3) is the thermal coefficient of linear expansion and can generally be considered small and is not taken into account in the following.

An instrument was designed to track small changes in time of flight with temperature. This instrument, based on the pulse overlap method, is described fully in Chapter 7.

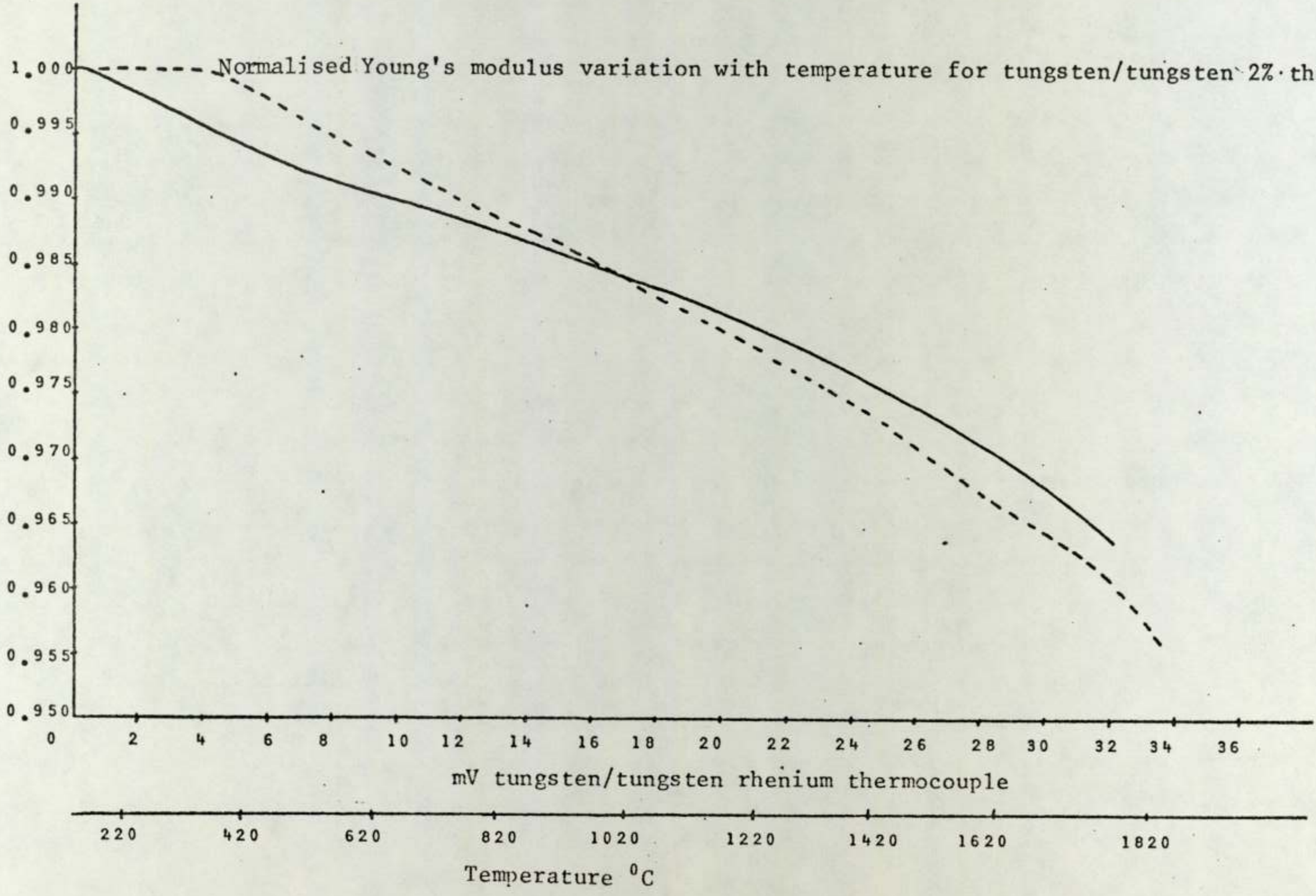

Normalised Young's modulus variation with temperature for tungsten/tungsten 2% thoria

FIGURE 6.7

6.6 Temperature Coefficient of Young's Modulus

A sensor as described in Section 6.4 was machined from tungsten - 2% thoria. It was installed in a Metals Research PCA10 furnace capable of a maximum temperature of 1800°C. Temperature was monitored using a tungsten/tungsten rhenium thermocouple.

The operating procedure of the flight time tracking instrument is as follows. The echo pulses were overlapped by manually tuning the echo pulse oscillator and observing the composite echo on an oscilloscope. The instrument was then switched to automatic track and no further manual tuning was required over the temperature range of the furnace. The echo was continually monitored on the oscilloscope to check that tracking lock was maintained. The period of the oscillator with the instrument in lock is the flight time in the sensor. Period and thermocouple e.m.f. were recorded automatically at two minute intervals on a teletype using a Solatron Data Transfer Unit. Figure 6.7 shows the variation of Young's modulus normalised to the room temperature value over the temperature range 0-1800°C. The total variation of Young's modulus is about 5%. The first temperature cycle is for the sample in "as received" metallurgical condition. The second temperature cycle shows some variation resulting from the annealing of the sensor. The Young's modulus of the annealed sensor is slightly higher than the un-annealed sensor, a feature common to other metals. Dislocations and imperfections which tend to reduce Young's modulus are removed during annealing resulting in increased material strength. There is an indication of a change of slope of the second heating cycle at about 1700°C, although insufficient data points are available to confirm this. However, it is known that at the recyrstallisation temperature (about half the melting point) mobile grain boundaries result in easier deformation.

The room temperature velocity value for one sample was measured as 4659 ms^{-1}. Appendix A6.2 describes a standing wave method of measuring the velocity of the same probe and shows very good agreement.

First Temperature Cycle

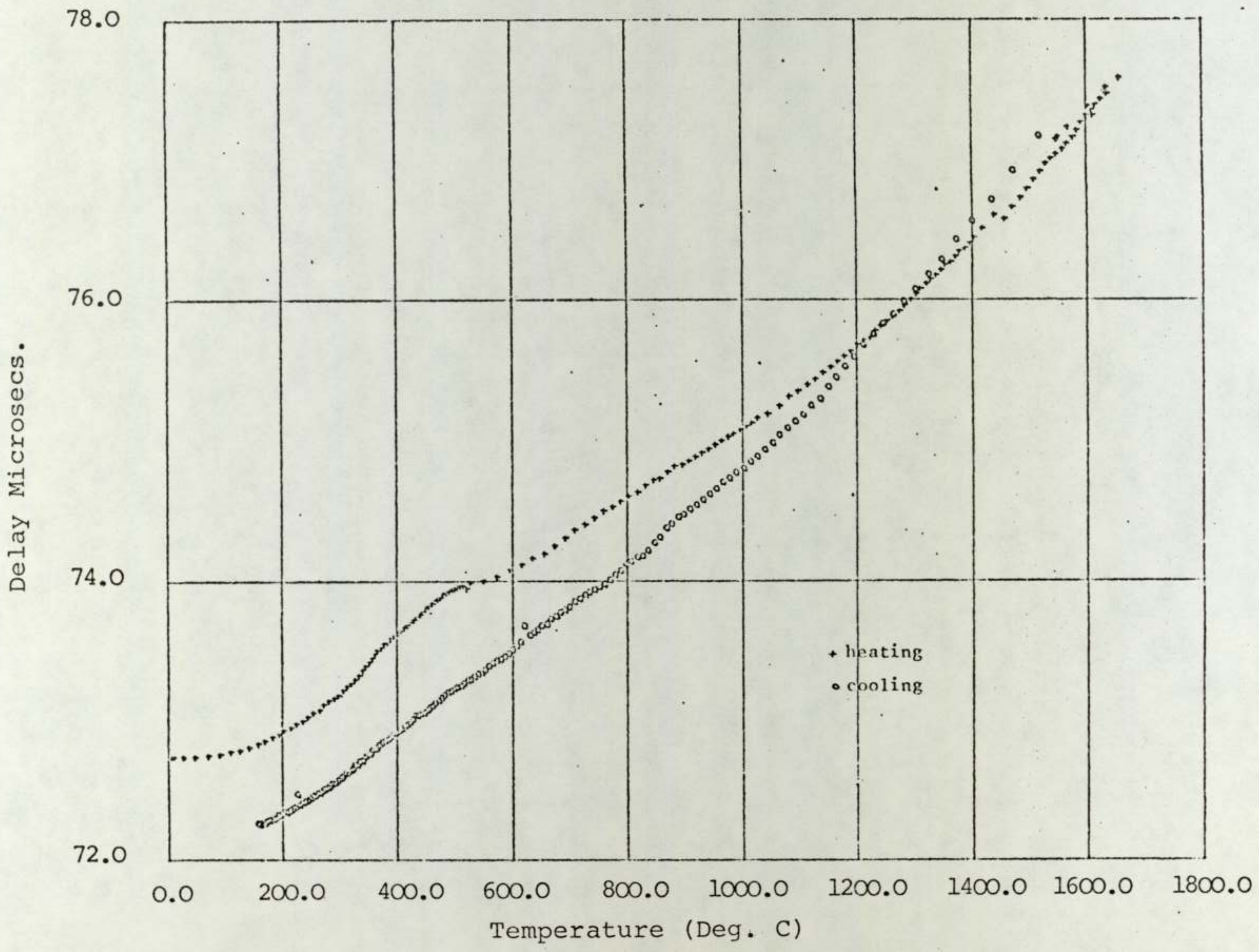

Figure 6.8

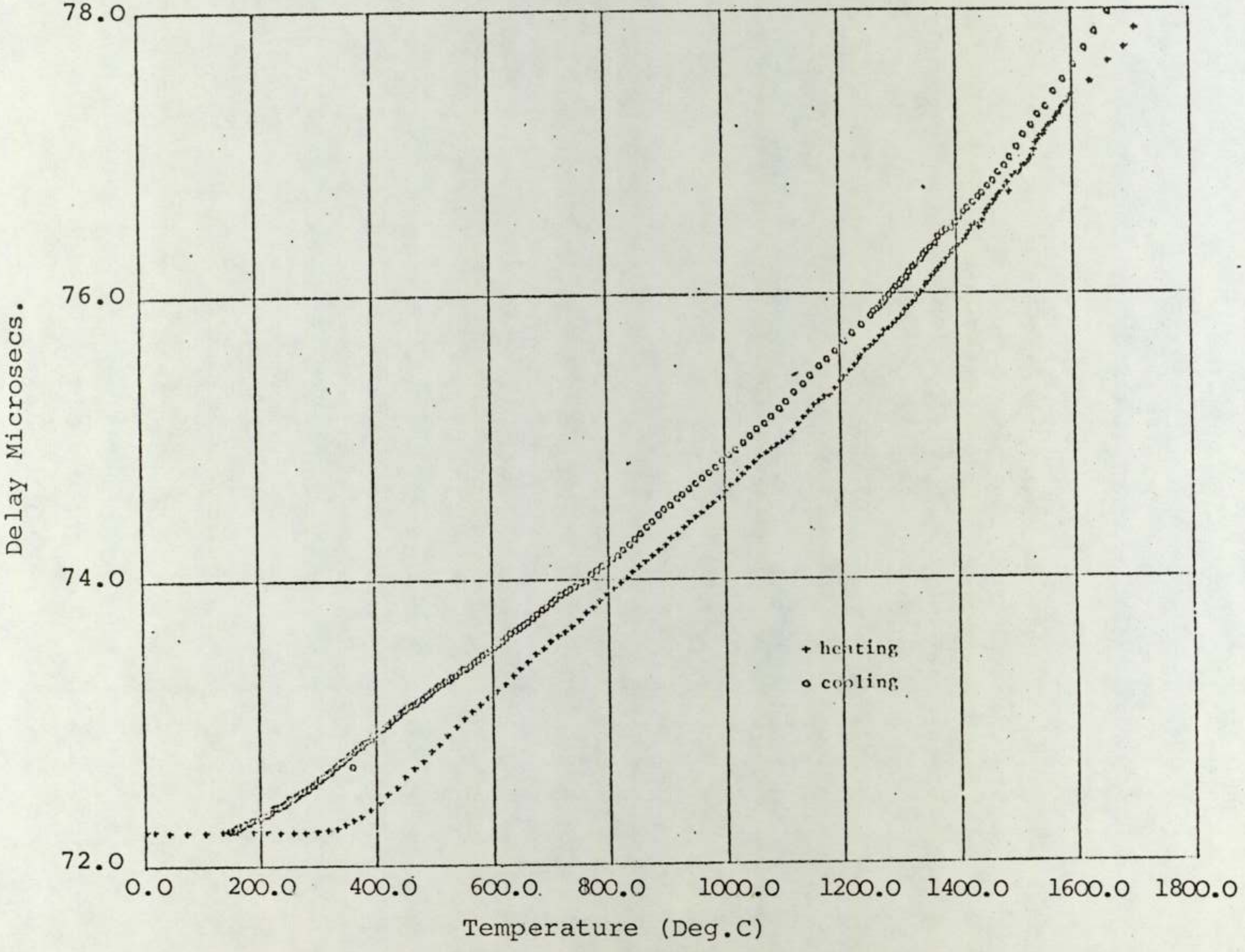
Second Temperature Cycle

Figure 6.9

First Run Delay v. Temperature

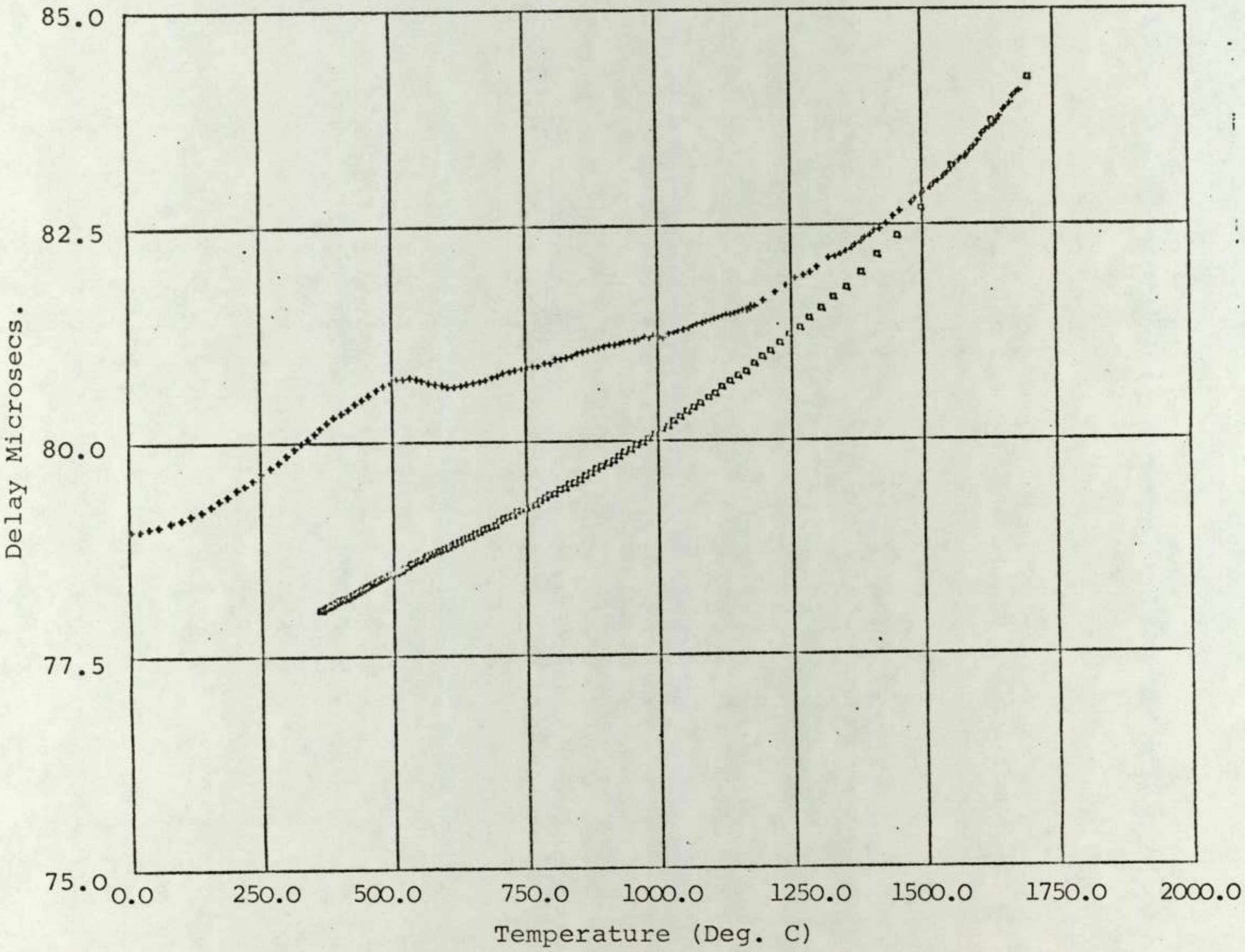

Figure 6.10

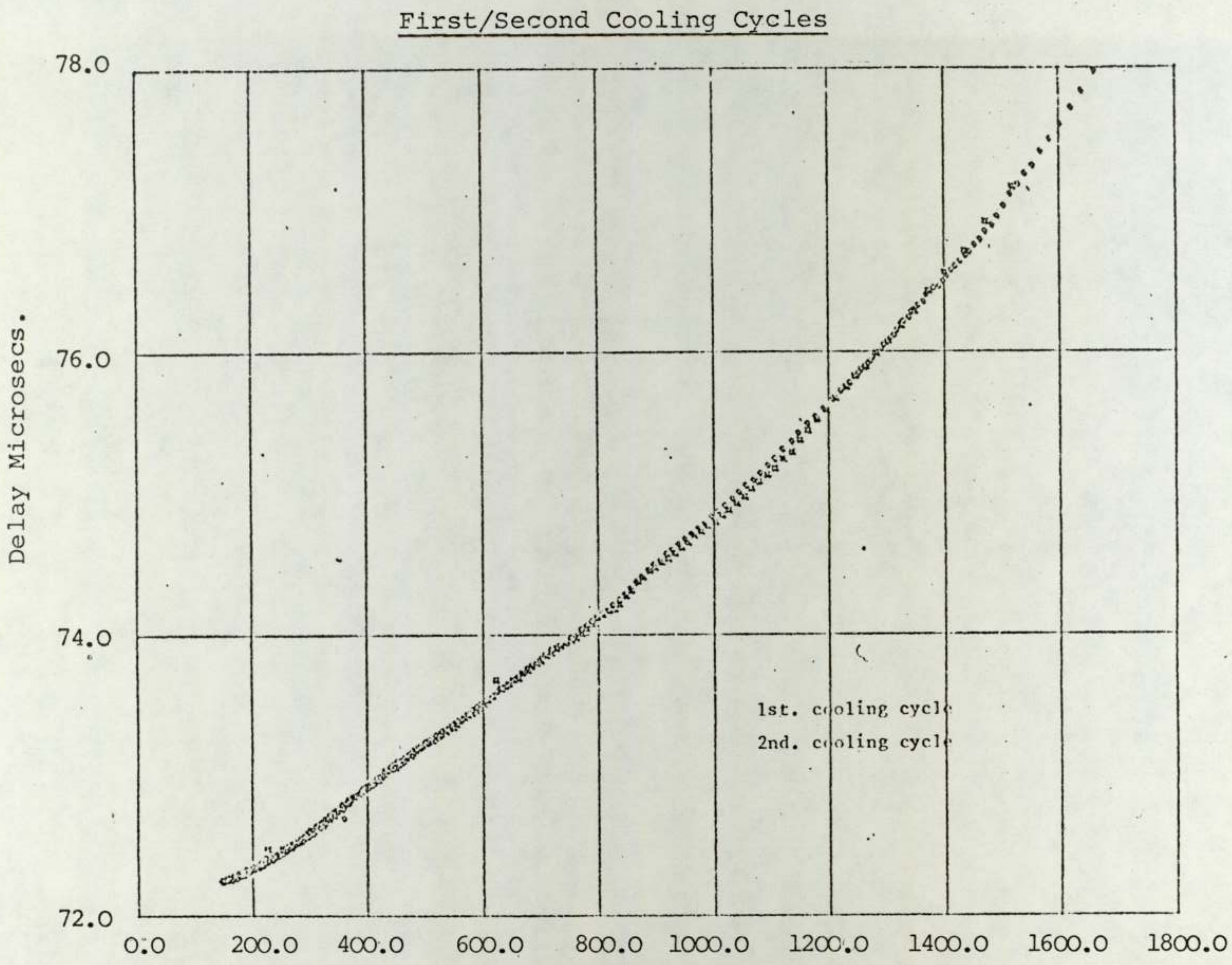

First/Second Cooling Cycles

Figure 6.11

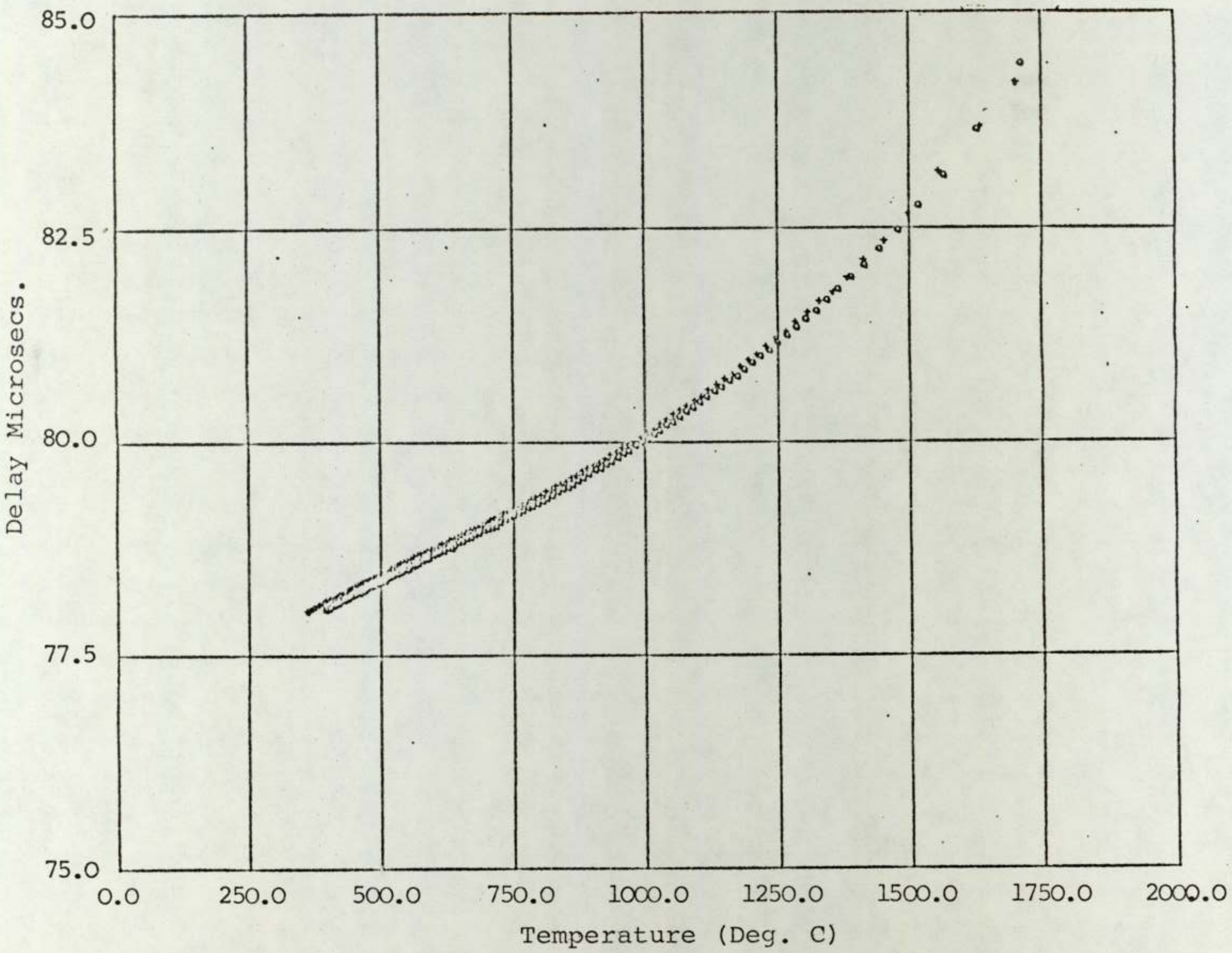

First/Second Cooling Runs Del. (Sensor 2)

Figure 6.12

6.7 The Sensor as a Temperature Transducer

The first and second temperature cycles are shown in Figures 6.8 and 6.9 respectively. There is a definite knee in the heating curve of the first cycle that is not apparent in the second cycle. This is most likely due to removal of dislocations by annealing. It is interesting to note that a second specimen also shows this knee at the same temperature (Figure 6.10).

The considerable difference between the heating and cooling curves of Figure 6.9 is almost entirely due to the different rates of heating in the furnace rather than hysteresis in the specimen. Figures 6.11 and 6.12 show the first and second cooling curves of two different specimens plotted together. Hysteresis is not as pronounced in this case indicating that the differences in Figure 6.9 are almost certainly due to the differential thermal time constants of the tungsten/tungsten rhenium thermocouple and the sensor.

The implication of the above results is that before such a sensor could be used as a temperature transducer, several heating and cooling cycles (five or six) are necessary before calibration, in order to stabilise the transducer. Also, the transducer should be calibrated at several spot values both during heating and cooling, allowing sufficient time for the transducer to reach thermal equilibrium at each point.

CHAPTER 7

INSTRUMENTATION OF TIME OF FLIGHT TRACKING

- 7.1 Introduction
- 7.2 Modified Pulse Overlap Technique
- 7.3 The Electronic System
    - 7.3.1 Pulse Selection Circuitry
    - 7.3.2 The P.R.I. Oscillation
    - 7.3.3 The Receiver
- 7.4 Performance

CHAPTER 7

INSTRUMENTATION FOR TIME OF FLIGHT TRACKING

7.1 Introduction

The measurement of variation of flight of time of an ultrasonic pulse over a wide temperature is a tedious process if carried out manually. A typical measurement cycle in Chapter 6 takes over six hours.

In this chapter an automatic system is described which, after initially locked onto the pulse, will track the flight time variation over a wide range with good accuracy. The measurements discussed in Chapter 6 were obtained using this instrument.

The instrument was initially designed as a pulse ultrasonic thermometer for nuclear fuel rod centre line temperature measurement, but clearly it is not restricted solely to the measurement of temperature. Since, primarily it is the variation of velocity that is being measured, the additional effect of parameters such as magnetic field or neutron flux could be determined.

The technique of using double pulse overlap has already been explained in Chapter 6. The two pulses transmitted every pulse repetition interval (P.R.I.), are derived from a voltage controlled oscillator, the period of which, at overlap is the two way flight time in the sensor. This

V.C.O. is continuously adjustable over a finite range. The stability of the V.C.O. is a possible limitation of the accuracy in both manual and automatic mode. In the former it arises from the time interval between setting the composite echo amplitude and observing the period. In the latter there is a random fluctuation about the mean period due to what is essentially a control sampling system.

7.2 Modified Pulse Overlap Technique

To obtain a control signal to adjust the V.C.O. automatically, a modification to the double pulse overlap method is introduced. On alternate cycles of the P.R.I. oscillator the time interval between two pulses derived from the V.C.O. is lengthened and then shortened by the same small amount. This perturbation is symmetrical about the period of the V.C.O. Figures 7.1(a) and (b) show the echo overlap situation if there was no perturbation of the second pulse and the frequency of the V.C.O. adjusted so that the echo peaks exactly coincided. In Figure 7.1(c) the second pulse is in advance of the exact overlap condition by a small amount Δt. This causes the peak of the junction echo resulting from the second pulse to be somewhere on the rising edge of the end echo from the first pulse. Similarly, by delaying the second pulse by an amount Δt as in Figure 7.1(d), the second pulse junction echo is on the falling edge of the end echo of the first pulse.

Assuming that the V.C.O. period is slightly shorter ($<\Delta t$) than the sensor flight time, then the composite of (d) and (a) of Figure 7.1 will have a peak amplitude larger than the composite of (c) and (a). The reverse will be true if the V.C.O. period is slightly greater than the flight time in the sensor. Clearly the difference between these two conditions can then be used to control the V.C.O. When the V.C.O. period is identical to the sensor flight times, the amplitude of the composite echoes of the advanced and delayed

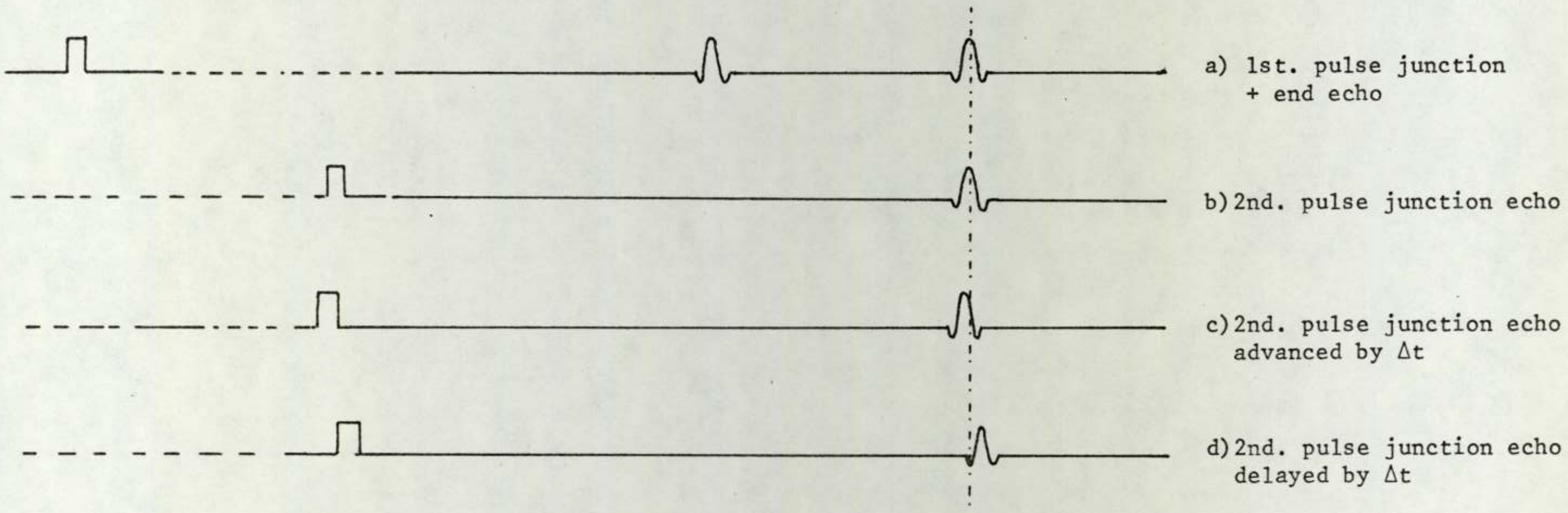

Modified double pulse overlap

FIGURE 7.1

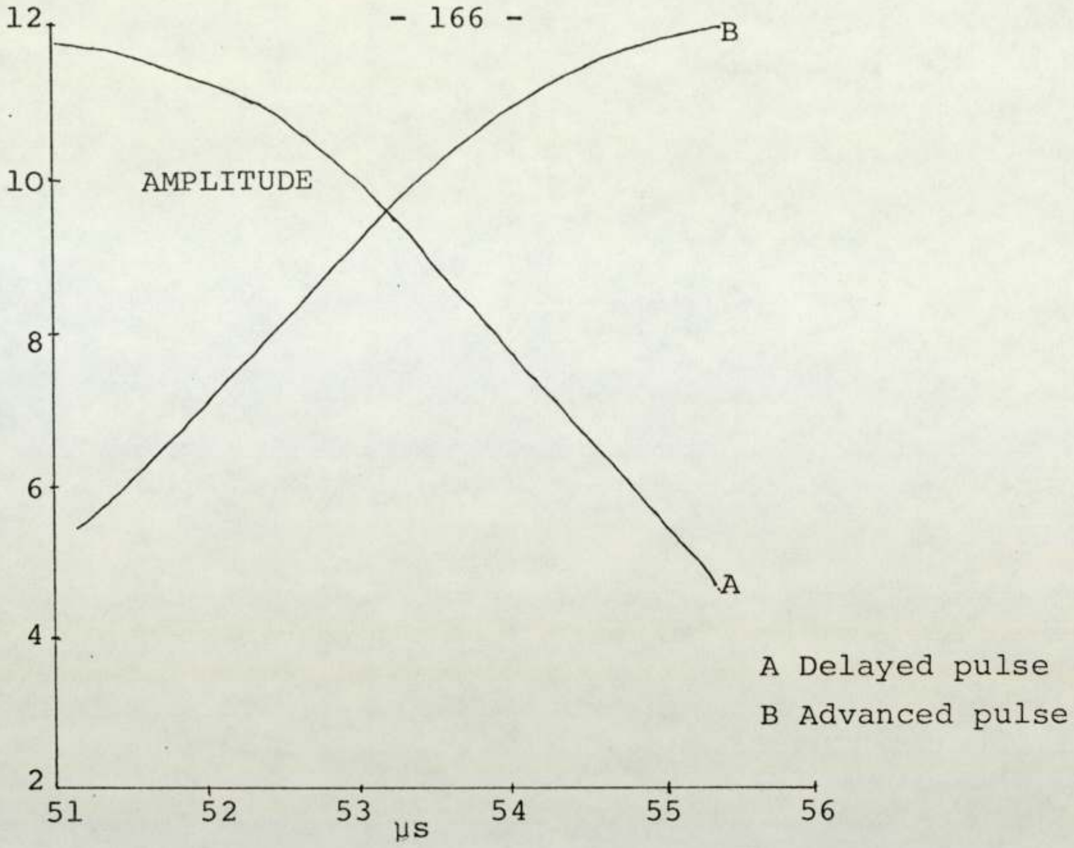

Composite pulse height

FIGURE 7.2(a)

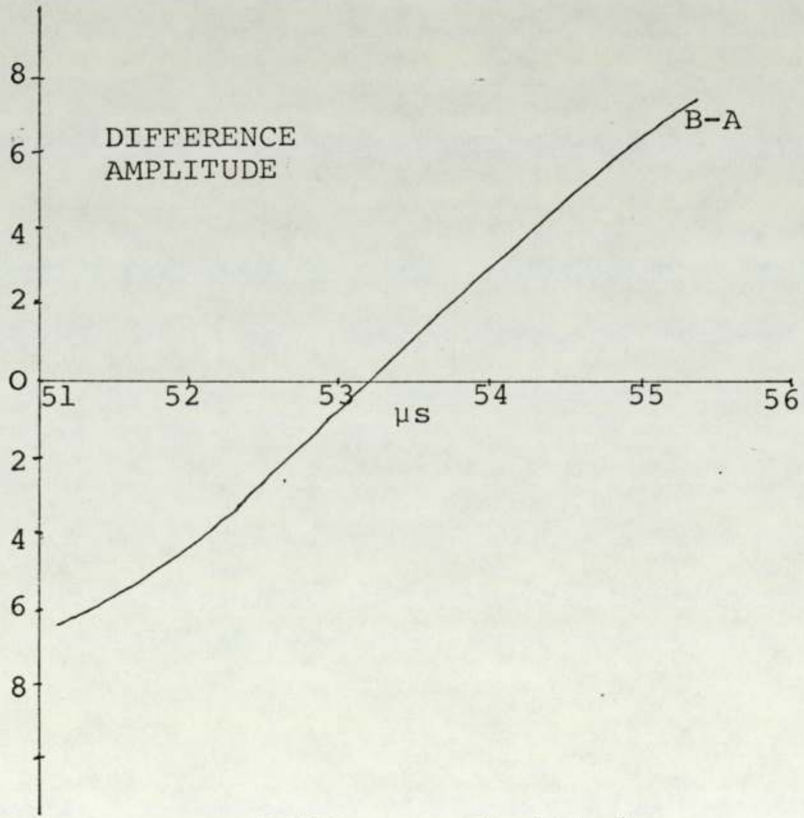

Difference Amplitude

FIGURE 7.2(b)

Pulse amplitude relationships used for tracking control.

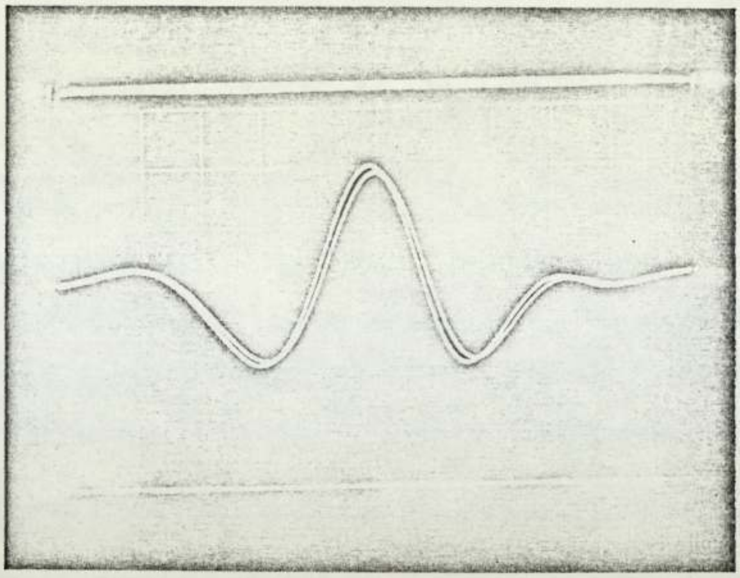

a) open loop
τ=71.529µS

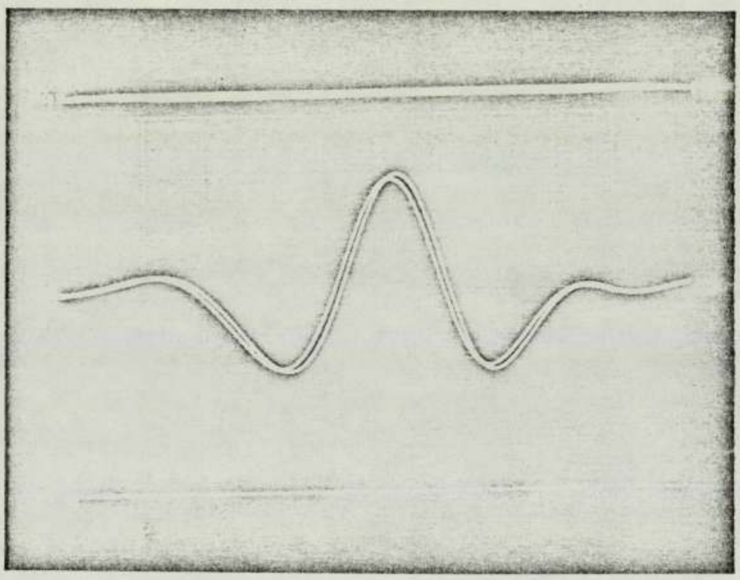

b) open loop
τ=72.357µS

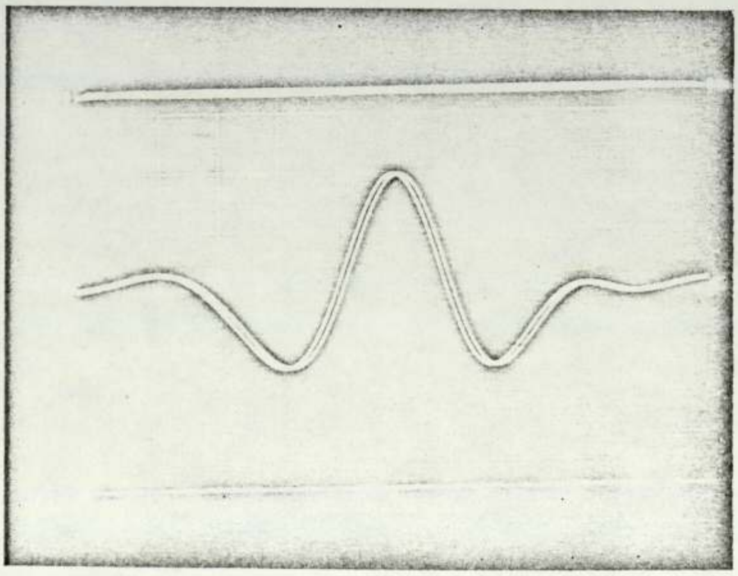

c) closed loop
τ=71.893µS

The composite echoes

FIGURE 7.3

pulses will be identical and hence applying zero voltage to the control I/P of the V.C.O. Figure 7.2 shows the pulse amplitudes of the advanced and delayed composite echoes in a steel sensor with a nominal flight time about 50μs from a sensor length of 125 mm. Figure 7.2(b) is the difference between the two composite pulses.

The oscilloscope photographs in Figure 7.3 show the typical composite echoes. Figures 7.3(a) and 7.3(b) are the advanced and delayed composite echoes without tracking. In Figure 7.3(a) the V.C.O. is at a slightly higher period than the flight time while Figure 7.3(b) shows the condition when the V.C.O. is at a longer period. Figure 7.3(c) shows the two composite echoes with the tracking loop closed and the V.C.O. period locked to the flight time of the ultrasonic pulse in the sensor.

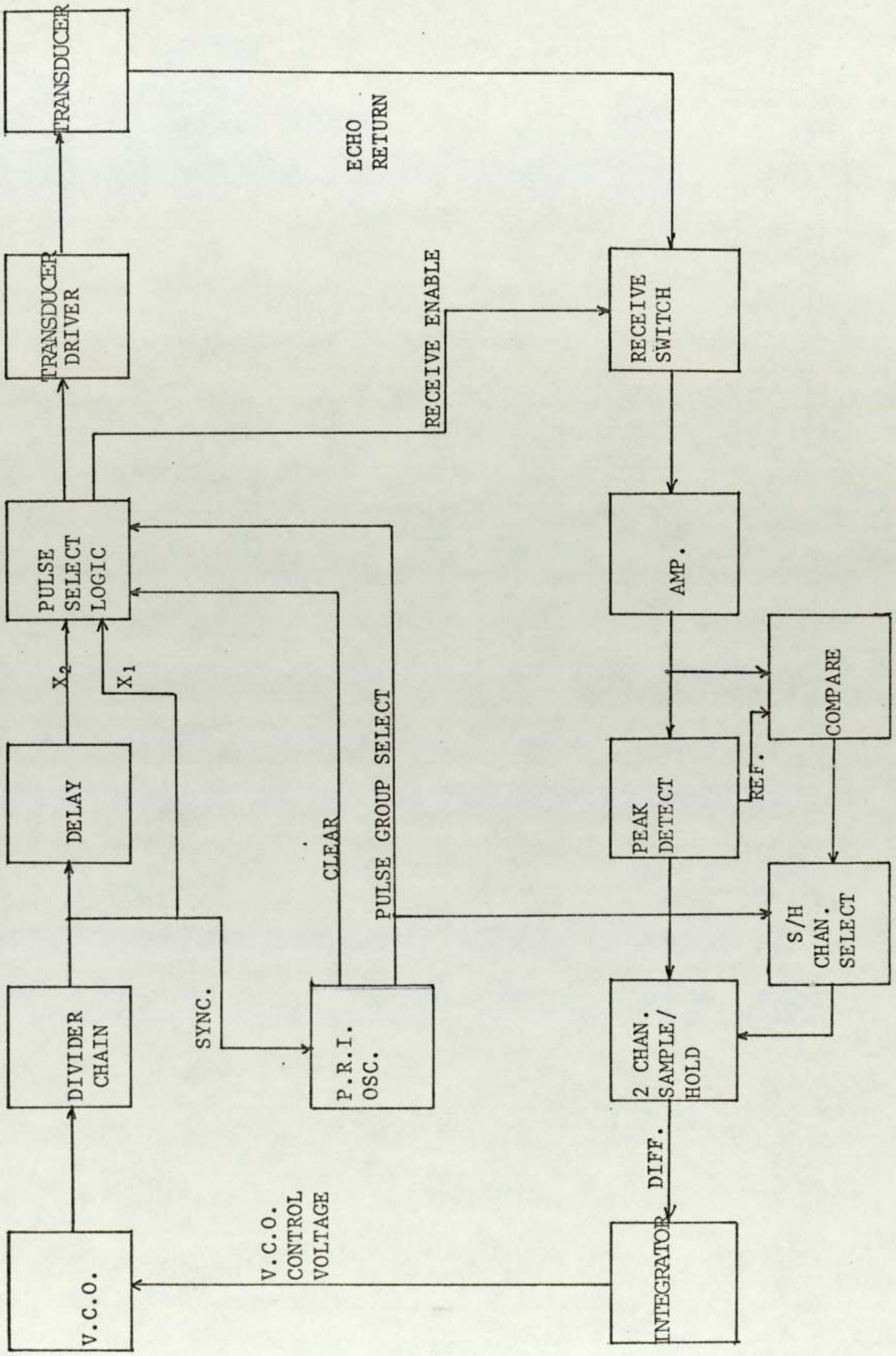

Figure 7.4 -Pulse tracking circuit block diagram

7.3 The Electronic System

The block diagram of the system is shown in Figure 7.4. There are essentially three sections. The master V.C.O. supplies the pulses via some decision logic and pulse amplifiers to the transducer. This V.C.O. has a range of 500 kHz to about 1 MHz. A divider chain reduces this frequency to a value suitable for the particular sensor in use. The rate at which the double pulses are supplied is controlled by a second oscillator of much lower frequency, variable between 10 Hz and 100 Hz. This second oscillator, the P.R.I. oscillator supplies a control to the decision logic which determines whether the advanced or delayed pulses are launched and also synchronises the receive circuitry to guide the echo returns to the correct sample hold circuits. The outputs from the sample hold circuits are subtracted and integrated before being fed back to the master V.C.O.

7.3.1 Pulse Selection Circuitry

The output from the V.C.O. and divider is a square wave of equal mark space ratio. This is the waveform X_1 in Figure 7.5. On the rising and falling edges of this waveform, very short pulses are derived, typically 50 ns which are then lengthened to between 1 and 2 μs. This waveform forms the clock to C_k in Figure 7.5,the propagation delay in the remaining logic circuitry and the width of the pulse is the total symmetrical delay about the V.C.O. frequency. The clock C_k is

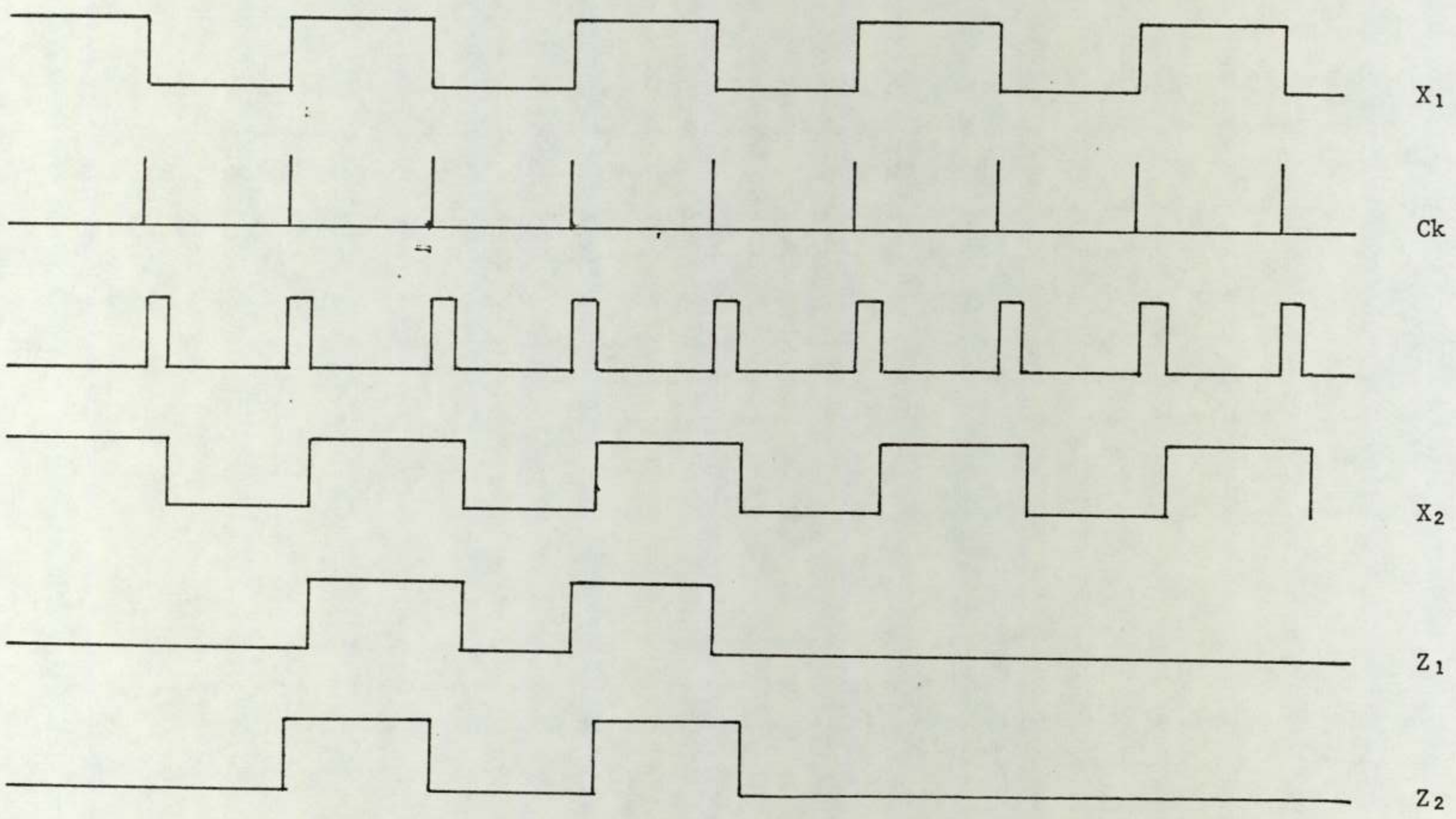

Pulse selection waveforms

FIGURE 7.5

then used to synchronise X_1 to give the waveform X_2 which is identical to X_1 but delayed by the width of the clock pulse.

The waveforms X_1, X_2 and C_k are the three main inputs to the pulse selectors. In addition there is an input C from the P.R.I. oscillator which controls whether the two pulses Z_1 or Z_2 are enabled. This occurs on alternate cycles of the P.R.I. oscillator. The two sets of pulse groups are transmitted via the same line to an amplifier which drives the transducer. The mechanism by which the relevant pulses are selected is summarised in the state map of Figure 7.6, where q denotes the circuit states. The hold state q_5 is also used to enable the receiver after the pulses have been transmitted to avoid breakthrough to the receiver.

7.3.2 The P.R.I. Oscillator

The P.R.I. oscillator is also a TTL voltage controlled oscillator with a frequency range between 10 Hz to 100 Hz. The basic function of this oscillator is to control the rate at which the pulses are launched into the transmission line. The maximum permissible rate is determined by the length of the lead-in line. Reverberations are allowed to decay sufficiently to have minimum interference with subsequent transmissions. The frequency at which the P.R.I. oscillator operates has an effect on overall accuracy, the greater the sampling rate the better the control. As is shown later this effect is an instability in the tracking loop resulting from

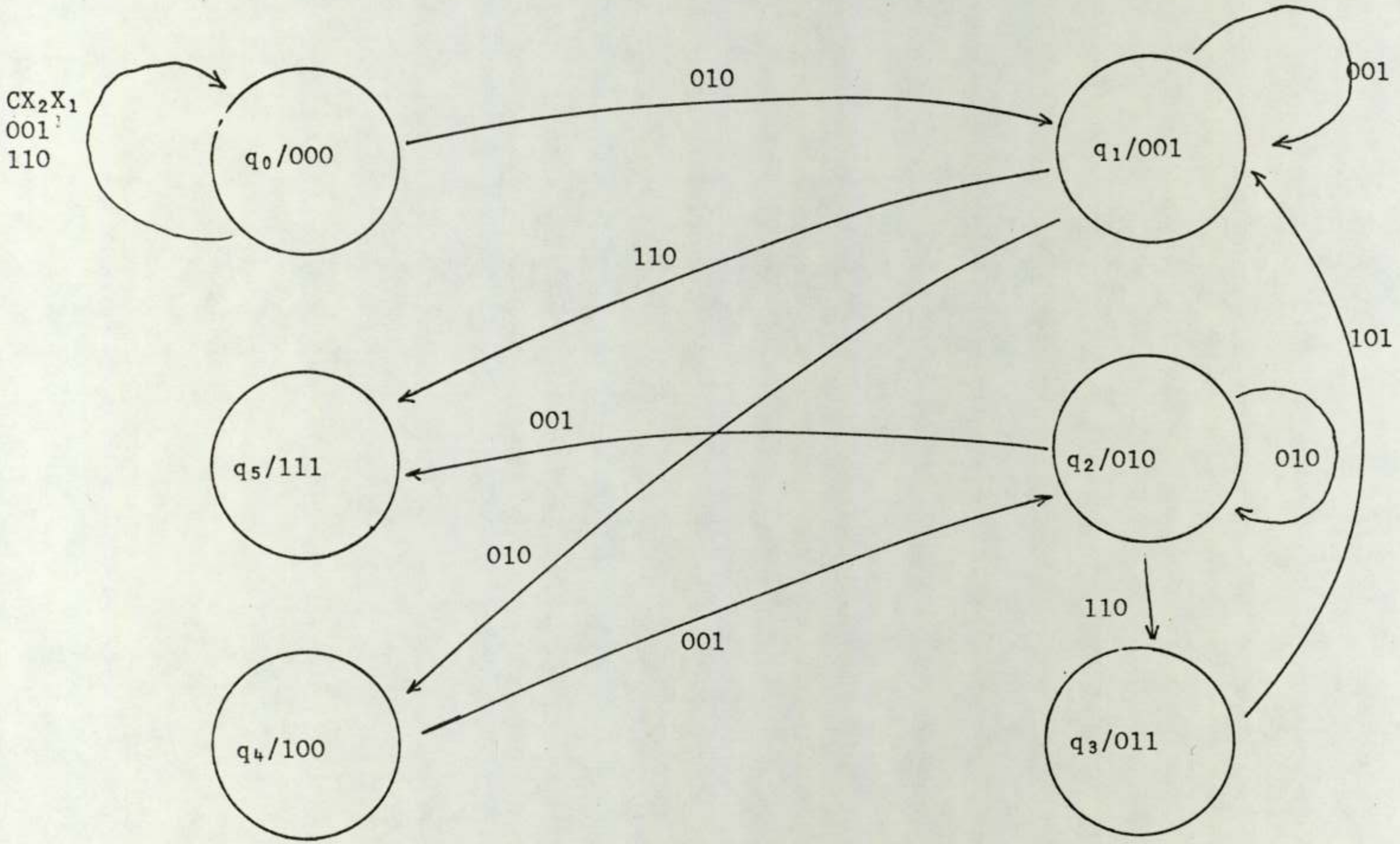

q_0-RESET
q_1-X_1 ENABLE
q_2-X_2 ENABLE
q_3-X_1&X_2 ENABLE
q_4-X_1&X_2 INHIBIT
q_5-HOLD

Pulse selector state map

FIGURE 7.6

the delay time of the pulses in the transmission line before the controlling error voltage is integrated and applied to the V.C.O.

The P.R.I. oscillator also supplies a control signal to the V.C.O. oscillator which selects delayed or advanced pulses. In addition a clear pulse is supplied to the pulse selection circuitry and also, the oscilloscope trigger is derived from the P.R.I. oscillator. A facility is included to enable either the early, late or both pulses to be viewed on the oscilloscope independently.

7.3.3 The Receiver

The function of the receiver is to amplify the echo pulses to a convenient level and gate the peak level of the pulses to the appropriate sample hold circuits. The difference between the two sample hold channel voltages (error signal) is then integrated and fed to the V.C.O. control voltage input.

Precautions have to be taken in the receiver circuitry to ensure that only the required pulse amplitudes are measured. This is achieved by the use of a comparator with the reference input taken from the peak detector. After detection of a pulse and allowing sufficient time for the sample hold circuits to acquire the new peak value, the peak detector is allowed to decay approximately 3 dB from its peak value. Subsequent peaks are then gated to the sample hold circuits if they exceed this value. Having detected a peak, the peak detector is then inhibited until the transmission of the next set of pulses.

Allowing the peak detector to decay by 3 dB imposes a restriction on the impedance mismatch between the transmission line and the sensor. This means that the amplitude of the first junction reflection must not exceed -3 dB of the composite pulse amplitude. This was not found to be a restriction in the application described in Chapter 6. However, if this is unduly restrictive in any application, it can be overcome fairly simply by ensuring that the first pulse is always detected and gating the peak detector output to the sample hold circuits on detection of the second pulse.

The complete circuitry for the time of flight tracking instrument is given in Appendix 7.

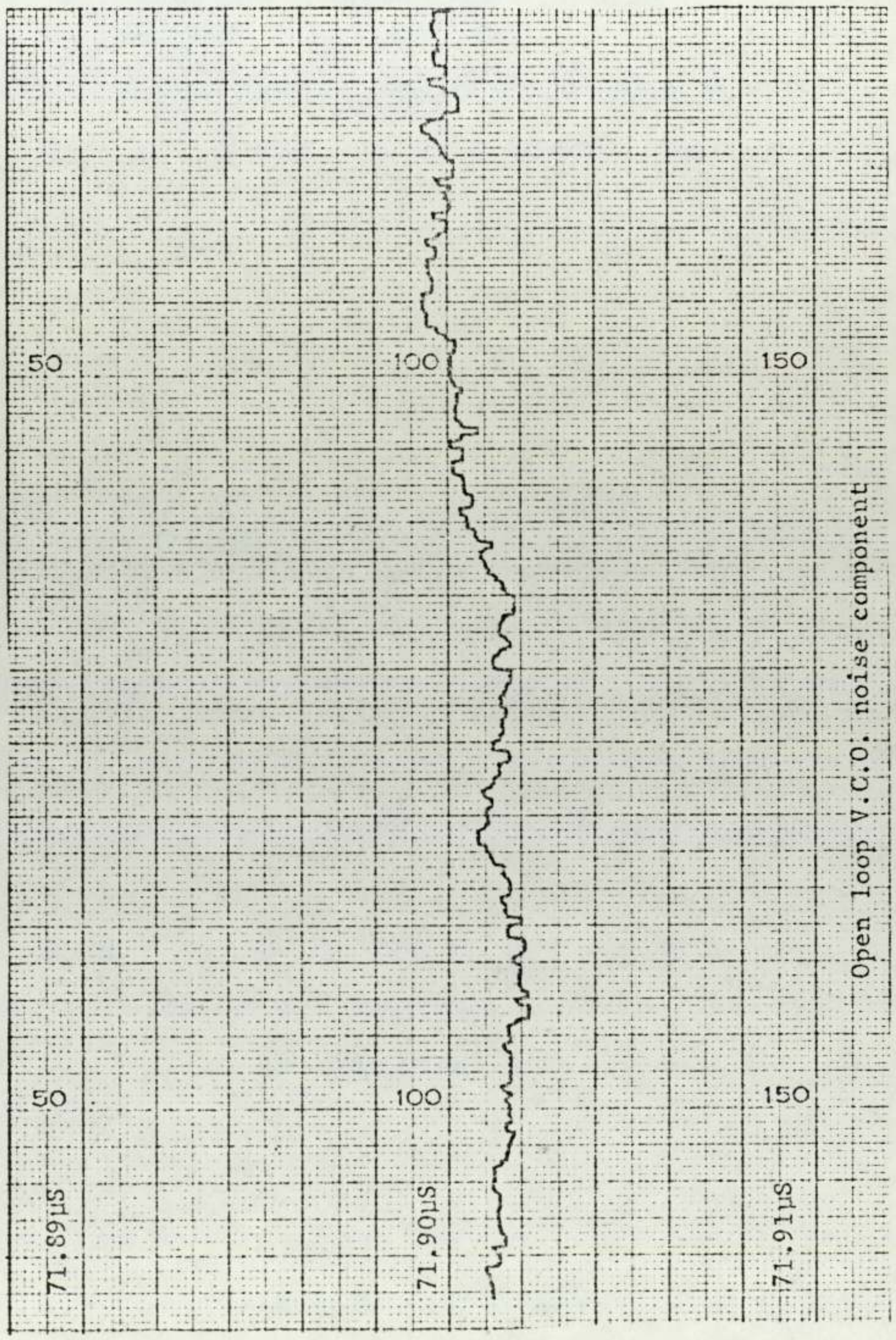

Open loop V.C.O. noise component

FIGURE 7.7

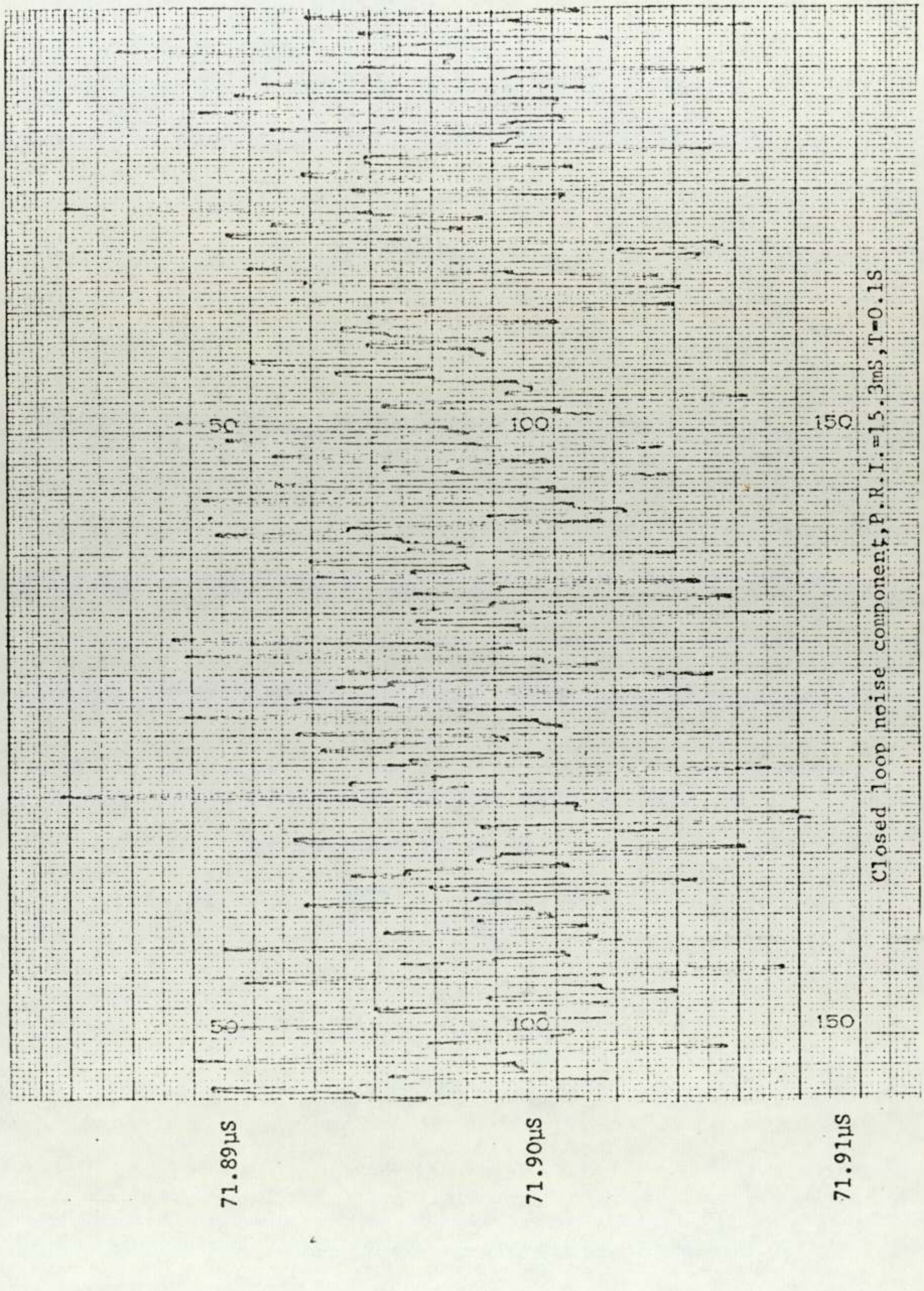

Closed loop noise component, P.R.I.=15.3mS, T=0.1S

FIGURE 7.8

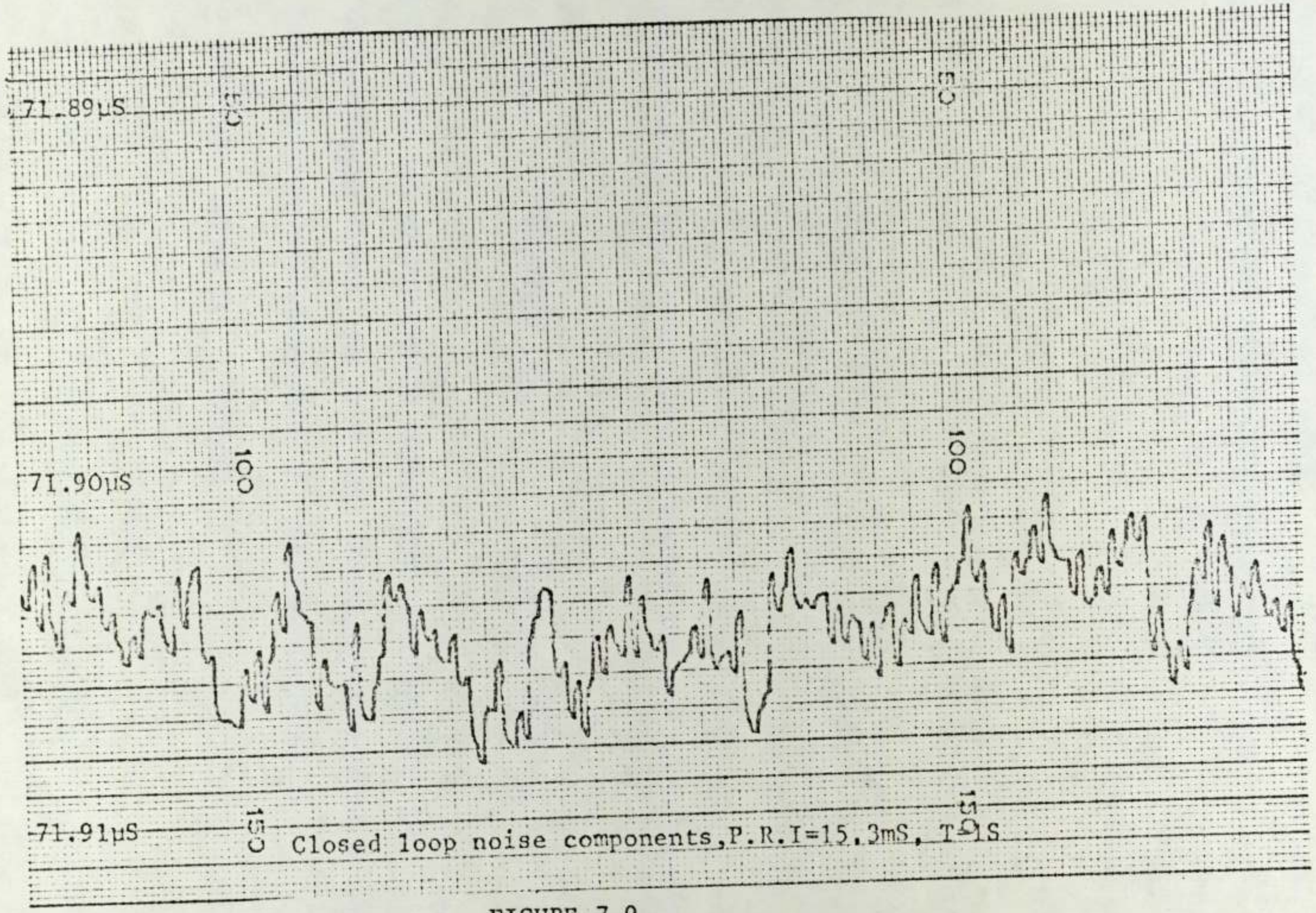

Closed loop noise components, P.R.I=15.3mS, T=1S

FIGURE 7.9

7.4 Performance

The accuracy with which flight time variations can be measured with the instrument depends on the P.R.I. oscillator period and the time constant of the final integrator. The effect of these two parameters appears as instrument noise in the period measurements of the V.C.O. Figure 7.7 shows the typical noise component of the V.C.O. when the control loop is open. A small drift is apparent due to temperature variations in the V.C.O. This long term drift is of no importance in closed loop since the V.C.O. period is controlled by the flight of the time in the sensor.

In closed loop, the noise component is a function of both the integrator time constant and the P.R.I. period. Figures 7.8 and 7.9 show the typical noise for a nominal P.R.I. period of 15 ms with the integrator time constants of 0.1s and 1s. The dependence of the noise on these two parameters is a result of the delay time in the transmission line. This is because the integrator runs continuously and the V.C.O. period is changing during the time of travel of the pulses in the transmission line. The period of the V.C.O. is different at the instant the control signal is updated to when the pulses were transmitted. The minimum permissible time that can occur is the flight time in the lead-in line, although the P.R.I. oscillator period is usually several times this value, the requirement to avoid reverberation effects. So for an error at the V.C.O. input of e volts, the correction after one P.R.I. interval of t seconds will be et/τ where τ is the

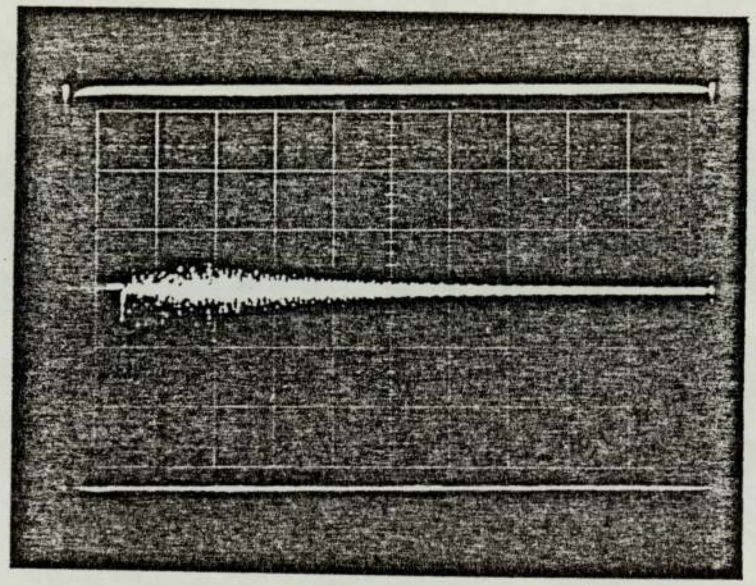

Horizontal scale 1mS./div.

Vertical scale 5V/div.

Noise build up in sensor

FIGURE 7.10

integrator time constant. Generally this will cause the V.C.O. to overshoot the required value and the overshoot is inversely proportional to the integerator time constant and proportional to the P.R.I. period. The reverberation noise is shown in Figure 7.10 and the optimum choice of P.R.I. is the smallest period where this does not contribute significantly to subsequent transmissions. This adjustment is carried out visually on the oscilloscope. Table 7.1 shows typical rms values of data noise obtained from the V.C.O. with the sensor held at a fixed temperature in the furnace.

In normal operation the instrument is designed to track a changing flight time as a function of temperature. Figures 7.11 and 7.12 show the integrator output response to a step change of 600 mV. This represents a lock in range of about 2 μs which corresponds to several hundred degrees centigrade in the case of the tungsten sensor described in Chapter 6.

P.R.I. PERIOD	INTEGRATOR TIME CONSTANT	
	0.1s	1s
Open Loop	0.5 ns	0.5 ns
10.7 ms	3.2 ns	1.2 ns
15.3 ms	5.4 ns	1.3 ns
20.9 ms	4.7 ns	1.8 ns

R.M.S. V.C.O. Period Noise

TABLE 7.1

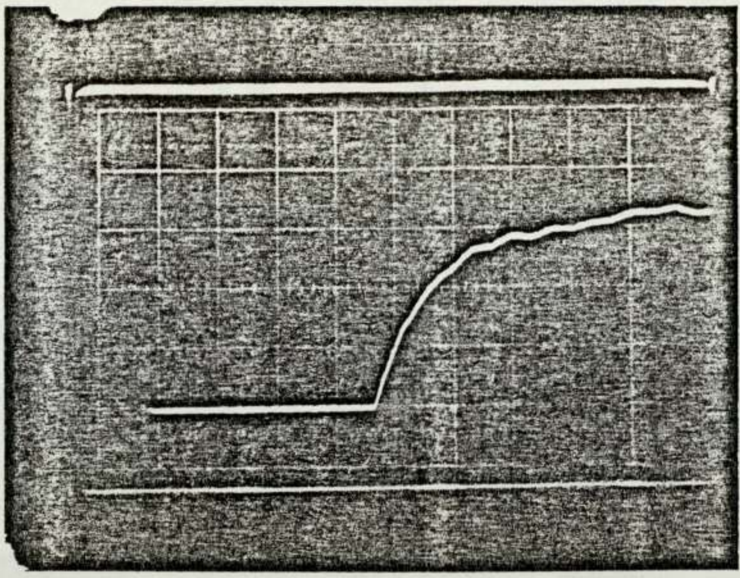

Horiz=100mS/div.
Vert=200mV/div.
I/P step 550mV

a)P.R.I.=16.9mS
T=0.1s

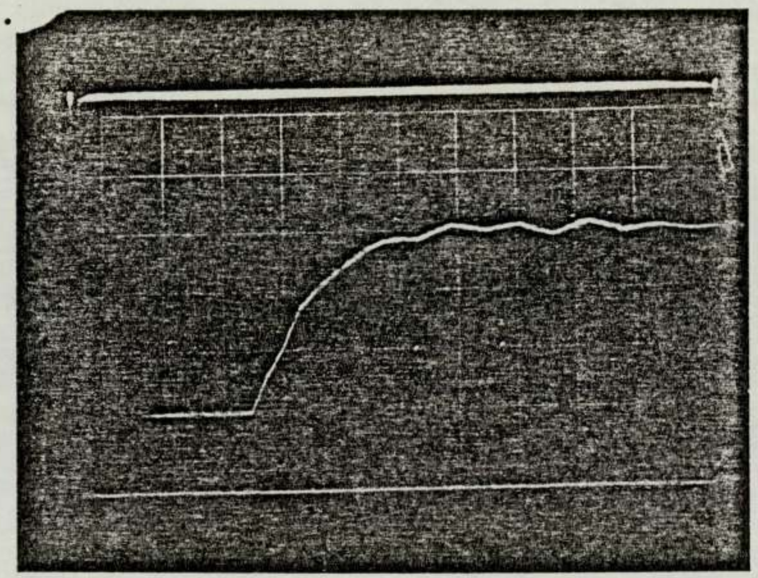

b)P.R.I.=29.05mS
T=0.1s

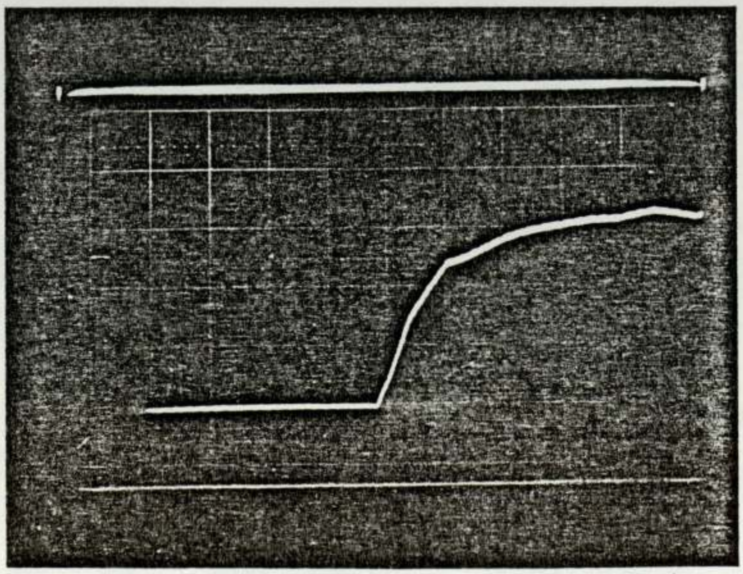

c)P.R.I.=31.6mS
T=0.1s

Integrator step response

FIGURE 7.11

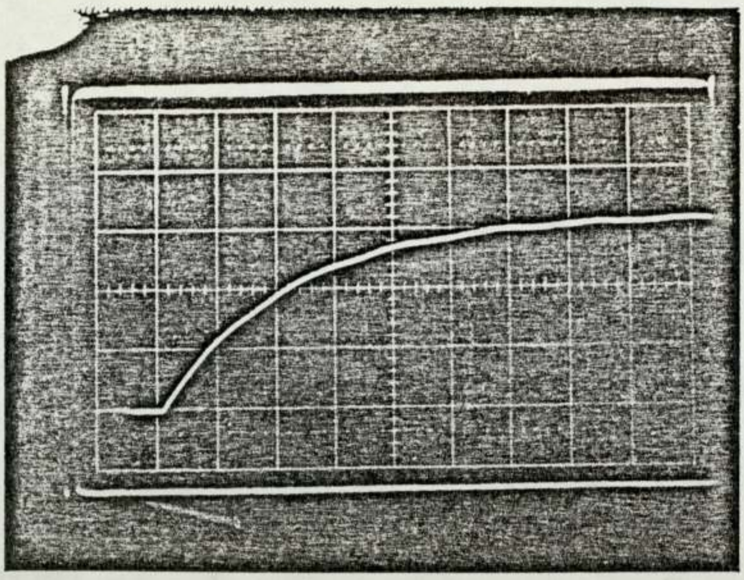

Horiz.=500mS/div.
Vert.=200mV/div.
I/P step=550mV

a) P.R.I.=10mS
T=1s

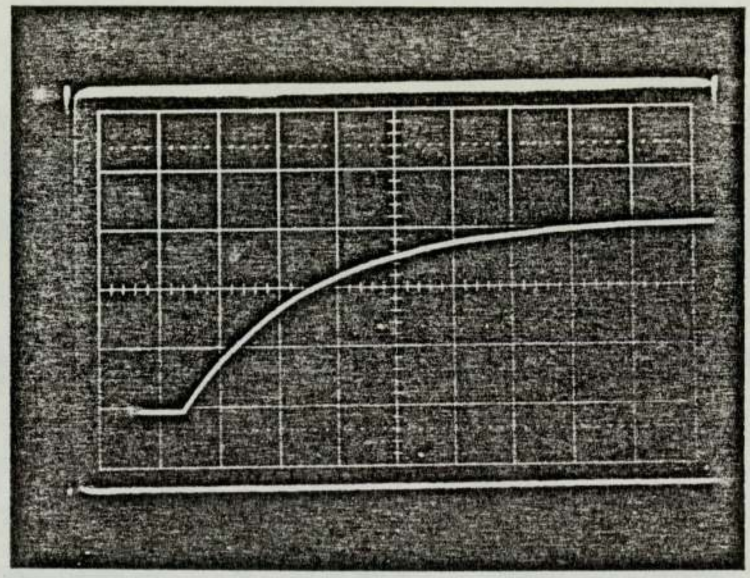

b) P.R.I.=20mS
T=1s

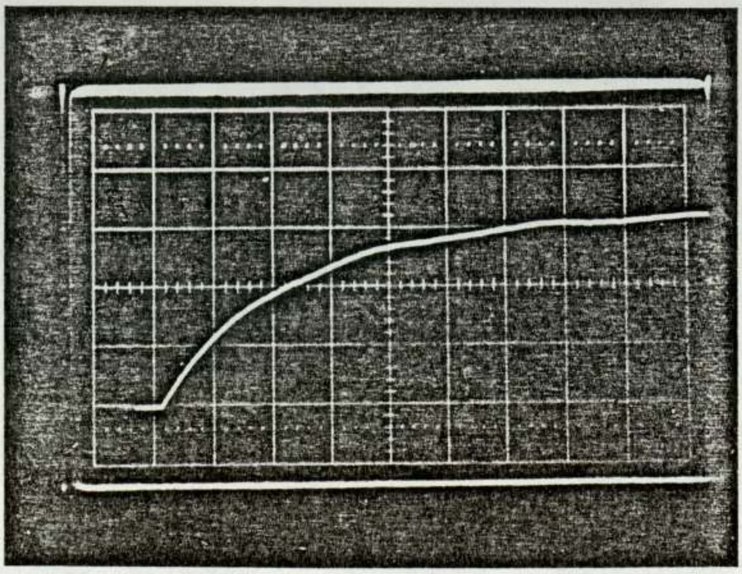

c) P.R.I.=30mS
T=1s

Integrator step response

FIGURE 7.12

With an integrator time constant of 0.1s the rise time to 90% of the final value is 400 ms. This implies that temperature changes of about 1000°C/sec can be tracked but there were no means available to check this capability in practice. The effect of a 1 second time constant is clearly visible in Figure 7.12. The rise time is clearly longer but the oscillation about the mean value is greatly reduced over the 0.1s time constant.

CHAPTER 8

CONCLUSIONS

CHAPTER 8

CONCLUSIONS

Two sensitive methods of measuring the elasticity of materials have been dealt with. The first method consists of a comparison of two known modes to give a value of Poisson's ratio and Young's modulus. A number of modal frequency ratios are given in Appendix A4.2 which allows some redundancy in the data and enhances confidence in the result. The second method is applicable to measurement of temperature changes of Young's modulus by a time of flight technique. The principle of this method is well known but a modification based on junction and end echo overlap enable the method to be automated. An instrument has been designed to accomplish this and is shown to have good flight time variation tracking accuracy. The pulse overlap method is particularly suited to high temperature measurement in hostile environments. The probe material can be chosen to suit the temperature range and environment of the application.

The disc resonance method has been applied to the measurement of the temperature coefficient of Poisson's ratio of a number of grades of graphite. It has been shown that mild anisotropy introduced by the manufacturing process can cause spurious modes of resonance. However, with careful technique it is possible to resolve the modes required to utilise the tables given in Appendix A4.2 and obtain consistent results. It is worth noting that while repeatable results can be obtained for any one particular disc from a sample, it was later found that considerable variation of Poisson's ratio can occur between discs from nominally the same material. It is not yet possible to extend this method of elastic constant measurement to generally anisotropic materials. However materials that appear isotropic in the plane of the disc can be dealt with. Pyrolytic graphite as a result of the vacuum deposition manufacturing technique has this property and its in plane Poisson's ratio and Young's modulus together with their temperature coefficients over 1000^{o}C temperature range have been successfully measured. In order to obtain the measurements it was necessary to extend previously published solutions to the disc frequency equations to include negative values of Poisson's ratio. It is also shown that the temperature variation of Young's modulus of pyrolytic graphite does not have the same form as isotropic graphite. The results would seem to confirm that the initial fall in Young's modulus of isotropic graphites is due to c axis expansion to fill the voids in the structure. In the case of pyrolytic graphite c asix expansion will not influence in plane measurements. Sufficient data has been presented to enable this method of elastic constant measurement to be used systematically for a large variety of materials with confidence.

An attractive method of measuring elastic constants would be direct measurement on an extruded bar. End resonances would have application here but require greater theoretical knowledge than exists at present. A previously unpublished spectrum of end resonance frequencies has been obtained for the longitudinal mode end resonances and the data obtained has shown good agreement with experiment. To make end resonances a viable method of elastic constant measurement theoretical values of frequency are required for higher mode end resonances. These modes have not received much attenuation in the literature, the most likely reason being that they only exist at the driving end of the bar (in contrast to the longitudinal mode end resonance). A simple method has been given for obtaining these end resonances experimentally. The theoretical approach successfully used for longitudinal mode end resonances, modified to account for the absence of a propagating mode did not give conclusive confirmation of the experimental results. The method showed a sensitivity to boundary value approximation and needs further investigation. Nevertheless, the method presented here may well show results if the boundary value approximation is chosen carefully. This may necessitate some form of iteration over the points at which the boundary value is set to zero in such a manner as to minimise the mean or r.m.s. residual stress at the end face.

APPENDICES

APPENDIX A4.1

SOLUTIONS TO THIN DISC FREQUENCY EQUATION

The data given in these tables are the eigenvalues (K) of the thin disc frequency equation normalised to the plate velocity C_p. Conversion to the eigenvalue (Ω) referred to the shear velocity C_s is achieved by multiplying each K value by a factor $\sqrt{2/(1-\sigma)}$.

SIGMA	0,1	0,2	1,1	1,2	2,1	3,1	4,1
0.00	1.84118	5.33144	1.74965	3.53782	1.65192	2.50683	3.23202
0.01	1.84886	5.33338	1.74819	3.53764	1.64396	2.49623	3.21990
0.02	1.85647	5.33533	1.74652	3.53750	1.63595	2.48547	3.20752
0.03	1.86403	5.33727	1.74464	3.53740	1.62788	2.47458	3.19491
0.04	1.87153	5.33921	1.74256	3.53735	1.61976	2.46354	3.18206
0.05	1.87898	5.34115	1.74027	3.53733	1.61158	2.45236	3.16897
0.06	1.88637	5.34309	1.73777	3.53734	1.60334	2.44104	3.15565
0.07	1.89371	5.34503	1.73507	3.53738	1.59505	2.42958	3.14211
0.08	1.90099	5.34697	1.73217	3.53745	1.58670	2.41800	3.12835
0.09	1.90822	5.34891	1.72906	3.53754	1.57830	2.40627	3.11437
0.10	1.91959	5.35084	1.72575	3.53764	1.56984	2.39442	3.10018
0.11	1.92252	5.35278	1.72223	3.53776	1.56132	2.38243	3.08577
0.12	1.92959	5.35471	1.71852	3.53788	1.55274	2.37032	3.07116
0.13	1.93661	5.35665	1.71460	3.53801	1.54410	2.35808	3.05634
0.14	1.94359	5.35858	1.71048	3.53813	1.53541	2.34571	3.04131
0.15	1.95051	5.36051	1.70617	3.53823	1.52666	2.33321	3.02608
0.16	1.95739	5.36244	1.70165	3.53832	1.51784	2.32058	3.01065
0.17	1.96421	5.36437	1.69693	3.53838	1.50897	2.30785	2.99502
0.18	1.97099	5.36630	1.69201	3.53839	1.50003	2.29495	2.97920
0.19	1.97773	5.36823	1.68690	3.53835	1.49103	2.28194	2.96317
0.20	1.98441	5.37015	1.68158	3.53825	1.48197	2.26881	2.94695
0.21	1.99105	5.37280	1.67507	3.53807	1.47284	2.25555	2.93054
0.22	1.99765	5.37401	1.67036	3.53779	1.46365	2.24216	2.91393
0.23	2.00420	5.37593	1.66445	3.53740	1.45439	2.22865	2.89712
0.24	2.01071	5.37785	1.65835	3.53687	1.44507	2.21500	2.88012
0.25	2.01717	5.37977	1.65024	3.53618	1.43568	2.20123	2.86292
0.26	2.02359	5.38159	1.64554	3.53530	1.42621	2.18733	2.84553
0.27	2.02997	5.38361	1.63884	3.53420	1.41668	2.17330	2.32795
0.28	2.03630	5.38553	1.63195	3.53283	1.40780	2.15913	2.81016
0.29	2.04260	5.38745	1.62485	3.53115	1.39740	2.14483	2.79218
0.30	2.04885	5.38936	1.61756	3.52912	1.38765	2.13040	2.77400
0.31	2.05506	5.39128	1.61007	3.52666	1.37783	2.11583	2.75563
0.32	2.06123	5.39319	1.60237	3.52371	1.36793	2.10112	2.73705
0.33	2.06736	5.39511	1.59448	3.52018	1.35795	2.08628	3.71827
0.34	2.07346	5.39702	1.58639	3.51599	1.34789	2.07129	2.69928
0.35	2.07951	5.39893	1.57809	3.51103	1.33774	2.05616	2.68009
0.36	2.08552	5.40084	1.56959	3.50518	1.32752	2.04089	2.66069
0.37	2.09150	5.40274	1.56089	3.49831	1.31721	2.02547	2.64108
0.38	2.09743	5.40465	1.55199	3.49029	1.30681	2.00990	2.62126
0.39	2.10333	5.40656	1.54288	3.48099	1.29633	1.99417	2.60122
0.40	2.10920	5.40846	1.53356	3.47029	1.28576	1.97829	2.58096
0.41	2.11502	5.41036	1.52403	3.45806	1.27509	1.96226	2.56048
0.42	2.12081	5.41227	1.51430	3.44422	1.26432	1.94606	2.53977
0.43	2.12657	5.41417	1.50435	3.42873	1.25346	1.92970	2.51884
0.44	2.13229	5.41607	1.49419	3.41156	1.24251	1.91318	2.49767
0.45	2.13797	5.41796	1.48318	3.39274	1.23144	1.89648	2.47626
0.46	2.14362	5.41986	1.47321	3.37231	1.22028	1.87961	2.45461
0.47	2.14923	5.42176	1.46239	3.35037	1.20900	1.89256	2.43271
0.48	2.15481	5.42365	1.45135	3.32699	1.19762	1.84533	2.41056
0.49	2.16036	5.42554	1.44009	3.30229	1.18612	1.82791	2.38315
0.50	2.16587	5.42743	1.42859	3.27635	1.17451	1.81030	2.36548

SIGMA	0,1	0,2	1,1	1,2	2,1	3,1	4,1
0.00	1.84118	5.33144	1.74965	3.53782	1.65192	2.50685	3.23202
-0.01	1.83345	5.32950	1.75090	3.53804	1.65982	2.51728	3.24389
-0.02	1.82566	5.32755	1.75194	3.53832	1.66767	2.52758	3.25580
-0.03	1.81780	5.32561	1.75277	3.53864	1.67546	2.53772	3.26685
-0.04	1.80989	5.32366	1.75339	3.53902	1.68320	2.54770	3.27792
-0.05	1.80191	5.32171	1.75379	3.53945	1.69088	2.55751	3.23371
-0.06	1.79386	5.31977	1.75398	3.53994	1.69351	2.56716	3.29922
-0.07	1.78576	5.31782	1.75396	3.54048	1.70607	2.57663	3.20943
-0.08	1.77758	5.31587	1.75372	3.54108	1.71359	2.53591	3.31935
-0.09	1.76934	5.31392	1.75329	3.54174	1.72104	2.59502	3.32392
-0.10	1.76104	5.31197	1.75260	3.54246	1.72844	2.60393	3.33819
-0.11	1.75266	5.31002	1.75171	3.54324	1.73577	2.61264	3.23713
-0.12	1.74422	5.30806	1.75061	3.54408	1.74365	2.62114	3.33573
-0.13	1.73570	5.30611	1.74928	3.54498	1.75027	2.62944	3.36397
-0.14	1.72711	5.30416	1.74773	3.54595	1.75742	2.63751	3.37184
-0.15	1.71845	5.30220	1.74597	3.54698	1.76452	2.64533	3.37934
-0.16	1.70971	5.30025	1.74398	3.54807	1.77154	2.65296	3.38645
-0.17	1.70090	5.29829	1.74176	3.54923	1.77851	2.66032	3.39316
-0.18	1.69201	5.29634	1.73933	3.55046	1.78540	2.66742	3.39946
-0.19	1.68305	5.29438	1.73666	3.55175	1.79225	2.67425	3.40632
-0.20	1.67400	5.29243	1.73378	3.55310	1.79898	2.68080	3.41074
-0.21	1.66487	5.29047	1.73066	3.55453	1.80568	2.68706	3.41570
-0.22	1.65566	5.28851	1.72732	3.55610	1.81227	2.69300	3.42019
-0.23	1.64637	5.28656	1.72375	3.55757	1.81879	2.69866	3.42419
-0.24	1.63699	5.28460	1.71994	3.55919	1.82524	2.70392	3.42768
-0.25	1.62752	5.28264	1.71591	3.56087	1.83159	2.70587	3.43054
-0.26	1.61797	5.28068	1.71164	3.56262	1.83786	2.71344	3.43307
-0.27	1.60832	5.27872	1.70714	3.56444	1.84404	2.71763	3.43494
-0.28	1.59859	5.27676	1.70240	3.56632	1.85011	2.72142	3.43624
-0.29	1.58876	5.27480	1.69743	3.56827	1.85608	2.72479	3.43695
-0.30	1.57883	5.27284	1.69222	3.57029	1.86195	2.72771	3.43704
-0.31	1.56880	5.27088	1.68677	3.57236	1.86769	2.73018	3.43651
-0.32	1.55868	5.26892	1.68108	3.57450	1.87331	2.73218	3.43535
-0.33	1.54845	5.26696	1.67514	3.57671	1.87880	2.73363	3.43343
-0.34	1.53812	5.26499	1.66896	3.57898	1.88415	2.73458	3.43096
-0.35	1.52769	5.26303	1.66254	3.58131	1.88935	2.73498	3.42775
-0.36	1.51714	5.26107	1.65587	3.58371	1.89438	2.73481	3.42579
-0.37	1.50649	5.25911	1.64894	3.58616	1.89924	2.73404	3.41911
-0.38	1.49572	5.25714	1.64177	3.58868	1.90391	2.73466	3.41369
-0.39	1.48483	5.25518	1.63434	3.59126	1.90858	2.73063	3.40750
-0.40	1.47383	5.25322	1.62666	3.59389	1.91262	2.72793	3.40052
-0.41	1.46721	5.25126	1.61872	3.59659	1.91661	2.72455	3.39276
-0.42	1.45146	5.24929	1.61051	3.59935	1.92036	2.72046	3.58417
-0.43	1.44008	5.24733	1.60205	3.60216	1.92377	2.71566	3.37476
-0.44	1.42858	5.24535	1.59331	3.60503	1.92638	2.71006	3.36452
-0.45	1.41694	5.24340	1.58431	3.60796	1.92964	2.70671	3.35343
-0.46	1.40516	5.24144	1.57503	3.61094	1.93201	2.69657	3.34147
-0.47	1.39324	5.23947	1.56548	3.61398	1.93394	2.68863	3.32363
-0.48	1.38118	5.23751	1.55565	3.61707	1.93941	2.67987	3.31492
-0.49	1.36897	5.23554	1.54554	3.62022	1.93635	2.67027	[illegible]
-0.50	1.35660	5.23358	1.53514	3.62341	1.93671	2.65832	3.28479

SIGMA	5,1	6,1	7,1	8,1	9,1	10,1
0.00	3.90945	4.56565	5.21067	5.84907	6.48317	7.11431
0.01	3.89595	4.55073	5.19428	5.83116	6.46372	7.09527
0.02	3.88212	4.53540	5.17741	5.81271	6.44364	7.07155
0.03	3.86795	4.51966	5.16006	5.79370	6.42295	7.04915
0.04	3.85346	4.50353	5.14224	5.77416	6.40166	7.02609
0.05	3.83866	4.48700	5.12396	5.75409	6.37977	7.00236
0.06	3.82355	4.47009	5.10523	5.73350	6.35731	6.97800
0.07	3.80813	4.45281	5.08605	5.71241	6.33427	6.95300
0.08	3.79241	4.43515	5.06643	5.69081	6.31066	6.92373
0.09	3.77640	4.41713	5.04639	5.66872	6.28650	6.90113
0.10	3.76010	4.39875	5.02592	5.64614	6.26180	6.87428
0.11	3.74351	4.38002	5.00503	5.62308	6.23655	6.84683
0.12	3.72664	4.36094	4.98373	5.59954	6.21076	6.81878
0.13	3.70949	4.34151	4.96202	5.57554	6.18445	6.79015
0.14	3.69207	4.32174	4.93990	5.55107	6.15762	6.76095
0.15	3.67437	4.30163	4.91739	5.52614	6.13027	6.73117
0.16	3.65640	4.28118	4.89448	5.50076	6.10242	6.70082
0.17	3.63817	4.26041	4.87118	5.47493	6.07405	6.66991
0.18	3.61967	4.23931	4.84749	5.44866	6.04515	6.63845
0.19	3.60090	4.21788	4.82342	5.42194	6.01582	6.60645
0.20	3.58188	4.19613	4.79896	5.39479	5.98596	6.57386
0.21	3.56259	4.17406	4.77413	5.36719	5.95561	6.54075
0.22	3.54304	4.15166	4.74891	5.33917	5.92477	6.50709
0.23	3.52324	4.12895	4.72332	5.31071	5.89344	6.47289
0.24	3.50318	4.10592	4.69736	5.28182	5.86163	6.43816
0.25	3.43286	4.08257	4.67102	5.25250	5.82933	6.40289
0.26	3.46228	4.05891	4.64430	5.22275	5.79655	6.36708
0.27	3.44144	4.03493	4.61722	5.19257	5.76330	6.33074
0.28	3.42035	4.01063	4.58976	5.16197	5.72955	6.29387
0.29	3.39900	3.98601	4.56192	5.13094	5.69533	6.25646
0.30	3.37783	3.96108	4.53372	5.09948	5.66063	6.21852
0.31	3.35551	3.93583	4.50514	5.06759	5.62544	6.18004
0.32	3.33338	3.91026	4.47618	5.03526	5.58977	6.14102
0.33	3.31098	3.88437	4.44684	5.00251	5.55361	6.10146
0.34	3.28832	3.85815	4.41712	4.96932	5.51696	6.06136
0,35	3.26539	3.83161	4.38703	4.93569	5.47982	6.02072
0.36	3.24219	3.80474	4.35654	4.90163	5.44219	5.97955
0.37	3.21872	3.77753	4.32567	4.86712	5.40405	5.93779
0.38	3.19497	3.75000	4.29441	4.83216	5.36542	5.89549
0.39	3.17095	3.72213	4.26275	4.79675	5.32628	5.85262
0.40	3.14664	3.69391	4.23069	4.76088	5.28662	5.80920
0.41	3.12205	3.66535	4.19823	4.72456	5.24645	5.76519
0.42	3.09717	3.63644	4.16536	4.68776	5.20576	5.72061
0.43	3.07200	3.60718	4.13208	4.65050	5.16454	5.67544
0.44	3.04653	3.57756	4.09837	4.61275	5.12277	5.62968
0.45	3.02076	3.54757	4.06424	4.57452	5.08047	5.58332
0.46	2.99468	3.51721	4.02968	4.53580	5.03761	5.53634
0.47	2.96828	3.48647	3.99467	4.49657	4.99418	5.48874
0.48	2.94156	3.45534	3.95922	4.25683	4.95019	5.44051
0.49	2.91452	3.42382	3.92331	4.41657	4.90561	5.39163
0.50	2.88715	3.39191	3.88693	4.37578	4.86044	5.34210

SIGMA	5,1	6,1	7,1	8,1	9,1	10.1
0.00	3.90945	4.56565	5.21067	5.84907	6.48317	7.11431
-0.01	3.92261	4.58014	5.22656	5.86641	6.50199	7.13464
-0.02;	3.93542	4.59421	5.24195	5.88317	6.52913	7.15425
-0.03	3.94787	4.60783	5.25682	5.89934	6.53768	7.17314
-0.04	3.95998	4.62101	5.27116	5.91491	6.55452	7.19128
-0.05	3.97166	4.63372	5.28497	5.92987	6.57067	7.20866
-0.06	3.98299	4.64597	5.29822	5.94420	6.58613	7.22528
-0.07	3.99392	4.65773	5.31092	5.95789	6.60087	7.24110
-0.08	4.00444	4.56900	5.32304	5.97093	6.61488	7.25612
-0.09	4.01455	4.67976	5.33457	5.98330	6.62814	7.27032
-0.10	4.02423	4.69001	5.34549	5.99499	6.64065	7.28369
-0.11	4.03347	4.69793	5.35581	6.00598	6.65238	7.29619
-0.12	4.04228	4.70890	5.36549	6.01626	6.66331	7.30783
-0.13	4.03039	4.71752	5.37453	6.02518	6.67344	7.31857
-0.14	4.05845	4.72556	5.38291	6.03462	6.68274	7.32841
-0.15	4.06582	4.73302	5.39062	6.04267	6.69119	7.33732
-0.16	4.07268	4.73988	5.39763	6.04993	6.69878	7,43527
-0.17	4.07903	4.74615	5.40394	6.05641	6.70549	7.35227
-0.18	4.08434	4.75175	5.40952	6.06702	6.71130	7.35327
-0.19	4.09011	4.75672	5.41437	6.06690	6.71819	7.36326
-0.20	4.09482	4.76102	5.41846	6.07088	6.72013	7.36723
-0.21	4.09896	4.76465	5.42177	6.07399	6.72312	7.37015
-0.22	4.10250	4.76759	5.42429	6.07622	6.72514	7.37200
-0.23	4.10543	4.76981	5.42601	6.07755	6.72615	7.37275
-0.24	4.10773	4.77130	5.42689	6.07795	6.72815	7.37240
-0.25	4.10940	4.77205	5.42694	6.07741	6.72510	7.37091
-0.26	4.11041	4.77204	5.42612	6.07591	6.72300	7.36826
-0.27	4.11074	4.77125	5.42442	6.07343	6.71983	7.36444
-0.28	4.11038	4.76966	5.42182	6.06995	6.71555	7.35942
-0.29	4.10931	4.76725	5.41830	6.06546	6.71016	7.35319
-0.30	4.10752	4.76402	5.41836	6.05993	6.70363	7.34571
-0.31	4.10498	4.75994	5.40846	6.05335	6.69594	7.33697
-0.32	4.10168	4.75499	5.40209	6.04569	6.68707	7.32695
-0.33	4.09761	4.74915	5.39474	6.03694	6.67701	7.31563
-0.34	4.09275	4.74244	5.38638	6.02709	6.66573	7.30298
-0.35	4.08708	4.73480	5.37701	6.01610	6.65322	7.28899
-0.36	4.08058	4.72623	5,36660	6.00397	6.63945	7.27364
-0.37	4.07324	4.71672	5.35513	5.99068	6.62441	7.25690
-0.38	4.06506	4.70624	5.34260	5.97621	6.60808	7.23876
-0.39	4.05600	4.69480	5.32898	5.96055	6.59044	7.21920
-0.40	4.04606	4.68236	5.31427	5.94367	6.57148	7.19819
-0.41	4.03522	4.66892	5.29843	5.92556	6.55117	7.17572
-0.42	4.02347	4.65445	5.28147	5.90621	6.52949	7.15177
-0.43	4.01080	4.63896	5.26336	5.88559	6.50643	7.12632
-0.44	3.99719	4.62243	5.24409	5.86370	6.48198	7.09935
-0.45	3.93263	4.60483	5.22365	5.84051	6.45611	7.07084
-0.46	3.96711	4.58616	5.20201	5.81601	6.42881	7.04077
-0.47	3.95062	4.56641	5.17917	5.79018	6.40005	7.00913
-0.48	3.93315	4.54556	5.15512	5.76301	6.36982	7.97588
-0.49	3.91467	4.52359	5.12983	5.73448	6.33811	7.94012
-0.50	3.89520	4.50051	5.10329	5.70458	6.30489	7.90452

APPENDIX A4.2

RATIOS FOR POISSON'S RATIO DETERMINATION

SIGMA	$\frac{K_{0,1}-K_{3,1}}{K_{3,1}}$	$\frac{K_{1,2}-K_{5,1}}{K_{5,1}}$	$\frac{K_{0,2}-K_{9,1}}{K_{9,1}}$	$\frac{K_{1,2}-K_{4,1}}{K_{4,1}}$
0	-0.26553	-0.09506	-0.17765	0.09462
0.01	-0.25934	-0.09197	-0.17487	0.09868
0.02	-0.25307	-0.08877	-0.17200	0.10288
0.03	-0.24662	-0.08546	-0.16903	0.10720
0.04	-0.24031	-0.08206	-0.16596	0.11165
0.05	-0.23381	-0.07850	-0.16280	0.11624
0.06	-0.22723	-0.07485	-0.15954	0.12095
0.07	-0.22056	-0.07110	-0.15617	0.12580
0.08	-0.21382	-0.06723	-0.15271	0.13077
0.09	-0.20698	-0.06325	-0.14914	0.13588
0.10	-0.20006	-0.05916	-0.14548	0.14111
0.11	-0.19304	-0.05496	-0.14171	0.14648
0.12	-0.18692	-0.05065	-0.13783	0.15197
0.13	-0.17873	-0.04623	-0.13385	0.15760
0.14	-0.17110	-0.04169	-0.12976	0.16336
0.15	-0.16202	-0.03705	-0.12557	0.16925
0.16	-0.15651	-0.03229	-0.12126	0.17527
0.17	-0.14889	-0.02743	-0.11684	0.18142
0.18	-0.14116	-0.02246	-0.11230	0.18770
0.19	-0.13331	-0.01737	-0.10765	0.19411
0.20	-0.12535	-0.01218	-0.10288	0.20065
0.21	-0.11727	-0.00688	-0.09798	0.20731
0.22	-0.10905	-0.00148	-0.09296	0.21410
0.23	-0.10071	0.00402	-0.08781	0.22101
0.24	-0.09223	0.00962	-0.08253	0.22803
0.25	-0.08362	0.01531	-0.07712	0.23517
0.26	-0.07486	0.02109	-0.07157	0.24240
0.27	-0.06595	0.02695	-0.06588	0.24974
0.28	-0.05689	0.03289	-0.06004	0.25716
0.29	-0.04766	0.03888	-0.05406	0.26466
0.30	-0.03828	0.04493	-0.04792	0.27221
0.31	-0.02872	0.05101	-0.04163	0.27980
0.32	-0.01899	0.05710	-0.03517	0.28741
0.33	-0.00907	0.06318	-0.02854	0.29501
0.34	0.00105	0.06924	-0.02174	0.30257
0.35	0.01136	0.07523	-0.01476	0.31004
0.36	0.02187	0.08111	-0.00760	0.31740
0.37	0.03260	0.08686	-0.00024	0.32458
0.38	0.04355	0.09243	0.00731	0.33153
0.39	0.05474	0.09778	0.01507	0.33821
0.40	0.06617	0.10286	0.02305	0.34457

SIGMA	$\frac{K_{0,1}-K_{3,1}}{K_{3,1}}$	$\frac{K_{1,2}-K_{5,1}}{K_{5,1}}$	$\frac{K_{0,2}-K_{9,1}}{K_{9,1}}$	$\frac{K_{1,2}-K_{4,1}}{K_{4,1}}$
-0.00	-0.26552	-0.09568	-0.17764	0.09600
-0.01	-0.27165	-0.09804	-0.18033	0.09068
-0.02	-0.27770	-0.10090	-0.18291	0.08687
-0.03	-0.28369	-0.10366	-0.18540	0.08320
-0.04	-0.28960	-0.10630	-0.18779	0.07965
-0.05	-0.29544	-0.10882	-0.19008	0.07624
-0.06	-0.30123	-0.11124	-0.19228	0.07296
-0.07	-0.30694	-0.11353	-0.19438	0.06982
-0.08	-0.31259	-0.11571	-0.19638	0.06681
-0.09	-0.31818	-0.11777	-0.19828	0.06393
-0.10	-0.32370	-0.11972	-0.20008	0.06119
-0.11	-0.32916	-0.12154	-0.20179	0.05859
-0.12	-0.33456	-0.12324	-0.20339	0.05613
-0.13	-0.33990	-0.12482	-0.20489	0.05381
-0.14	-0.34517	-0.12628	-0.20629	0.05164
-0.15	-0.35039	-0.12761	-0.20758	0.04961
-0.16	-0.35555	-0.12888	-0.20877	0.04773
-0.17	-0.36064	-0.12988	-0.20986	0.04600
-0.18	-0.36568	-0.13082	-0.21083	0.04442
-0.19	-0.37065	-0.13162	-0.21170	0.04300
-0.20	-0.37556	-0.13229	-0.21245	0.04174
-0.21	-0.38041	-0.13282	-0.21309	0.04064
-0.22	-0.38520	-0.13321	-0.21362	0.03971
-0.23	-0.38992	-0.13345	-0.21403	0.03895
-0.24	-0.39459	-0.13354	-0.21432	0.03837
-0.25	-0.39919	-0.13348	-0.21449	0.03796
-0.26	-0.40372	-0.13327	-0.21454	0.03774
-0.27	-0.40819	-0.13290	-0.21446	0.03770
-0.28	-0.41259	-0.13236	-0.21425	0.03786
-0.29	-0.41692	-0.13166	-0.21391	0.03821
-0.30	-0.42119	-0.13079	-0.21344	0.03877
-0.31	-0.42539	-0.12975	-0.21282	0.03953
-0.32	-0.42951	-0.12853	-0.21207	0.04051
-0.33	-0.43356	-0.12712	-0.21118	0.04172
-0.34	-0.43753	-0.12553	-0.21014	0.04314
-0.35	-0.44143	-0.12375	-0.20895	0.04451
-0.36	-0.44525	-0.12176	-0.20760	0.04671
-0.37	-0.44899	-0.11958	-0.20610	0.04886
-0.38	-0.45265	-0.11719	-0.20444	0.05126
-0.39	-0.45623	-0.11458	-0.20261	0.05393
-0.40	-0.45973	-0.11176	-0.20060	0.05656

APPENDIX A6.1

THE PHASE AND GROUP VELOCITY IN THE LINEAR REGION OF THE L(O,1) DISPERSION CURVE

The frequency equation for axially symmetric vibrations is:

$$2\Omega^2\bar{\alpha}J_1(\bar{\alpha})J_1(\bar{\beta})-(\Omega^2-2\bar{\gamma}^2)^2J_0(\bar{\alpha})J_1(\bar{\beta})-4\bar{\gamma}^2\bar{\alpha}\bar{\beta}J_1(\bar{\alpha})J_0(\bar{\beta})=0 \tag{A.6.1}$$

If the Bessel functions are expanded in their series form and for small arguments only the first terms of the series are taken the zero and first order Bessel functions are:

$$J_0(z) \doteqdot 1 \tag{A.6.2}$$

and

$$J_1(z) \doteqdot \tfrac{1}{2}z \tag{A.6.3}$$

Equation (A.6.1) then becomes:

$$\Omega^2\bar{\alpha}^2-(\Omega^4-4\Omega^2\bar{\gamma}^2+4\bar{\gamma}^4)-4\bar{\gamma}^2\bar{\alpha}^2 = 0 \tag{A.6.4.}$$

By definition

$$\bar{\alpha}^2 = k^2\Omega^2-\bar{\gamma}^2 \tag{A.6.5}$$

then

$$\Omega^2\{k^2(\Omega^2-1) + \bar{\gamma}^2(3-4k^2)\} = 0 \tag{A.6.6}$$

With the bracketed term equal to zero gives

$$\frac{\Omega^2}{\bar{\gamma}^2} = \frac{3 - 4k^2}{1 - k^2} \tag{A.6.7}$$

Since only the linear portion of the curve is being considered at low $\bar{\gamma}$ values, group and phase velocities are equal.

Since,

$$k^2 = \frac{\mu}{\lambda + 2\mu} \tag{A.6.8}$$

$$\frac{\Omega^2}{\bar{\gamma}^2} = \frac{3\lambda + 2\mu}{\lambda + \mu} \tag{A.6.9}$$

and returning to un-normalised variables,

$$C_{gp} = C_{ph} = \frac{\omega}{\gamma} = \sqrt{\frac{(3\lambda + 2\mu)}{\lambda + 2\mu}\mu \frac{1}{\rho}} \tag{A.6.10}$$

Hence,

$$C = \sqrt{\frac{E}{\rho}} \tag{A.6.11}$$

APPENDIX A6.2

VELOCITY OF SOUND IN THORIATED TUNGSTEN

An independent check of the sound velocity in 2% thoriated tungsten was carried out on one of the sensors used in Chapter 6. The measured sensor length was 167.5 mm with a two way flight time of 71.893μs. The rod velocity is therefore

$$v = \frac{2 \times 167.5.10^{-3}}{71.893.10^{-6}} = 4659.7 \text{ ms}^{-1}$$

The method uses standing waves between the junction at the end of the specimen. The sensor is excited with a long burst of oscillations such that the junction and end echoes overlap. When the overlap signal amplitude is at a minimum then the wave in the sensor must have travelled an odd number of half wave lengths. i.e. so that the junction and end echoes are 180^{p} out of phase.

The results obtained for the 167 mm probe were

f(kHz)	118.16	132.08	145.87	160.25	173.64
n	8½	9½	10½	11½	12½
f/n	13.901	13.903	13.892	13.935	13.891

f(kHz)	187.69	201.65	215.45	229.78	243.58
n	13½	14½	15½	16½	17½
f/n	13.903	13.907	13.900	13.926	13.919

Mean = 13.907 kHz

Standard deviation σ = 0.014

Velocity v = 4659.1 ms^{-1}

It will be seen that that the two measurements are in close agreement. The time of flight corresponds to a frequency of 13.909 kHz which is almost identical with the value obtained by the alternative method. If some systematic error were associated with the junction this would probably show up as a phase error. The constancy of the values of f/n indicate that any such error is less than the sensitivity of the observations.

APPENDIX A7

TIME OF FLIGHT PULSE TRACKING CIRCUITRY

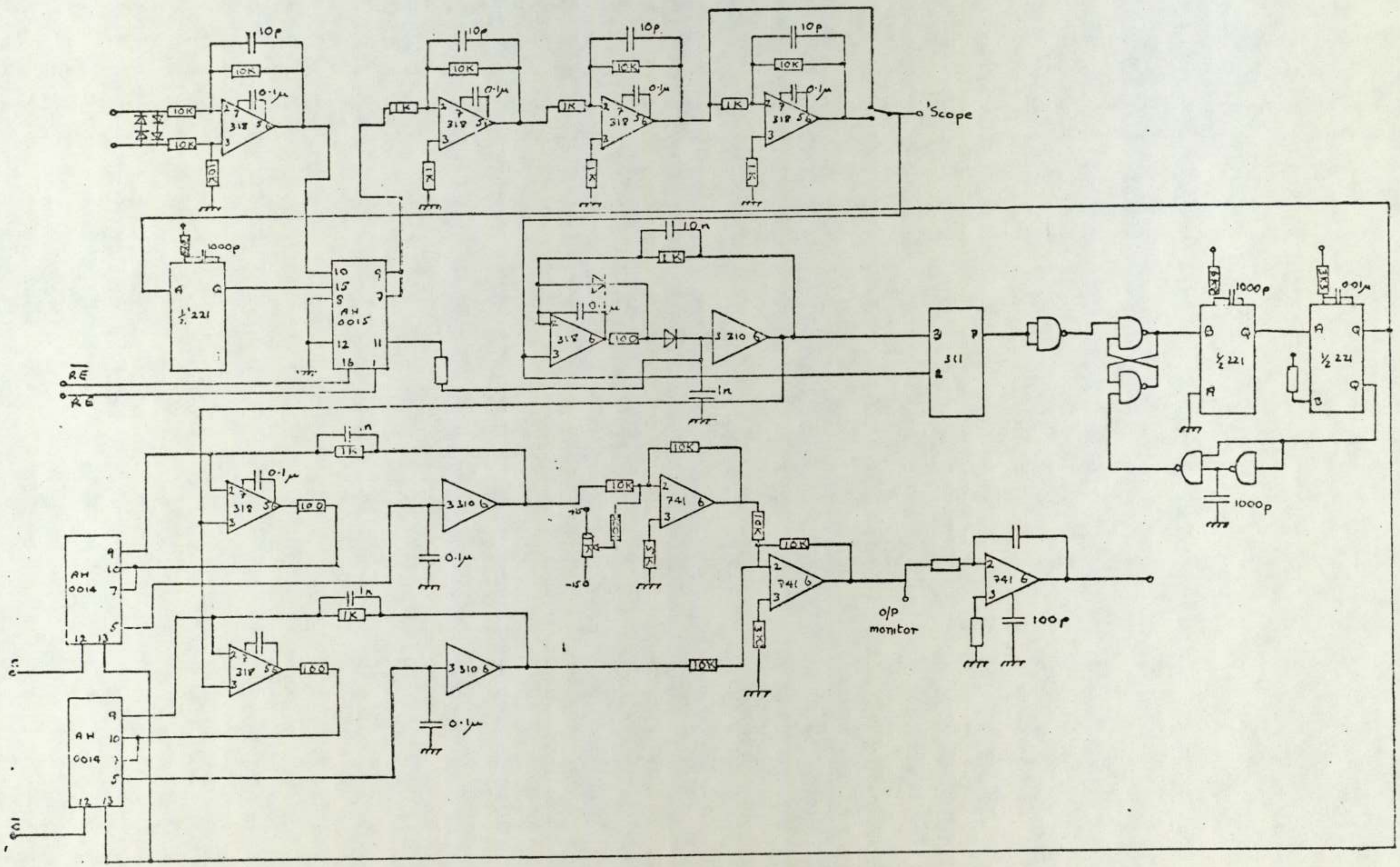

RECEIVER/TRACKING CONTROL LOOP

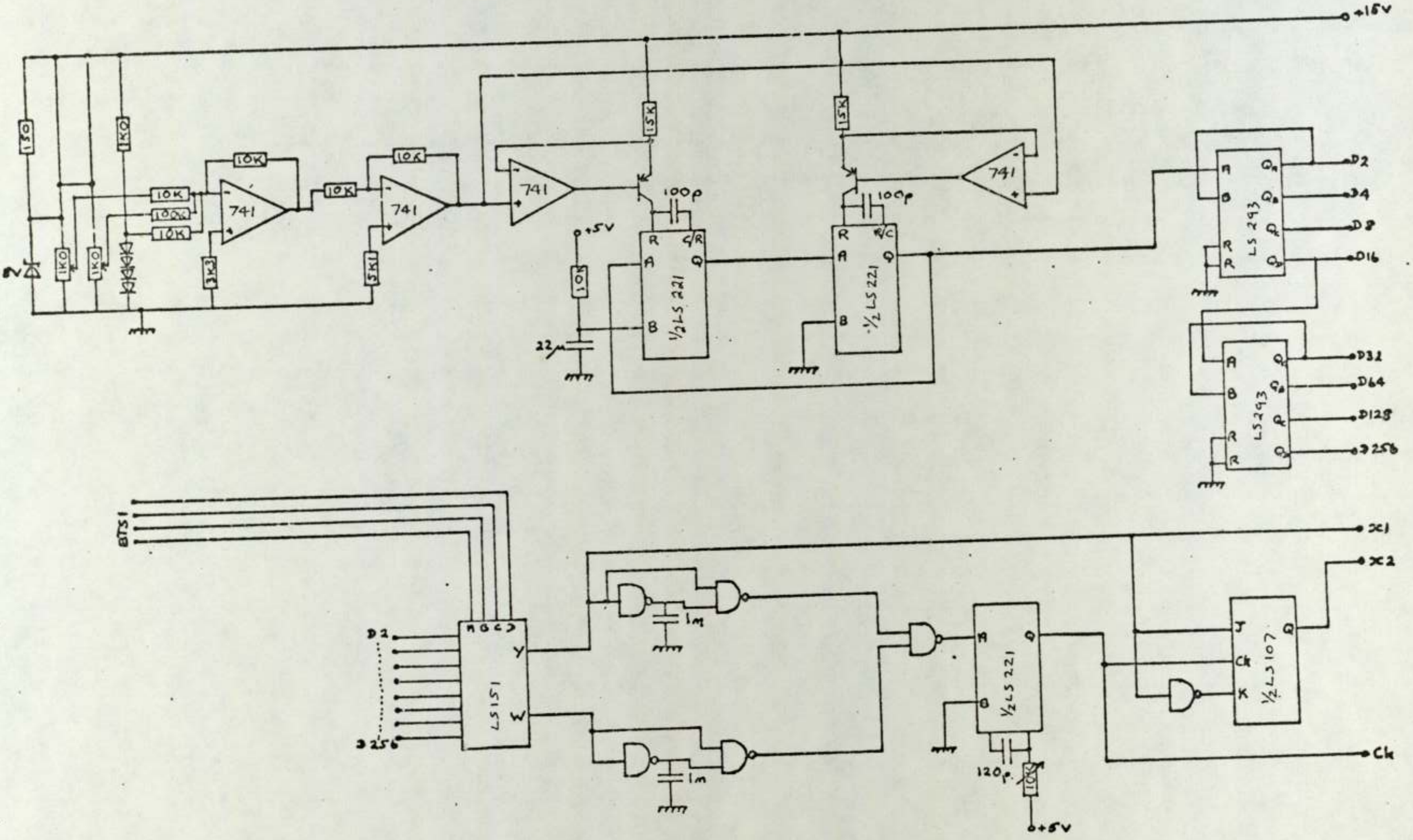

TIME OF FLIGHT OSCILLATOR

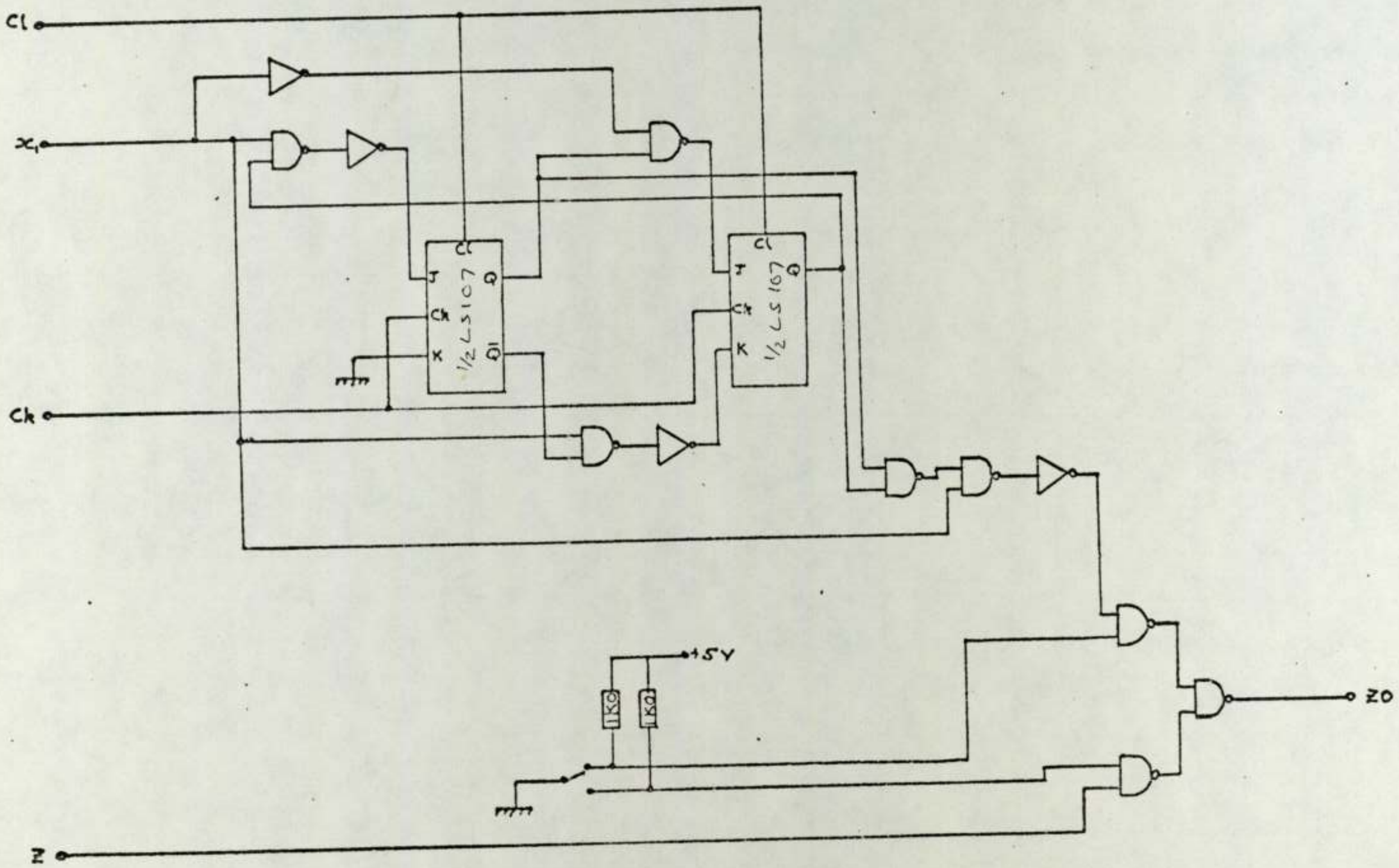

DELAY/NO DELAY PULSE GROUP SELECTOR

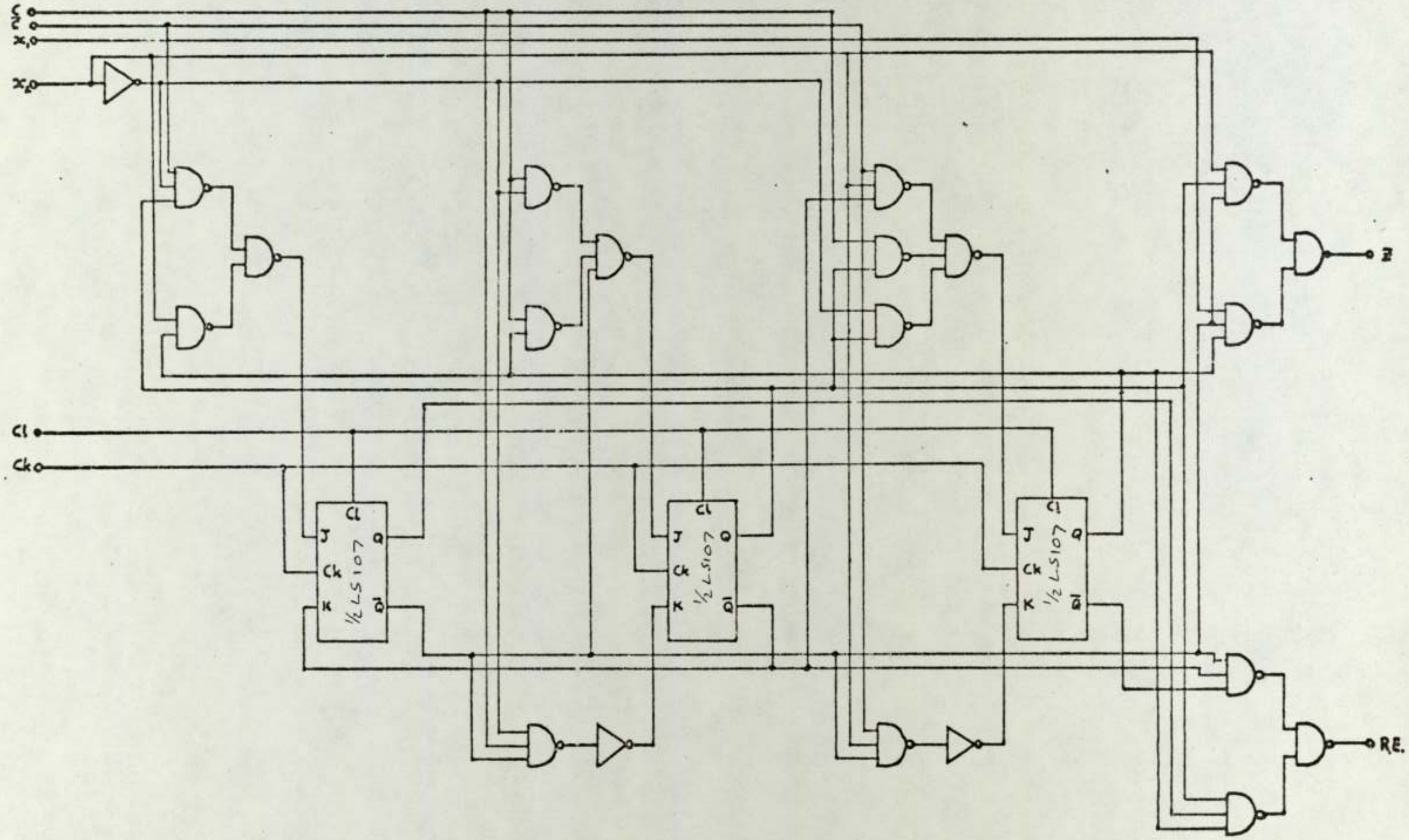

ADVANCED/DELAYED PULSE GROUP
SELECTOR

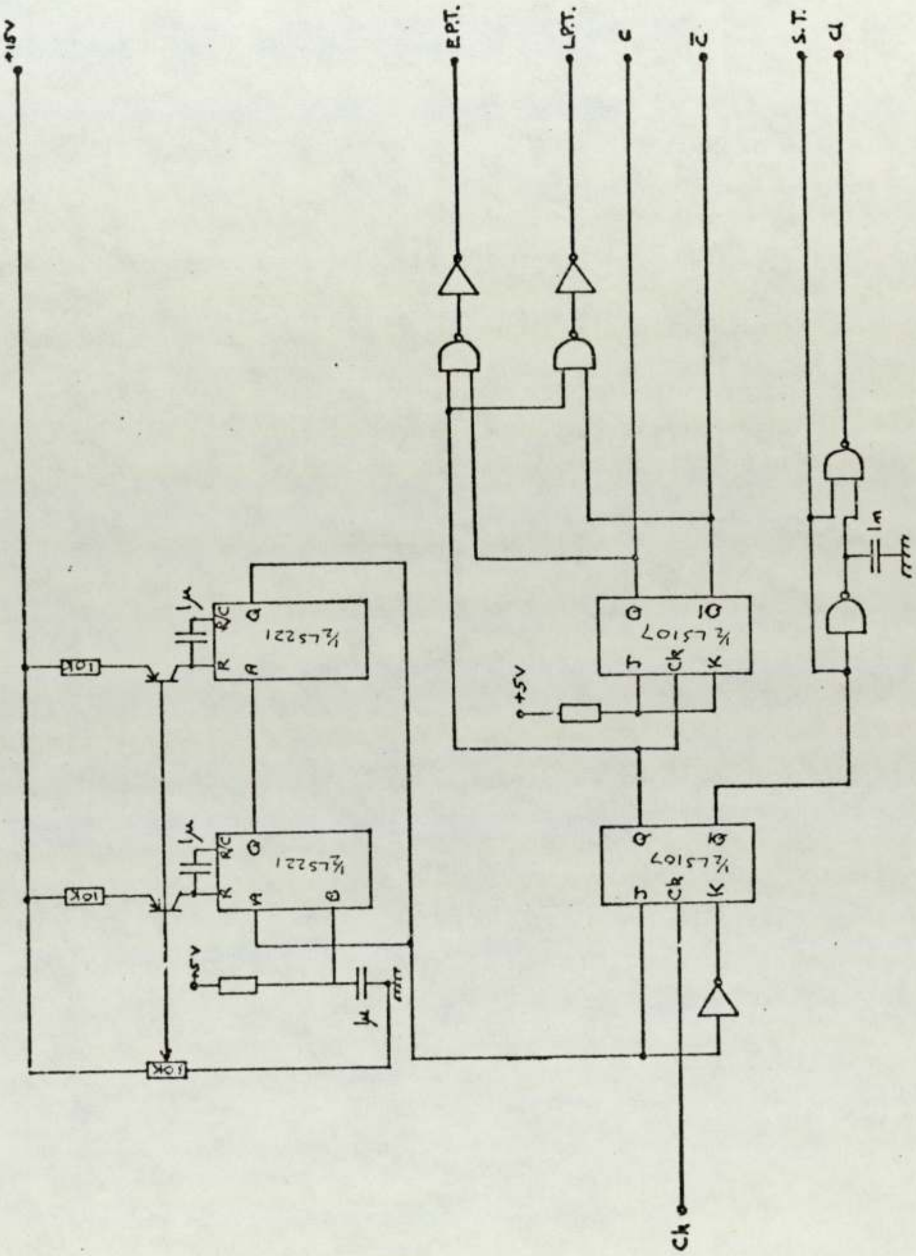

P.R.F. OSCILLATOR

REFERENCES

REFERENCES

1. POCHHAMMER
'Uber Die Fortpflanzungsgescwindigkeiten Kleiner Schwingungen in Einem Unbegrenzten Isotropen Kreiszlinder',
J. Reine Angear Math., 81, pp. 324-336 (1876)

2. CHREE
'The Equations of an Isotropic Elastic Solid in Polar and Cylindrical Co-ordinates, their Solution and Applications',
Trans. Cambridge Phil. Soc., 14, pp. 250-369 (1889)

3. LOVE
'A Treatise on the Mathematical Theory of Elasticity',
Dover, 4th Edition, pp. 287-292 (1927)

4. BANCROFT
'The Velocity of Longitudinal Waves in Cylindrical Bars',
Phys. Rev., 59, pp. 588-593 (1941)

5. HUDSON
'Dispersion of Elastic Waves in Solid Cylinders',
Phys. Rev., 63, pp. 46-51 (1943)

6. ADEM
'On the Axially Symmetric Steady Wave Propagation in Elastic Circular Rods',
Qu. Appl. Math., 12, pp. 261-275 (1954)

7. MINDLIN AND MCNIVEN
'Axially Symmetric Waves in Elastic Rods',
Trans. A.S.M.E., 27, pp. 145-151 (1960)

8. PAO AND MINDLIN
'Dispersion of Flexural Waves in an Elastic Circular Cylinder',
J. Appl. Mech., 27, p. 513 (1960)

9. PAO
'The Dispersion of Axially Symmetric Waves in Elastic Rods',
J. Appl. Mech., 29, pp. 61-64 (1962)

10. ONOE, MCNIVEN AND MINDLIN
'Dispersion of Axially Symmetric Waves in Elastic Rods',
J. Appl. Mech., 29, pp. 729-734 (1962)

11. ZEMANEK
'An Experimental and Theoretical Investigation of Elastic Wave Propagation in a Cylinder',
J.A.S.A., 51, pp. 265-283 (1972)

12. REDWOOD
'Mechanical Waveguides',
Pergamon Press (1960)

13. GRAFF
'Wave Motion in Elastic Solids',
Clarendon Press (1975)

14. MEEKER AND MEITZLER
'Guided Wave Propagation',
Physical Acoustics, Vol. 1, Pt. A, Ed. W. P. Mason,
Academic Press (1964)

15. MEITZLER
'Backward Wave Transmission of Stress Pulses in Elastic Cylinders and Plates',
J.A.S.A., 38, pp. 835-842 (1965)

16. RASBAND
'Resonant Vibrations of Free Cylinders and Discs',
J.A.S.A., 57, pp. 899-905 (1975)

17. HUTCHINSON
'Axisymmetric Vibrations of a Free Finite Length Rod',
J.A.S.A., 51, pp. 233

18. BISWAS, NANGIA AND KUMAR
'Flexural Vibrations of a Finite Circular Cylinder',
Acoustica, 35, pp. 26-31 (1976)

19. OLIVER
'Elastic Wave Dispersion in a Cylindrical Rod by a Wide Band Short Duration Pulse Technique',
J.A.S.A., 29, pp. 189-194 (1957)

20. MCMAHON
'Experimental Study of the Vibrations of Solid Isotropic Elastic Cylinders',
J.A.S.A., 36, pp. 85-92 (1964)

21. MCNIVEN AND PERRY
'Axially Symmetric Waves in Finite Elastic Rods',
J.A.S.A., 34, pp. 433-437 (1962)

22. BOOKER AND SAGAR

'Velocity Dispersion of the Lowest Order Longitudinal Mode in Finite Rods of Circular Cross Section',

J.A.S.A, 49, pp. 1491-1498 (1970)

23. ONOE

'Contour Vibrations of Isotropic Circular Plates',

J.A.S.A., 28, pp. 1158-1162 (1956)

24. ONOE

'Gravest Contour Vibration of Thin Anisotropic Circular Plates',

J.A.S.A, 30, pp. 634-638 (1957)

25. HOLLAND

'Numerical Studies of Elastic Disc Contour Modes Lacking Axial Symmetry',

J.A.S.A., 40, pp. 1051-1057 (1966)

26. SHARPE

'An Experimental and Theoretical Investigation of the Spectra of Selected Resonators',

Ph. D. Thesis, University of Aston in Birmingham (1974)

27. AMBATI

'Experimental and Numerical Studies of Radial and Contour Extensional Modes in Elastic Discs',

M.Sc. Thesis, University of Aston in Birmingham (1973)

28. MOSELEY
'Contribution to the Theory of Radial Extensional Vibrations in Thin Discs',
J.A.S.A, 32, pp. 991-995 (1960)

29. LUCEY
'Resonant and Anti-resonant Frequencies of Thick Discs and Thick Rods',
J.A.S.A, 43, pp. 1324-1328 (1968)

30. MCSKIMMIN
'Ultrasonic Methods for Measuring the Mechanical Properties of Liquids and Solids',
Physical Acoustics,Vol. 1, P.T.A., Academic Press (1964)

31. BELL
'Ultrasonic Thermometry using Resonance Techniques'
Temperature, its measurement and control in science and Industry, Washington (1972)

32. KALMARCZIE
'Energy Trapped Resonances in Solid Structures',
Ph.D. Thesis, University of Aston in Birmingham (1976)

33. SETH
'Ultrasonic Pyrometer for Industrial Applications',
Ph.D. Thesis, University of Aston in Birmingham (1974)

34. FATHIMANI
'The Automation of Resonant Thermometer Probe Measurements',
Ph.D. Thesis, University of Aston in Birmingham (1976)

35. BELL, JOHNSON AND SHARPE
'Pulse Echo Method of Investigating the Properties of Mechanical Resonators',
J.A.S.A., 57, pp. 1085-1093 (1975)

36. THURSTON
'Wave Propagation in Fluids and Normal Solids',
In. Physical Acoustics, Vol. 1, P.T.A., Academic Press (1964)

37. MEITZLER
'Mode Coupling Occurring in the Propagation of Elastic Pulses in Wires',
J.A.S.A., 33, pp. 435-445 (1961)

38. LANGE
'Mode Conversion in the Long Wavelength Limit',
J.A.S.A., 41, pp. 1449-1452 (1967)

39. SMITH AND LEEDS
'Modern Material Advances in Development and Applications',
Vol. 7, p. 139 (1970)

40. MASON AND KNIBBS
'Variation with Temperature of Young's Modulus of Polycrystalline Graphite',
Nature, 188, pp. 33-35 (1960)

41. BELL
'Velocity of Sound in Metals at High Temperature',
Phil. Mag., Vol. 2, pp. 1113-1120 (1957)

42. LYNNWORTH
'Ultrasonic Measurement of Elastic Properties in Graphite Rods',
Panametrics Technical Memorandum, January (1973)

43. International Colloquium on High Temperature in Pile Thermometry,
Sect. $\overline{\underline{\text{iv}}}$, Ultrasonic and Noise Thermometry, (1974)

44. PAPADAKIS, LYNNWORTH ET AL
'Ultrasonic Thermometry for LMFBR Systems',
Final Report to U.S. Atomic Energy Commission, Contract at (30-1)-3096,(1972)

45. ARAVE AND BUCHENAUER
'Use of Tungsten 2% Thoria Ultrasonic Transmission Line Sensor to Improve the Performance of High Temperature Ultrasonic Thermometry',
International Colloquium of High Temperature in Pile Thermometry, Petten (1974)

46. ROTHBART AND ROSENBERG
'A Theory of Pulse Transmission Along a Magnetostrictive Delay Line',
IRE Trans., PGUE 6, (1957)

47. ROSENBERG AND ROTHBART
' Electrical Design of the Transducer Network of Magnetostrictive Delay Lines',
IRE Nat. Conv. Record, Vol. 6, Pt. 2, (1958)

48. WILLIAMS

'Theory of Magnetostrictive Delay Lines for Pulse and Continuous Wave Transmission',

IRE Trans., PGUE 7, (1959)

49. KE AND ZENER

'Symposium on the Plastic Deformation of Crystalline Solids',

p.185, (1950)

50. HORVAY AND MIRABAL

'The End Problem of Cylinders',

Journal of Applied Mechanics, Trans.ASME, pp. 561-570, (1958)

51. AMBATI

'An Experimental and Theoretical Investigation into the Acoustic Spectra of Solids having Circular Symmetry',

Ph.D. Thesis, University of Aston in Birmingham, (1976)

52. BELL AND KALMARCZIE

'The End Resonance of Strips and Plates',

Physics Letters, Vol. 61A, pp. 91-94, (1977)